AN ABSTRACT OF THE THESIS OF

Keith S. Jennings for the degree of Master of Science in Water Resources Science presented on June 13, 2014.

Title: Precipitation-Snowmelt Timing and Snowmelt Augmentation of Large Peak Flow Events, Western Cascades, Oregon.

Abstract approved:

_____

Julia A. Jones

Despite advances in the understanding of rain-on-snow storms and their resulting peak flows, little is understood about the response of snowmelt to precipitation and the relative timing of the two at multiple temporal scales within such events. To address this issue, climate, snowmelt, and streamflow data were analyzed for 26 large storms in the H.J. Andrews Experimental Forest in the western Cascades of Oregon. Cumulative net snowmelt was plotted against precipitation for each storm to identify net snowmelt response categories, which were then used to summarize climatic and streamflow data, while the timing of precipitation and net snowmelt was assessed at multiple temporal scales and time ranges with wavelet coherence.

Five precipitation-net snowmelt response categories were identified: flat; persistent melt; persistent accumulation; late melt; and late accumulation. Persistent melt events, which were characterized by concomitantly increasing cumulative net snowmelt and precipitation, had the highest mean peak flow and water available for runoff values of the response categories. Large, contiguous regions of significant wavelet coherence at multiple temporal scales were observed in both the persistent melt and persistent accumulation categories, but the phase difference distributions indicated differing snowpack dynamics with pulses of precipitation leading pulses of

snowmelt in the former and precipitation being absorbed by the snowpack in the latter.

High water available for runoff totals and peak flows were observed in each of the five response categories, but a dewpoint temperature consistently above 0.5°C, elevated wind speeds, and a high fraction of precipitation falling as rain in the persistent melt category facilitated rapid snowmelt rates which were often synchronized with precipitation. Wavelet coherence showed this synchronization to be significant across all temporal scales and time periods for the two largest peak flows in the study, indicating that tightly coupled rainfall-synchrony is essential in generating an extreme rain-on-snow flood. By quantifying the amount and timing of net snowmelt, the categorization scheme provides a means of distinguishing among rain-on-snow events and predicting peak discharge magnitude.

Precipitation-Snowmelt Timing and Snowmelt Augmentation of Large Peak Flow Events, Western Cascades, Oregon

by
Keith S. Jennings

A THESIS

submitted to

Oregon State University

in partial fulfillment of
the requirements for the
degree of

Master of Science

Presented June 13, 2014
Commencement June 2015

Master of Science thesis of Keith S. Jennings presented on June 13, 2014

APPROVED:

Major Professor, representing Water Resources Science

Director of the Water Resources Graduate Program

Dean of the Graduate School

I understand that my thesis will become part of the permanent collection of Oregon State University libraries. My signature below authorizes release of my thesis to any reader upon request.

Keith S. Jennings, Author

ACKNOWLEDGEMENTS

I am humbled by and thankful for the guidance, support, assistance, and inspiration I have received over the past 22 months. Even though there is only one name on the front of a thesis, I would be nowhere without the selfless individuals below. I thank them as a student and as a person.

First, a sincere thank you to my committee: To Julia Jones, for helping me progress as a researcher through your motivation and wisdom (not to mention the countless hours you have spent on this thesis). I feel lucky to have been accepted as one of your students. To Anne Nolin, for sparking my interest in hydrology and research. Few professors would devote so much time to answering the nearly endless stream of questions from a master's student such as myself, but you have. And to Catalina Segura, whose valuable insights improved data visualization.

To Mary Santelmann, the Water Resources Graduate Program director. Thank you for accepting me into this superb program, providing me funding through the Provost's Fellowship, and always supporting your students. And to Stacey Schulte and Jennifer Cohen, the tireless program assistants for Geography and Water Resources. Thank you for always responding so quickly and helping me out, no matter how inane or obvious the question.

To the students of the WRGP and Geography programs, particularly Water World (Hayley Corson-Rikert, Nick Dosch, John Hammond, Laura Hempel, William L'Hommedieu and Caroline Nash) and Matt Cooper. You could always be counted on for honest, critical feedback, and you are all wicked smart, too!

Finally, but certainly not last, a thank you to my family: Marley, it is your support that has made this all possible. You amaze me every day and I love everything about who you are and who you have become. To my parents for always being by my side and providing me with invaluable advice. (Here is where I would thank Hazel and Luxford, but they are dogs and can only read at a 0^{th} grade level.)

Also, I would like to acknowledge Jack Rothacher for having the foresight to establish the Hi-15 watershed studies and for the hard work of establishing and maintaining records in the early days of the studies with Al Levno.

Additionally, climate and streamflow measurements at the H.J. Andrews Experimental Forest are supported by National Science Foundation award #0823380 (Long-Term Ecological Research at the H.J. Andrews Experimental Forest—LTER6) and the United States Forest Service.

Again, I thank all of those who have made the past two years so memorable and transformative. As Carl Sandburg said, “I’m an idealist. I don’t know where I’m going, but I’m on my way.”

TABLE OF CONTENTS

TABLE OF CONTENTS (continued)

Page

LIST OF FIGURES

LIST OF FIGURES (continued)

Figure Page

LIST OF FIGURES (continued)

LIST OF TABLES

LIST OF APPENDICES

1. INTRODUCTION

Many processes contribute to extreme floods, but rain-on-snow events in the Pacific Northwest are among the most extreme in the US (O'Connor and Costa, 2004). In Oregon, Washington, and California, rain-on-snow floods are responsible for a majority of all flood fatalities in the month of January (Ashley and Ashley, 2008) and single events have produced billions of dollars in damages (U.S.A.C.E., 1996).

Despite their importance, the precipitation, snowmelt, and streamflow dynamics of the largest rain-on-snow events are not well understood. In western Oregon, extreme floods are always rain-on-snow events, but not all rain-on-snow events produce large peak flows (Jones and Perkins, 2010). Several mechanisms influence rain-on-snow event peak magnitude: snowmelt augmentation of water available for runoff (WAR); the influence of climatic variables, logging, and land-use change on snowmelt; and the effect of basin topography and tributary synchrony on peak streamflow.

Snowmelt augmented water available for runoff by 4% to 37% during the largest rain-on-snow events, which were associated with steeper hydrograph rise and higher peak discharges than rain-only events for two streams in western Oregon (Harr 1981). Rain-on-snow peak discharges were larger in clearcut compared to unharvested basins Harr (1986). Snowmelt during ROS events is dominated by latent and sensible heat, the turbulent energy exchanges (U.S.A.C.E., 1956). Because these energy terms depend on wind speed, open or exposed areas experience higher latent and sensible heat exchanges than forested sites and contribute more snowmelt (Harr 1981, van Heeswijk et al., 1996; Marks et al., 1998; Marks et al., 2001).

Basin topography, antecedent soil moisture, and snowpack presence/absence affect storm hydrograph shape and peak discharge (Perkins and Jones 2008). Generally, the presence of a snowpack increased the duration of stormflow and peak flow magnitude, while basins with short, steep slopes experienced a quicker, steeper hydrograph response than basins with long, shallow slopes. Synchronized streamflow from headwater basins augments peak discharges in higher order catchments, and forest harvest may further augment extreme rain-on-snow peak flows by increasing

the area that experiences synchronized snowmelt during a storm (Jones and Perkins 2010).

Despite these advances, little is known about the snowmelt dynamics and precipitation interactions with the snowpack at sub-daily time scales during storm events, and the effect of these interactions on peak discharges. Data on the relative timing and phase of precipitation and snowmelt, as well as data on peak discharges from the transient snow zone are rare. However, the H.J. Andrews Experimental Forest in western Oregon provides long-term data on precipitation, temperature, snowmelt, and streamflow measured in the same location within the transient snow zone. These data, combined with streamflow from the larger drainage basin downstream, provide the opportunity to address the following research questions:

1. How do rain-on-snow events differ in the response of snowmelt to precipitation?
2. How are differences in snowmelt during storm events related to climate, water available for runoff, and peak discharge?
3. How is the timing of precipitation related to the timing of snowmelt at multiple temporal scales during rain-on-snow events?

2. STUDY SITE AND METHODS

2.1. Study site description

The H.J. Andrews Experimental Forest is located on the western slope of the Oregon Cascades, and it comprises the 5th-order, westward-facing 6400-ha Lookout Creek basin (Figure 2.1). Elevation ranges from 410 m to 1630 m and slopes are typically steep (40% average), with subbasin slopes ranging from 25% to 60%. The geology and geomorphology of the Lookout Creek basin are both shaped by the region's volcanic past and recent geomorphic processes. Lava flows, ash flows, and other rocks of volcanic origin underlie most of the Andrews, with ridge-capping basalt flows occurring as recently as 4 million years ago. Since then glacial, fluvial, and mass wasting processes have shaped the Andrews' geomorphology. Glaciers carved out the u-shaped valleys seen in the upper elevations of the forest, while stream erosion and debris flows and slides are the dominant processes that shaped the steep, narrow valleys on the west side of the Andrews. Deep, slow-moving earthflows occupy central portions of the Andrews Forest and are characterized by flatter slopes (Swanson and James, 1975; Swanson and Swanston, 1977; Swanson and Jones, 2002).

The climate of the Andrews is marine west coast with cool, wet winters and warm, dry summers. More than 80% of precipitation occurs between November and April (Perkins and Jones, 2008). Mean annual precipitation (MAP) at the Central Meteorological Station (CS2MET) is 2200 mm and MAP is estimated to vary from 1900 mm at elevations of 400 to 700 m in the southwest corner of the Andrews Forest, to over 2900 mm along the southern bounding ridge of the Andrews Forest (Lookout Ridge, up to 1400 m elevation). However, benchmark climate stations are mostly located in a rain shadow north and east of Lookout Ridge (Perkins and Jones, 2008). CS2MET, the Hi-15 Meteorological Station (H15MET), the Vanilla Leaf Meteorological Station (VANMET), and Upper Lookout Meteorological Station (UPLMET) have 13 years (1999-2011) of complete, overlapping precipitation records. During this time CS2MET, H15MET, and VANMET all averaged ~2150

mm of precipitation per year. Only UPLMET received appreciably enhanced precipitation at 2580 mm per year (table 2.1).

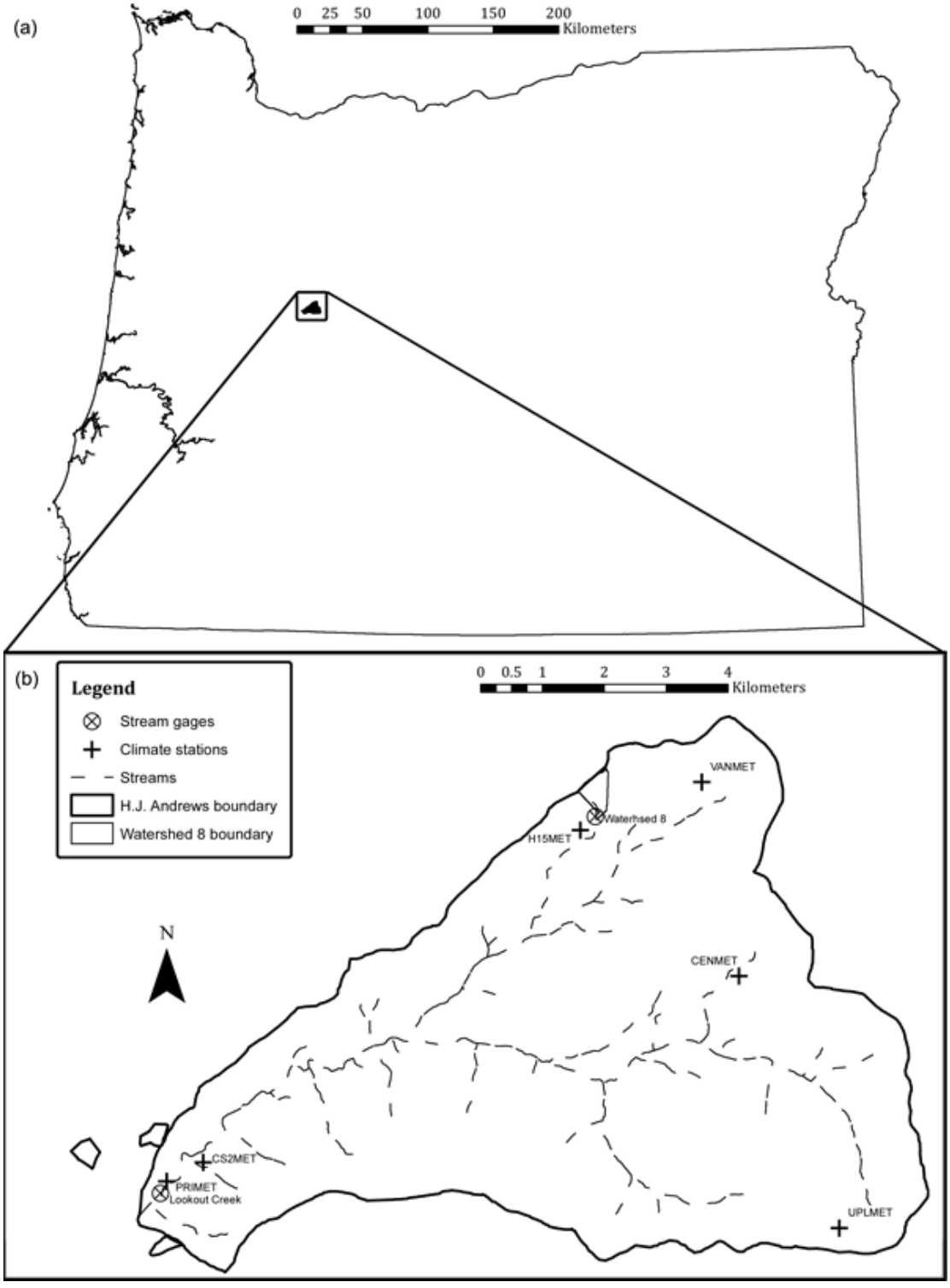

Figure 2.1. The location of the H.J. Andrews Experimental Forest within Oregon (a) and selected climate and streamflow stations in the study site (b).

Table 2.1. MAP (1999-2011) at four of the H.J. Andrews climate stations.

Met Station	Elevation (m)	Mean annual precipitation (mm)
CS2MET	482	2160
H15MET	909	2140
UPLMET	1298	2580
VANMET	1268	2150

Winter precipitation falls as a mix of rain and snow, with the percentage of snow increasing with elevation. Lower elevations in the Andrews (< 800 m) are in the transient snow zone and snowpacks rarely last longer than two weeks, while snowpacks at elevations above 800 m may last throughout the winter and into late spring. In addition, areas above 800 m experience more rain-on-snow events than low-elevation sites (Jones and Perkins, 2010).

Vegetation in the low-to-mid elevations of the Andrews (400 to 1050 m) is dominated by Douglas fir (*Pseudotsuga menziesii*), western hemlock (*Tsuga heterophylla*), and western red cedar (*Thuja plicata*). Upper elevations (above 1050 m) are composed of a mix of Pacific silver fir (*Abies amabilis*) and western hemlock, with some Douglas fir. Due to wildfires, most trees in the upper elevations are younger than the old growth in the lower elevations. Noble firs between 150 and 175 years old dominate the higher wildfire-affected stands (Franklin and Dyrness, 1971).

Soils at the Andrews are highly porous Inceptisols and Andisols (Brown and Parsons, 1973; Ranken, 1974). The infiltration rates of these soils are typically much higher than maximum precipitation rates, and therefore overland flow is not observed in the forest (Dyrness, 1969). Subsurface flow and channel interception are the two dominant pathways by which precipitation enters streams in the Andrews (Harr, 1977). Due to the region's maritime climate, frozen soils are only observed between 1 and 2 days per year (Jones and Perkins, 2010).

The Lookout Creek gage is at an elevation of 422 m. Approximately 25% of the basin has been affected by logging treatments such as clear-cuts and selective harvests. The majority of harvests and road installations were performed before 1970 and young stands range in age from 50 to 70 yrs. Several of the subbasins were

selectively harvested while others were 100% clear-cut (Jones and Grant, 1996).

Streamflow in the Andrews follows a distinct seasonal pattern with discharge peaking in the winter months—typically achieving maximum daily flow in December or January—and reaching a minimum in late summer. The highest flood peaks on Lookout Creek are typically caused by rain-on-snow events (Harr, 1981; Harr, 1986) and the largest flows occur between November and March. Discharge from the Andrews' subbasins follows the same general pattern, but the higher basins experience reduced December to January flows and augmented March to June flows due to rain shadow effects and spring snowmelt (Jones and Perkins, 2010).

WS8 is a 21.4-ha subbasin within the greater Lookout Creek basin that drains a small first-order stream in the northern section of the Andrews. Elevation in WS8 ranges from 970 to 1180 m. WS8 is one of the Andrews' unlogged control watersheds and its 150 to 500-yr-old stands are dominated by Douglas fir, western hemlock, and Pacific silver fir (Dyrness and Hawk, 1972). Slopes are relatively shallow, at a 25% average, and the basin has a southerly exposure.

2.2. Storm selection

Storms examined in this study are high-magnitude events, which are defined as those with 3-day precipitation totals greater than 150 mm at CS2MET and/or peak streamflow at Lookout Creek greater than 3.3 mm h^{-1}. The study period is limited to days in between 1992-03-12 and 2012-09-15, the dates for which both snowmelt lysimeter and dewpoint temperature data were available at H15MET, the station with longest continuously running snowmelt lysimeter. These criteria produced a total of 30 events, but 4 were removed due to missing snowmelt and/or dewpoint temperature data. The full list of events can be viewed in Appendix A. Additionally, each storm was analyzed using a 10-day window with the event's peak flow occurring on the 6^{th} day of the window. This window size was selected to encompass the entirety of each storm event without including potentially overlapping events, to provide a consistent scale of analysis among storms, to examine the temporal evolution of storms, and to minimize the edge effects of wavelet coherence.

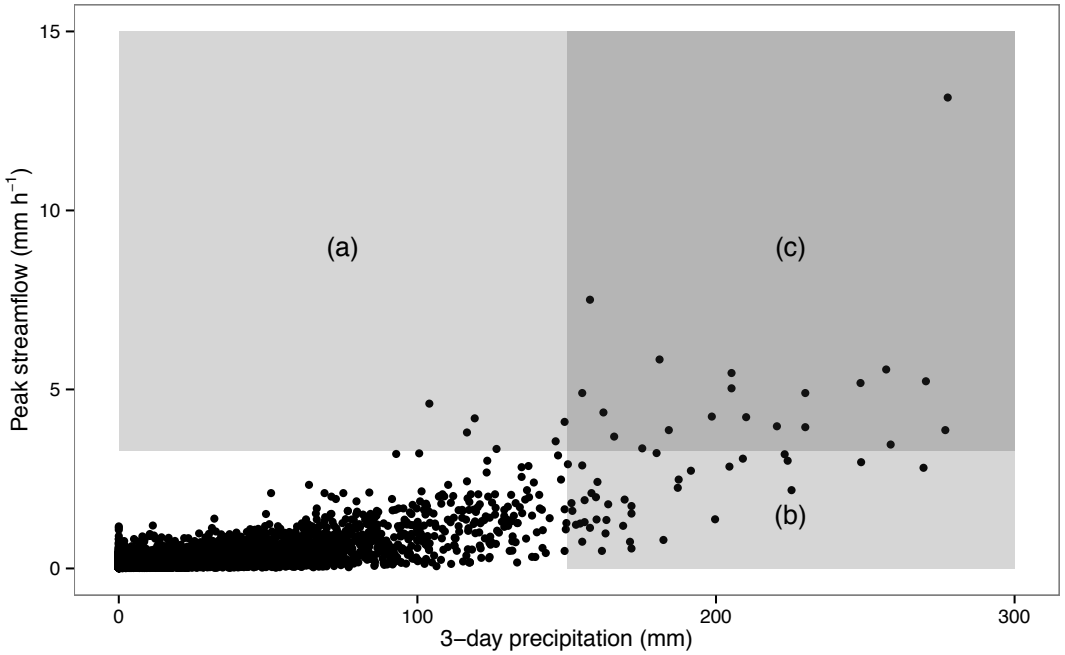

Figure 2.2. Storm selection. Shaded region (a) denotes events selected where peak streamflow was greater than 3.3 mm h^{-1}, (b) denotes events with 3-day precipitation greater than 150 mm, and (c) denotes the event met both criteria.

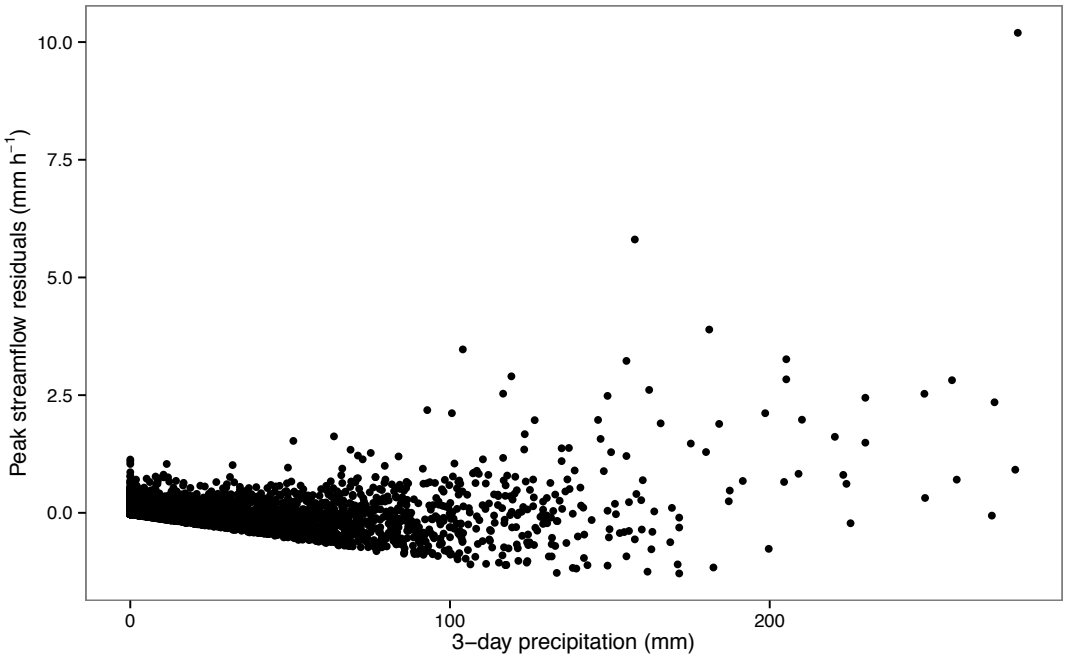

Figure 2.3. Residuals from the linear regression of peak streamflow as predicted by 3-day precipitation (*pkflow* = 0.04 + 0.01**ppt3day*; r^2 = 0.54). As 3-day precipitation increases, so does the magnitude of the residuals.

2.3. Data

2.3.1. Observed variables

Data from CS2MET, H15MET, VANMET, UPLMET, CENMET, WS8 and Lookout Creek were accessed through the forest's HF004 (Johnson and Rothacher, 2013) and MS001 (Daly and McKee, 2013) datasets, which are available on the Andrews website: http://andrewsforest.oregonstate.edu/. For further information on H.J. Andrews climate stations and available data, the reader is referred to the forest's website.

Streamflow data consisted of instantaneous streamflow data from Lookout Creek and one-hour streamflow data from WS8. Climate data consisted of air temperature, precipitation, dewpoint temperature, wind speed, and lysimeter output at 1-hour intervals from the H15MET.

Precipitation data at H15MET were obtained using an 8-inch diameter, heated raingage located 4.1 m above ground level with a pressure transducer and Campbell Scientific data logger. Measurements were taken every 10 seconds, summarized by 5-minute intervals, and recorded to the nearest 0.01 mm.

Snowmelt data were obtained from the H15MET snowmelt lysimeter, which is an open-topped wooden box (2.3 m x 2.3 m x 0.3 m) installed at ground level (Figures 2.4 and 2.5). The box is lined with hypalon rubber sheeting, and snowmelt is directed to a drain in the lowest corner of the lysimeter. The outflow empties into a tipping bucket gage, which records every 10 seconds using a CR10 recorder. Data are summarized at 5-minute intervals, and recorded to the nearest 0.01 mm.

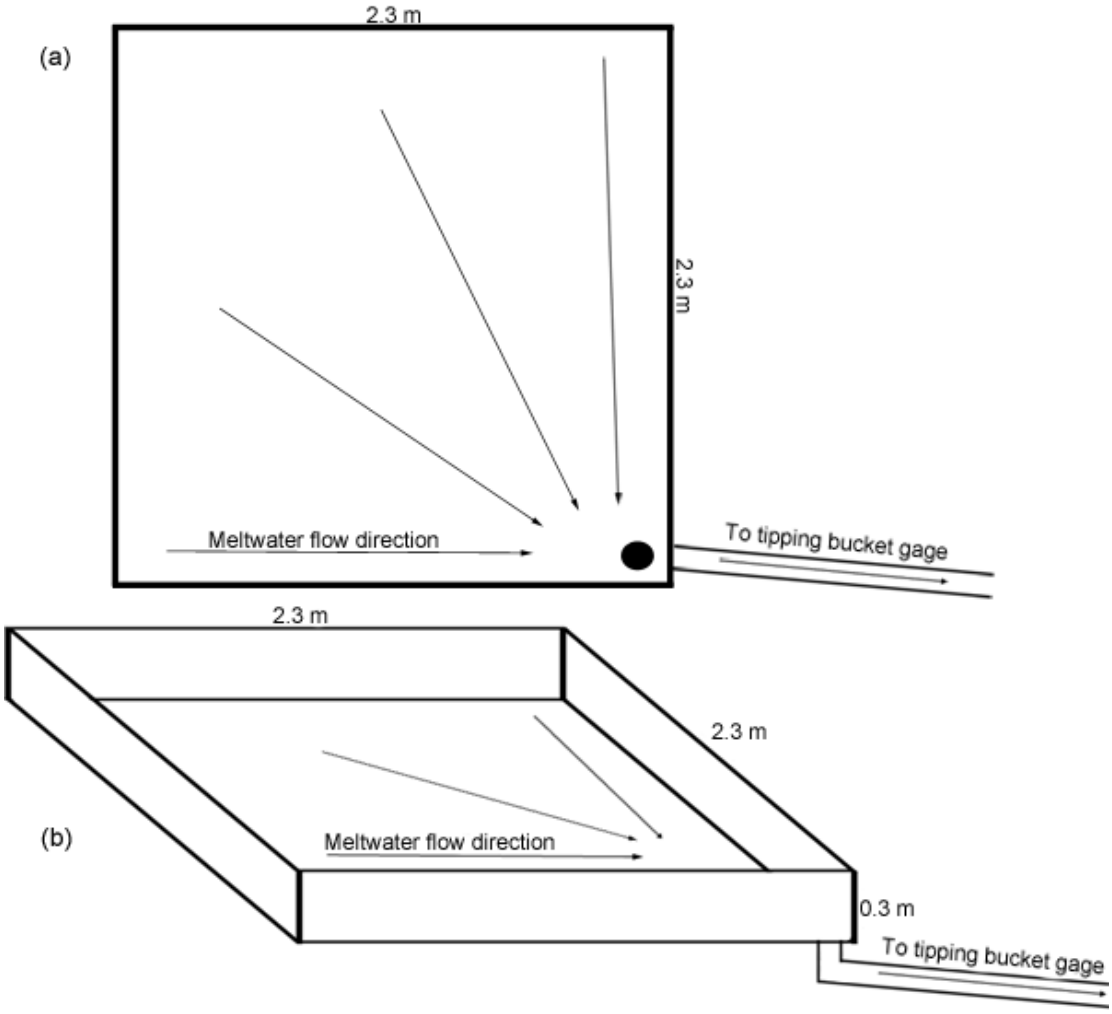

Figure 2.4. Top (a) and side (b) views of the H15MET snowmelt lysimeter.

Figure 2.5. H15MET instrumentation. Snowmelt lysimeter in foreground with shelter in background. Image courtesy of Al Levno, H.J. Andrews Experimental Forest.

Snowmelt data are available from the H15MET lysimeter from 1990-10-02 to 2012-09-15. Over the 22 years of snowmelt measurements, there are 6314 h (263.1 d) of missing data, which account for 3.3% of the dataset. The total gross output from the lysimeter is consistent with total precipitation as measured at H15MET on a water-year (October 1 through September 30) basis (Figure 2.6). Over the duration of overlapping precipitation and lysimeter records, the average per-water-year bias is 1.9×10^{-4} % with slightly more water being measured in the lysimeter than the precipitation gage (per-water-year bias ranged from -11.8% to 18.0%; $r^2 = 0.85$). On average, precipitation slightly exceeds total melt in years with precipitation < 2000 mm, but total melt exceeds precipitation in years with precipitation > 2000 mm. The differences could arise from the sublimation and evaporation of water from the lysimeter (when total water year lysimeter output < total water year precipitation) or from wind deposition of excess snow into the lysimeter (when total water year lysimeter output < total water year precipitation).

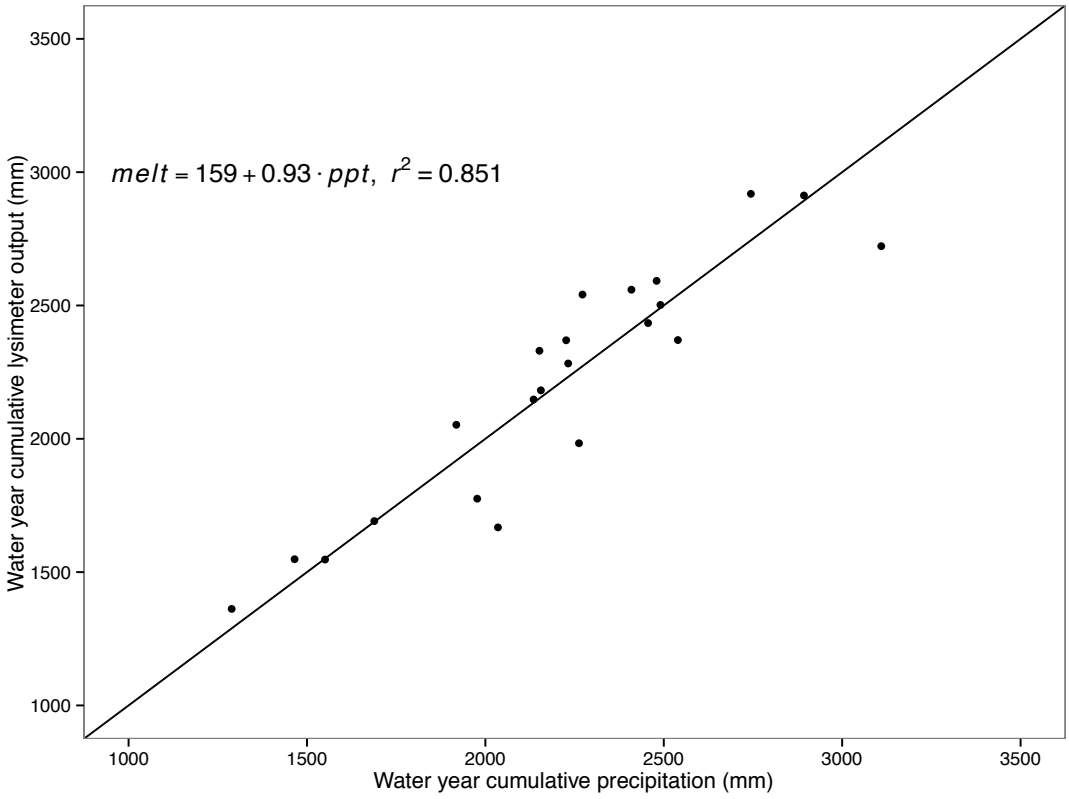

Figure 2.6. Cumulative lysimeter output plotted against cumulative precipitation per water year. Black line represents the linear regression of lysimeter output (*melt*) as predicted by precipitation (*ppt*).

Air temperature and relative humidity data were recorded using Campbell HMP35C (1992-03-12 to 2002-09-02) and HMP45C (2002-09-02 to present) probes located 4.5 m above ground level. Both probes utilize Vaisala capacitive relative humidity sensors, while the HMP35C uses a Fenwal Electronics thermistor and the HMP45C uses a platinum resistance thermometer to measure temperature. The precision for both instruments is +/- 2% and observations were recorded to the nearest 0.1°C and 0.1% using a Campbell Scientific data logger at 10-second intervals. Additionally, the MS001 dataset provides dewpoint temperature calculated from air temperature and relative humidity. Please visit the Andrews website for further documentation: http://andrewsforest.oregonstate.edu/lter/data/studies/ms01/meta/template.cfm?page=instlist&topnav=135#DEW_CALC.

Wind speed data were collected using an RM Young Model 05103 Wind Monitor located 5 m above ground level. The propeller-type anemometer has an operational range of 0 to 100 m s^{-1} and an accuracy range of ± 0.3 m s^{-1}. Hourly wind speed averages were recorded to the nearest 0.1 m s^{-1} using a Campbell Scientific data logger.

Snowpack data were collected at VANMET (1987-06-18 to 2006-11-05), UPLMET (1994-10-12 to 2009-07-14), and CENMET (1996-10-17 to 2007-01-25) using Park Mechanical pressure snow pillows and Druck pressure transducers installed at ground level (there is no snow pillow at H15MET). Observations were recorded hourly or every 5 minutes using a Campbell Scientific data logger.

In addition to sites in the Andrews, data from the three closest Natural Resources Conservation Service Snowpack Telemetry (SNOTEL) stations were included in the study: Jump Off Joe (1070 m), McKenzie (1450 m), and Roaring River (1510 m). These sites are all higher than H15MET, but were used to assess the presence/absence of a snowpack because of the narrow date range and number of missing observations of the snow pillows at the Andrews. The three SNOTEL stations use stainless-steel and hypalon snow pillows installed at ground level with Sensotec pressure transducers to measure snow water equivalent (SWE, the depth of liquid water contained in a snowpack). Data were summarized daily and recorded to the nearest 0.1 in.

2.3.2. Calculated variables

Net snowmelt was defined as:

$$Melt_{net}(t) = Lys_{out}(t) - P(t)$$

where Lys_{out} is the gross output from the snowmelt lysimeter and P is precipitation, both measured at time t. When $Melt_{net}$ is negative, moisture from precipitation is being held in the snowpack, i.e. SWE is increasing, and moisture is being released from the pack when $Melt_{net}$ is positive, i.e. SWE is decreasing. When $Melt_{net}$ is zero, either no precipitation/net snowmelt is occurring or the depth of precipitation at that

time step is equal to the moisture output from the snowpack, i.e. SWE remains constant.

Precipitation phase at H15MET was determined using dewpoint temperature in accordance with the methodology of Marks et al. (2013). Precipitation falling at a dewpoint temperature at or below -0.5°C was considered to be all snow, at or above 0.5°C all rain, and in between was considered mixed phase. To separate rain and snow totals in the mixed phase, a linear relationship was used where each 0.1°C rise above -0.5°C corresponded to a 10% increase in the percentage of rain falling (Figure 2.7). The phase data were used to color-code the precipitation-snowmelt "worm" plots (Chapter 3.1) and calculate the liquid-equivalent depth of snow and water that fell at H15MET during the study period.

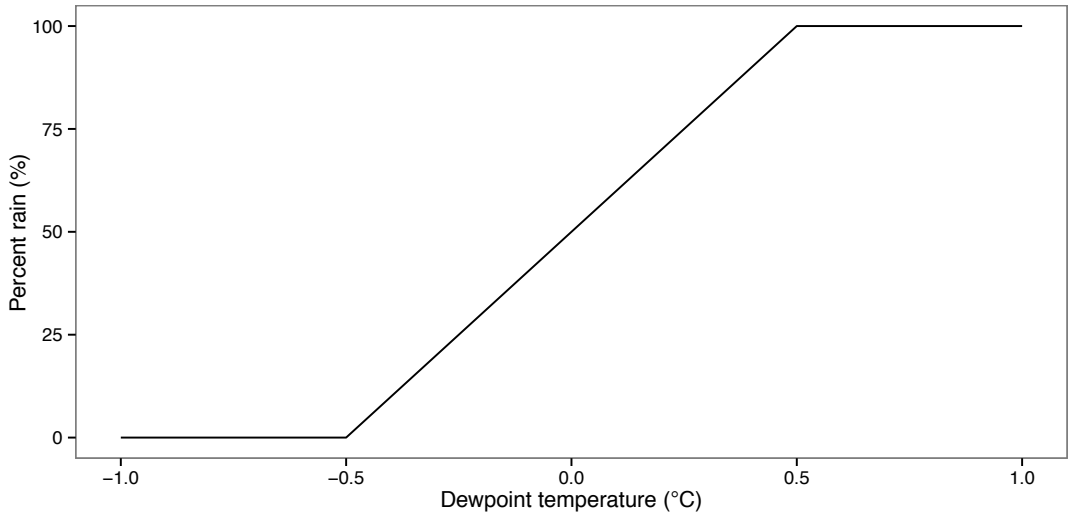

Figure 2.7. Percent rain as a function of dewpoint temperature. All precipitation below -0.5°C is classified as snow, while all precipitation above 0.5°C is classified as rain, with a linearly changing mix of the precipitation phases between the two threshold temperatures.

2.3.3. Cumulative and total variables

In addition to the observed and calculated data, cumulative and total variables were generated for each storm's 10-day window. Cumulative precipitation is the depth of precipitation (mm) accumulated up to time *t* in a storm. Cumulative net snowmelt is the depth of liquid water (mm) released by the snowpack—as calculated by $Melt_{net}$—up to time *t* in a storm. When cumulative net snowmelt is negative, water

has been retained within the snowpack up to that point in time (cumulative precipitation > cumulative gross lysimeter output) and water has been released by the snowpack when cumulative net snowmelt is positive (cumulative precipitation < cumulative gross lysimeter output).

In order to define snowmelt-response categories, "worm" plots were constructed with cumulative precipitation on the x-axis and cumulative net snowmelt on the y-axis. Each point represents an hourly observation, with a wider distance between points indicating more intense precipitation and/or melt. In addition, once the response categories were defined, the cumulative values were averaged for all storms in a given category at each time step to generate mean response plots. These plots are meant for illustration purposes and should not be interpreted as the predicted response for a given event.

Total precipitation and total net snowmelt are the sums of all hourly precipitation and net snowmelt values within the 10-day storm window. Total WAR is the sum of total precipitation and total net snowmelt. The total WAR-to-total precipitation ratio is calculated by dividing total WAR by total precipitation. The rain fraction is the proportion of precipitation that fell as rain during a storm, where 1 corresponds to an all-rain event and 0 corresponds to an all-snow event. Mean values for dewpoint temperature, air temperature, and wind speed are calculated by averaging hourly observations across the 10-day storm window.

2.3.4. Hourly melt rate categorization

Hourly net snowmelt rates were calculated for all hours in the dataset (n = 26 storms × 10 days × 24 hours = 6240 hourly rates) and categorized:

- None/gain: net snowmelt rate ≤ 0 mm h^{-1}
- Low: 0 mm h^{-1} < net snowmelt rate ≤ 1 mm h^{-1}
- Medium: 1 mm h^{-1} < net snowmelt rate ≤ 2 mm h^{-1}
- High: 2 mm h^{-1} < net snowmelt rate ≤ 3 mm h^{-1}
- Very high: 3 mm h^{-1} < net snowmelt rate

2.3.5. ANOVA and Tukey-Kramer test

The cumulative precipitation-cumulative net snowmelt "worm" plots described in Chapter 2.3.3 above were used to define response categories. An analysis of variance (ANOVA) was performed on the hydrologic and climatic data of the response categories to determine whether one of the categories was significantly different from the others. The Tukey-Kramer test was then used to assess the significance of all pairwise differences in means of the climatic and hydrologic variables of the response categories (Ramsay et al., 2013).

2.3.6. Data analysis and visualization

Data analysis was performed using R version 3.0.3 (R Core Team, 2014) with the RStudio version 0.98 interface (RStudio, 2013). R's base plotting routine, the ggplot2 package (Wickham, 2009), and gridExtra (Baptiste, 2012) were used to visualize the data. Additionally, the zoo (Zeilis and Grothendieck, 2005), xts (Ryan and Ulrich, 2014), and plyr (Wickham, 2011) packages were used for time series analysis and data management, and the multcomp (Hothorn et al., 2008) package was used for the Tukey-Kramer tests.

2.4. Wavelet analysis

2.4.1. Introduction

Wavelet analysis is an ideal tool for time series analysis in the geosciences. Much like traditional Fourier analysis, wavelet analysis can identify the dominant frequencies of variability within a dataset while also identifying the points in time where the strongest fluctuations occur. Fourier analysis presents results solely in the frequency space, while wavelet analysis presents results in time-frequency space, giving the researcher distinct advantages (e.g., noting when shifts in the data occur or visual trend identification). Furthermore, wavelet analysis is robust to non-stationary data, a common concern in the geosciences (Torrence and Compo, 1998).

The form of wavelet analysis applied here relies on the continuous wavelet transform, which utilizes a scaled mother wavelet to interpret variations in the data

across frequencies and time. Results from the analysis are presented via a 2-dimensional surface plot with the color denoting the power of the continuous wavelet transform at a given time and frequency. The mother wavelet, which can be simplified as a band-pass filter, is scaled based on time for each period of interest (Grinsted et al., 2004; Cazelles et al., 2008). At small periods, the mother wavelet is small in order to identify high-frequency variability in the data, and its scale increases with period to identify successively larger-scale data fluctuations. There are various choices of mother wavelets, but all must fit the criteria of having a mean of zero and being localized in time-frequency space (Farge, 1992). Additionally, the shape of the chosen mother wavelet should reflect the variation in the observed data (Torrence and Compo, 1998). Typically, the Morlet mother wavelet is used for geoscience applications as its profile is well suited to picking up fluctuations in smoothly varying data (Torrence and Compo, 1998) and it provides an acceptable compromise in time-frequency resolution (Grinsted et al., 2004).

Wavelet analysis has been used in a variety of geoscience studies, including: identifying multi-year variability in the El Niño Southern Oscillation (ENSO) (e.g., Gu and Philander, 1995; Wang and Wang, 1996; and Torrence and Compo, 1998); identifying multiple timescales of variability in central England temperature data (Baliunas et al., 1997); characterizing patterns of streamflow and their connection to precipitation in remote French Guyana catchments (Gaucherel, 2002); identifying the dominant timescales of variability of streamflow in the Amazon, Parana, Orinoco, and Congo Rivers (Labat et al., 2005); analyzing the temporal modes of variability for precipitation, temperature, and discharge on the Iberian peninsula (Andreo et al., 2006); and determining the temporal scales of variability for discharge from 55 of the world's largest rivers (Labat, 2008)

For research where the relationship between two variables is of interest, the cross wavelet transform and wavelet coherence are available. In essence, the cross wavelet transform is the product of the continuous wavelet transforms of the two time series and its use is relatively limited. The cross wavelet transform is not normalized and it is sensitive to large fluctuations in either series, which allows the method to produce regions of supposedly high common power even when the two variables are

independent (Maraun and Kurths, 2004; Schaefli et al., 2007). Therefore, care must be taken when interpreting the results of the cross wavelet transform. Generally, wavelet coherence, which uses information from the cross wavelet transform, should be used when examining the covariation of two variables in a dataset. Wavelet coherence acts as a localized correlation coefficient that allows the researcher to quantify the relationship between two variables at specific points in time and at multiple periods (Grinsted et al., 2004). This is accomplished by normalizing the squared cross wavelet transform by the product of the squared continuous wavelet transform of each time series, thus bounding the possible values between 0 (no relationship in the frequencies) and 1 (a perfect linear relationship) (Grinsted et al., 2004; Schaefli et al., 2007). Again, one must be careful when interpreting the results as a significant relationship may be presented in a wavelet coherence plot even when the two series are varying out of phase, i.e. variable *x* is increasing and *y* is decreasing. Although their frequencies may be similar, as indicated by a high wavelet coherence value, an increase in *x* is not accompanied by an increase in *y* (Grinsted et al., 2004). Therefore, one should note the phase when plotting wavelet values in order to present the whole picture.

Cross wavelet analysis and wavelet coherence have been used in a variety of geoscience studies, including: identifying the scales at which and the time periods when the Arctic Oscillation (AO) and Baltic Sea ice are coupled (Grinsted et al., 2004); examining the precipitation-temperature relationship during large flood events in the Swiss Alps (Schaefli et al., 2007); correlating climatic indices, such as the North Atlantic Oscillation, AO, Southern Oscillation, Pacific Decadal Oscillation, and ENSO, with annual continental freshwater discharge at various timescales (Labat, 2010); linking relative humidity to shortwave radiation measurements in the tropical Atlantic Ocean (Veleda et al., 2012); and relating precipitation to discharge in various northern hemisphere catchments at daily to seasonal timescales (Carey et al., 2013).

Wavelet coherence was chosen for this study because previous research has shown it to be uniquely suited to identifying the relationship between two variables over time and at multiple frequencies. Therefore it should provide valuable insight into the rainfall-snowmelt dynamics of selected storms.

2.4.2. Implementation and math

Wavelet analysis was performed using the biwavelet package for R (Gouhier, 2014), which is based on the WTC MATLAB package detailed in Grinsted et al. (2004) and the wavelet program outlined in Torrence and Compo (1998). The relevant equations and methodology are outlined below, but the reader is encouraged to see Torrence and Compo (1998), Grinsted et al. (2004), Labat (2005), and Cazelles et al. (2008) for further information. Plotting was done using R's base plot function with output generated by the biwavelet package.

Calculating wavelet coherence with the biwavelet package requires the following inputs:

1. Time series *x*: 1-hour precipitation as measured at H15MET
2. Time series *y*: 1-hour net snowmelt from the H15MET snowmelt lysimeter
3. Mother wavelet selection: Morlet
4. Number of Monte Carlo randomizations: 1000

One-hour precipitation and net snowmelt data from the 6 days preceding, the day of, and the 3 days following the peak flow for a given event were used to create a 10-day window with 240 unique observations. The mother wavelet chosen for this study was the Morlet wavelet for the reasons described above. In order to assess the significance of wavelet coherence, 1000 Monte Carlo randomizations were used against the null hypothesis of first-order autoregressive (AR1) noise.

The Morlet mother wavelet is defined by the following function:

$$\psi_0(\eta) = \pi^{-\frac{1}{4}} e^{i\varpi_0\eta} e^{-\frac{1}{2}\eta^2}$$

where i is the imaginary unit (the Morlet mother wavelet has both real and imaginary components), η is the unit-less time parameter and ϖ_0 is the unit-less frequency parameter. For the Morlet mother wavelet in this study $\varpi_0 = 6$ as it provides an effective compromise between time and frequency localization (Grinsted et al., 2004).

The Morlet mother wavelet is then used to calculate the continuous wavelet transform and cross-wavelet transform for the time series. The continuous wavelet transform for a time series x_n (from $n = 1$ to N) with a uniform timestep (δt) is:

$$W_n^X(s) = \sqrt{\frac{\delta t}{s}} \sum_{n'=1}^{N} x_{n'} \psi_0 \left[(n' - n) \frac{\delta t}{s} \right]$$

where s is the wavelet scale.

The cross wavelet transform for two time series is the complex conjugate of the continuous wavelet transforms for data series x and y:

$$W^{XY} = W^{XY} *$$

Wavelet coherence is then calculated as:

$$R_n^2(s) = \frac{\left| S\left(s^{-1} W_n^{XY}(s) \right) \right|^2}{S\left(s^{-1} \left| W_n^X(s) \right|^2 \right) \cdot S\left(s^{-1} \left| W_n^Y(s) \right|^2 \right)}$$

where S is the smoothing function. The value of wavelet coherence at a given point would always be 1 if the cross wavelet transform and continuous wavelet transforms were not smoothed in scale and time. For more information on smoothing functions, please see Torrence and Compo (1998) and Grinsted et al. (2004).

2.4.3. Interpreting the output: Zero-padding, the cone of influence, significance testing, and phase difference

As the period of analysis increases, the scale of the Morlet mother wavelet increases. This allows for the detection of multiple scales of fluctuations in the data, which is partially what makes wavelet analysis such an effective tool in the geosciences. However, as the scale of the mother wavelet increases, so does its overlap at the edge of the dataset (Torrence and Compo, 1998). Therefore, extra zero values are inserted at the beginning and end of the dataset at successively larger periods. As these zeros were not actually observed, it is essential that the sections of wavelet power and coherence that include these values (i.e., they were overlapped by

the mother wavelet) not be considered as actual results. A cone of influence (denoted by a white dashed line) is thus included in the plots to visually identify the regions free of edge effects. All power and coherence values within the cone were generated using only observed data.

Areas of significant wavelet coherence (at the 95% level) are bounded on the output plots by black contour lines. Significance values are computed by comparing 1000 Monte Carlo randomizations of wavelet coherence values to the null hypothesis of background red noise using the lag-1 autoregressive model (AR1), shown by Torrence and Compo (1998) to be effective at representing variability in the geosciences. The AR1 model is used to randomly generate two time series with lengths equal to the observed time series—240 data points in this case—and then wavelet coherence for the artificial data is calculated as above. The 1000 permutations are then used to create a 95% confidence limit based on a χ^2 distribution. Wavelet coherence values above this level in the observed dataset are said to be statistically significant.

Furthermore, the scale-dependent phase difference between the continuous wavelet transforms of the two variables is presented on the plot with black arrows. In addition to its other advantages, the Morlet mother wavelet is used here as only mother wavelets with imaginary components can be used to calculate the phase difference (Cazelles et al., 2008). The arrows point right when the two are in phase, left when in anti-phase, down when *x* leads *y*, and up when *y* leads *x*. The phase relationship is indicative of the physical processes occurring during the event. When power is increasing in *x* and decreasing in *y* (i.e., the two variables are in anti-phase), precipitation is increasing while net melt is decreasing, meaning precipitation is being stored in the snowpack. The phase differences were also extracted for days 4 through 7 and periods of 12 to 32 hours to examine the mid-storm, mid-period phase difference distribution per event. The selected time window encompasses each event's peak flow and main period of precipitation. The period range allows for an assessment of the phase relationship between precipitation and snowmelt at multiple temporal scales during the window.

3. RESULTS

3.1. Snowmelt response to cumulative precipitation and temperature

Five categories of cumulative net snowmelt response to cumulative precipitation were observed in the 26 storms at H15MET (Figure 3.1):

1. Flat (=): Net snowmelt fluctuates between positive and negative values over the course of the storm event, and cumulative net snowmelt is less than 10% of cumulative precipitation (n = 4).
2. Persistent melt (+): Cumulative net snowmelt increases with cumulative precipitation throughout most of the storm event (n = 7).
3. Persistent accumulation (-): Cumulative net snowmelt decreases with cumulative precipitation throughout most of the storm event (n = 6).
4. Late melt (-/+): Cumulative net snowmelt decreases, and then increases with cumulative precipitation throughout the storm event (n = 6).
5. Late accumulation (+/-): Cumulative net snowmelt initially rises or stays constant, but then declines with cumulative precipitation throughout the storm event (n = 3).

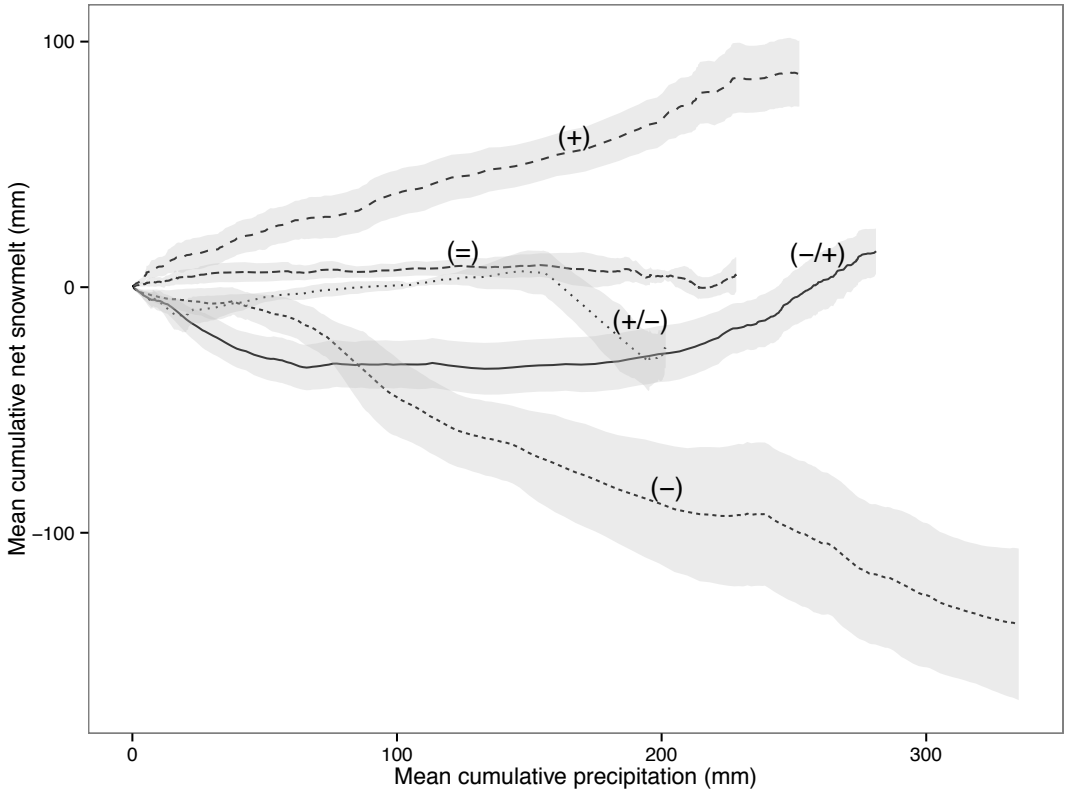

Figure 3.1. Cumulative net snowmelt as a function of cumulative precipitation, averaged for storms in each response category. When the slope of the response curve is negative, some precipitation is being retained by the snowpack. When the slope is positive, snowmelt augments precipitation. The grey shading denotes the standard error of cumulative net snowmelt for each response category.

Please see Appendix B and C for a complete listing of storm statistics, Appendix D for SWE data, and Appendix E for Lookout Creek streamflow, dewpoint temperature and wind speed.

3.1.1. Flat (=) category

Storms in the flat category experience small fluctuations in cumulative net snowmelt in response to cumulative precipitation (Figure 3.2). Maximum (minimum) net snowmelt contribution to total water available for runoff is less than 10% of cumulative total precipitation.

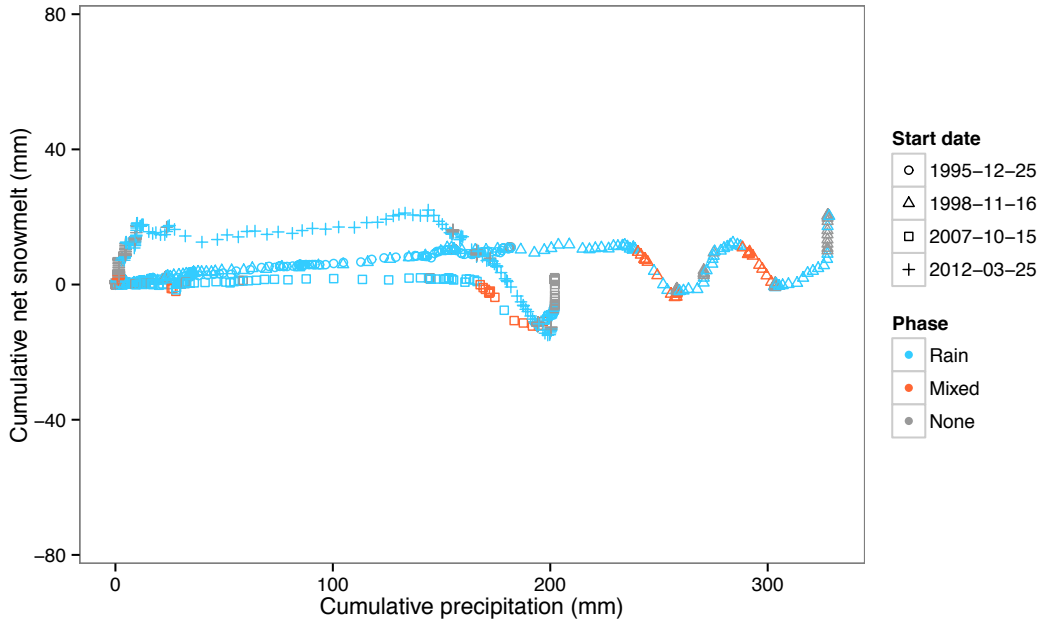

Figure 3.2. Cumulative net snowmelt as a function of cumulative precipitation for four storm events in the flat response category. Each point corresponds to an hourly observation; therefore, points spaced farther apart in the horizontal (vertical) are indicative of higher rates of precipitation (net snowmelt).

The 1995-12-25 storm event received the lowest total precipitation (182.1 mm) in this category, and total net snowmelt was 11.0 mm (6% of cumulative precipitation). Dewpoint temperature was typically < 0.5°C in the first three days of the 10-day window, but no precipitation fell. On day 4, dewpoint temperature rose to > 0.5°C and all of the precipitation in the event fell as rain. Wind speed was < 0.4 m s^{-1} during most of the event, but rose to > 0.6 m s^{-1} during the period of precipitation. Peak streamflow was 1.5 and 2.0 mm h^{-1} at WS8 and Lookout Creek (Figure 3.3, Table 3.1).

The 1998-11-16 storm received the highest total precipitation (328.3 mm) in this category, and total net snowmelt was 20.2 mm. Dewpoint temperature was

typically > 0.5°C, with two periods below the mixed-phase threshold during days 7 and 9, and nearly all precipitation fell as rain. Wind speed fluctuated between 0 and 0.8 m s^{-1} throughout the event. Peak streamflow was 2.1 and 3.0 mm h^{-1} at WS8 and Lookout Creek (Figure 3.3, Table 3.1).

The 2007-10-15 storm received the second lowest total precipitation (202.0 mm) in this category, and total net snowmelt was 2.0 mm. Dewpoint temperature was typically > 0.5°C, with two periods below the mixed-phase threshold during days 3 and 6, and nearly all precipitation fell as rain. Wind speed fluctuated between 0 and 0.6 m s^{-1} throughout the event with one spike over 0.8 m s^{-1}. Peak streamflow was 1.1 and 0.6 mm h^{-1} at WS8 and Lookout Creek (Figure 3.3, Table 3.1).

The 2012-3-25 storm received the lowest total precipitation (200.5 mm) in this category, and total net snowmelt was -12.5 mm. Dewpoint temperature observations during this storm were storm were erroneously high (> 30°C). Wind speed fluctuated between 0 and 0.6 m s^{-1} throughout the event. Peak streamflow was 3.1 and 3.8 mm h^{-1} at WS8 and Lookout Creek (Figure 3.3, Table 3.1).

Table 3.1. Selected climatic and hydrologic data for storms in the flat category. *Dewpoint data removed due to error in measurement.

Start date	Total ppt. (mm)	Total net melt (mm)	Total WAR (mm)	Mean dew. temp. (°C)	Mean wind speed (m s^{-1})	WS8 peak flow (mm h^{-1})	Lookout Creek peak flow (mm h^{-1})
1995-12-25	182.1	11.0	193.1	3.8	0.2	1.5	2.0
1998-11-16	328.3	20.2	348.5	3.2	0.2	2.1	3.0
2007-10-15	202.0	2.0	204.1	6.0	0.1	1.1	0.6
2012-03-25	200.5	-12.5	187.9	31.7*	0.2	3.1	3.8

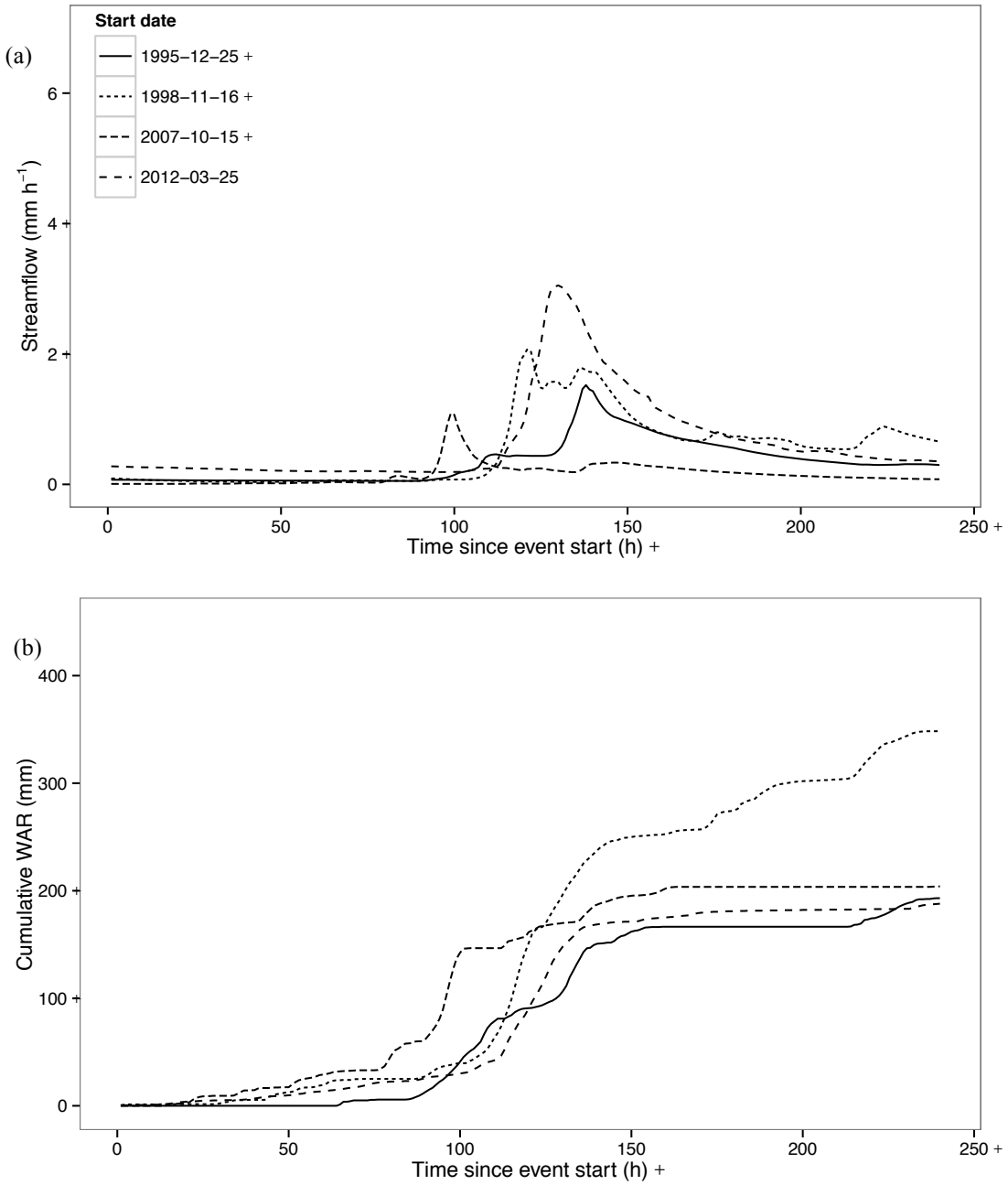

Figure 3.3. WS8 streamflow (a) and cumulative WAR (b) plotted against time for each event in the flat response category. The steepness of the cumulative WAR line represents combined snowmelt and precipitation intensity.

3.1.2. Persistent melt (+) category

The seven events in the persistent net snowmelt category are characterized by more or less continuously positive net snowmelt with only brief periods of net water absorption by the snowpack when dewpoint temperature fell below 0.5°C (Figure 3.4).

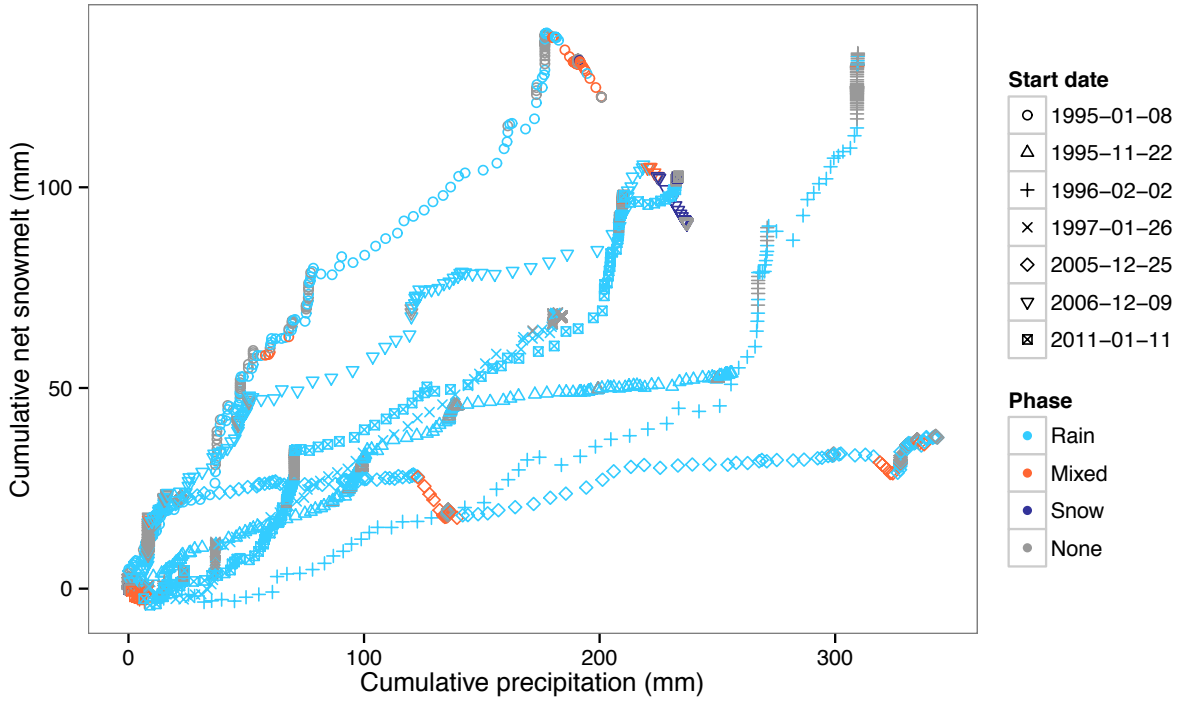

Figure 3.4. Cumulative net snowmelt as a function of cumulative precipitation for seven storm events in the persistent melt response category. Each point corresponds to an hourly observation; therefore, points spaced farther apart in the horizontal (vertical) are indicative of higher rates of precipitation (net snowmelt).

The 1995-01-08 storm received the second lowest total precipitation (200.8 mm) in this category, and total net snowmelt was 122.5 mm. Dewpoint temperature was typically > 0.5°C, with a pronounced decrease on day 8 below the mixed-phased threshold. Wind speed fluctuated between 0 and 1.0 m s^{-1} in the event's opening 3 days before tapering off to less than 0.5 m s^{-1}. Peak streamflow was 2.4 and 2.9 mm h^{-1} at WS8 and Lookout Creek (Figure 3.5, Table 3.2).

The 1995-11-26 storm received the 3rd highest total precipitation (256.1 mm) in this category, and total net snowmelt was 53.7 mm. Dewpoint temperature was > 0.5°C throughout the event, and all precipitation fell as rain. Wind speed fluctuated

between 0 and 0.8 m s^{-1} throughout the event. Peak streamflow was 1.5 and 1.6 mm h^{-1} at WS8 and Lookout Creek (Figure 3.5, Table 3.2).

The 1996-02-02 storm received the second highest total precipitation (309.6 mm) in this category, and total net snowmelt was 133.4 mm. Dewpoint temperature was typically > 0.5°C, with two periods below the mixed-phase threshold during days 1, 2 and 9, and nearly all precipitation fell as rain. Wind speed stayed a constant 0.5 to 0.6 m s^{-1} days 4 through 7 with lower values before and higher after. Peak streamflow was 6.6 and 13.2 mm h^{-1} at WS8 and Lookout Creek (Figure 3.5, Table 3.2).

The 1997-01-26 storm received the lowest total precipitation (184.1 mm) in this category, and total net snowmelt was 68.1 mm. Dewpoint temperature was typically > 0.5°C, with two periods below the mixed-phase threshold during days 2 and 9, and nearly all precipitation fell as rain. Wind speed fluctuated between 0 and 0.8 m s^{-1} throughout the event with a spike above 1.0 m s^{-1} on day 10. Peak streamflow was 2.6 and 3.6 mm h^{-1} at WS8 and Lookout Creek (Figure 3.5, Table 3.2).

The 2005-12-27 storm received the highest total precipitation (343.3 mm) in this category, and total net snowmelt was 37.7 mm. Dewpoint temperature was typically > 0.5°C, with three periods below the mixed-phase threshold during days 5, 7 and 10, and nearly all precipitation fell as rain. Wind speed fluctuated between 0 and 0.8 m s^{-1} throughout the event with a spike above 1.0 m s^{-1} on day 8. Peak streamflow was 3.7 and 5.0 mm h^{-1} at WS8 and Lookout Creek (Figure 3.5, Table 3.2).

The 2006-12-09 storm received the median total precipitation (237.1 mm) in this category, and total net snowmelt was 91.1 mm. Dewpoint temperature was > 0.5°C days 1 through 6 before dropping below -0.5 °C on day 7, and nearly all precipitation fell as rain (little precipitation occurred following the transition to colder temperatures). Wind speed fluctuated between 0 and 1.5 m s^{-1} days 1 through 6 before dropping to 0.0 m s^{-1} on day 7. Peak streamflow was 4.0 and 3.7 mm h^{-1} at WS8 and Lookout Creek (Figure 3.5, Table 3.2).

The 2011-01-11 storm received the third lowest total precipitation (233.5 mm) in this category, and total net snowmelt was 102.8 mm. Dewpoint temperature was typically > 0.5°C, with two periods below the mixed-phase threshold during days 1 and 10, and nearly all precipitation fell as rain. Wind speed fluctuated between 0 and 0.3 m s^{-1} days 2 through 7. Peak streamflow was 3.9 and 7.5 mm h^{-1} at WS8 and Lookout Creek (Figure 3.5, Table 3.2).

Table 3.2. Selected climatic and hydrologic data for storms in the persistent melt category.

Start date	Total ppt. (mm)	Total net melt (mm)	Total WAR (mm)	Mean dew. temp. (°C)	Mean wind speed (m s^{-1})	WS8 peak flow (mm h^{-1})	Lookout Creek peak flow (mm h^{-1})
1995-01-08	200.8	122.5	323.3	1.9	0.3	2.4	2.9
1995-11-22	256.1	53.7	309.8	6.4	0.2	1.5	1.6
1996-02-02	309.6	133.4	443.1	1.3	0.5	6.6	13.2
1997-01-26	184.1	68.1	252.1	2.8	0.2	2.6	3.6
2005-12-25	343.3	37.7	381.0	3.1	0.2	3.7	5.0
2006-12-09	237.1	91.1	328.2	0.1	0.2	4.0	3.7
2011-01-11	233.5	102.8	336.2	1.9	0.1	3.9	7.5

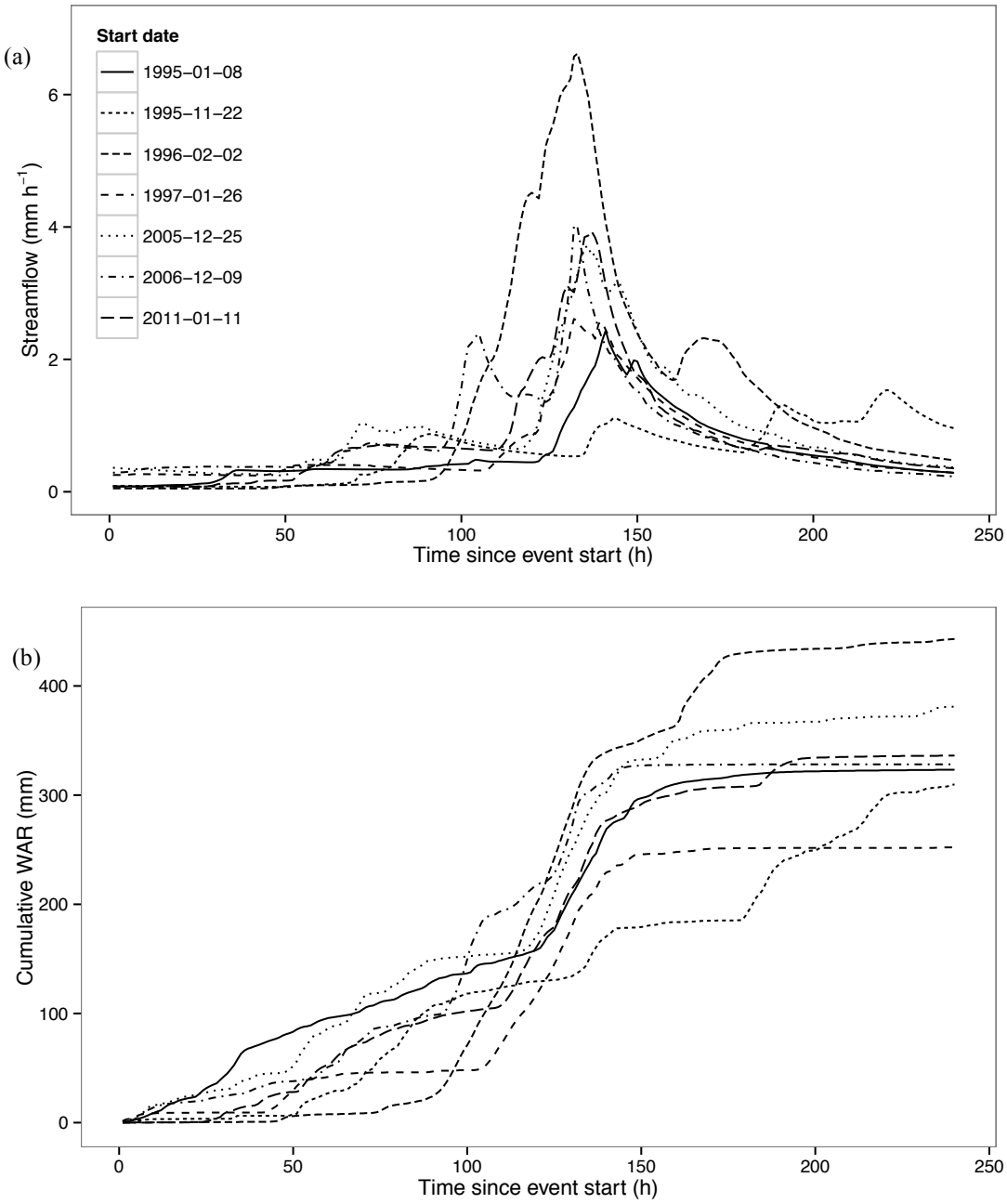

Figure 3.5. WS8 streamflow (a) and cumulative WAR (b) plotted against time for each event in the persistent melt response category. The steepness of the cumulative WAR line represents combined snowmelt and precipitation intensity.

3.1.3. Persistent accumulation (-) category

Net snowmelt is a more or less continuously declining function of cumulative precipitation in the six events in the persistent accumulation category (Figure 3.6). This category is characterized by dewpoint temperature < 0.5°C, snow and mixed-phase precipitation, and low water available for runoff with short periods of dewpoint temperature > 0.5°C and rain.

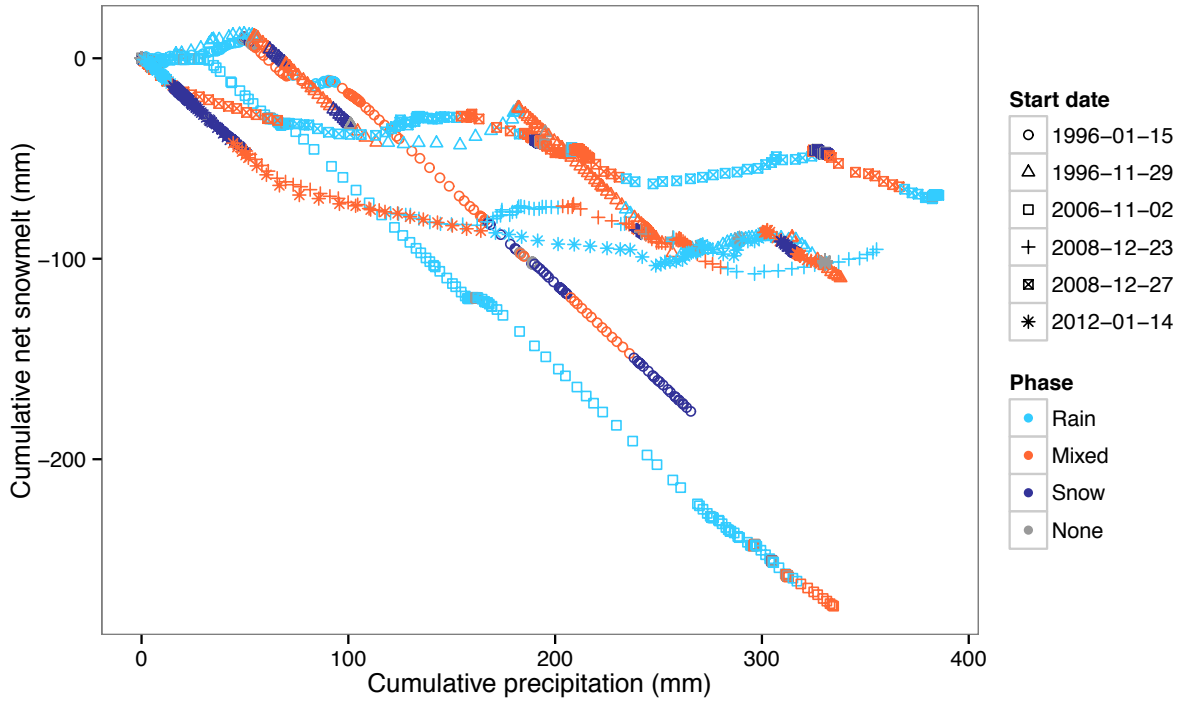

Figure 3.6. Cumulative net snowmelt as a function of cumulative precipitation for six storm events in the persistent accumulation response category. Each point corresponds to an hourly observation; therefore, points spaced farther apart in the horizontal (vertical) are indicative of higher rates of precipitation (net snowmelt).

The 1996-01-15 storm received the lowest total precipitation (265.6 mm) in this category, and total net snowmelt was -176.2 mm. Dewpoint temperature was typically < 0.5°C, with two periods above the mixed-phase threshold during days 1, 2, and 5, and precipitation was nearly split between rain (57%) and snow (43%). Wind speed fluctuated between 0 and 1.0 m s^{-1} days 1 through 5 before the measurements cut out. Peak streamflow was 0.6 and 0.7 mm h^{-1} at WS8 and Lookout Creek (Figure 3.7, Table 3.3).

The 1996-11-29 storm received the third highest total precipitation (338.0 mm) in this category, and total net snowmelt was -109.6 mm. Dewpoint temperature was typically < 0.5°C, with three periods above the mixed-phase threshold during days 1 and 2, 6 and 7, and 9 and 10, and precipitation was mostly rain (81%). Wind speed fluctuated between 0 and 1.0 m s^{-1} throughout the event, but there were several periods of missing observations. Peak streamflow was 2.5 and 3.3 mm h^{-1} at WS8 and Lookout Creek (Figure 3.7, Table 3.3).

The 2006-11-02 storm received the third lowest total precipitation (334.7 mm) in this category, and total net snowmelt was -273.3 mm. Dewpoint temperature was > 0.5°C days 1 through 7, with three periods below the mixed-phase threshold during days 8 through 10, and precipitation was nearly all rain. Wind speed fluctuated between 0 and 0.6 m s^{-1} throughout the event. Peak streamflow was 1.2 and 1.9 mm h^{-1} at WS8 and Lookout Creek (Figure 3.7, Table 3.3).

The 2008-12-23 storm received the second highest total precipitation (355.4 mm) in this category, and total net snowmelt was -95.3 mm. Dewpoint temperature was typically < 0.5°C, with two periods above the mixed-phase threshold during days 6 and 10, and precipitation was mostly rain (70%). Wind speed was 0 m s^{-1} days 1 through 5 and had two periods of up to 0.8 m s^{-1} on days 6,7, and 10. Peak streamflow was 2.9 and 3.2 mm h^{-1} at WS8 and Lookout Creek (Figure 3.7, Table 3.3).

The 2008-12-27 storm received the highest total precipitation (385.6 mm) in this category, and total net snowmelt was -68.3 mm. Dewpoint temperature was typically < 0.5°C, with two periods above the mixed-phase threshold during days 2, 6 and 7, and precipitation was mostly rain (80%). Wind speed was 0 m s^{-1} most days with two periods of up to 0.8 m s^{-1} on days 2 and 3 and 6 and 7. Peak streamflow was 2.9 and 4.6 mm h^{-1} at WS8 and Lookout Creek (Figure 3.7, Table 3.3). (Note: 2008-12-23 and 2008-12-27 shared six days of overlap, but both were included as they each registered that met the storm selection criteria).

The 2012-01-14 storm received the second lowest total precipitation (330.5 mm) in this category, and total net snowmelt was -101.0 mm. Dewpoint temperature was typically < 0.5°C, except for erroneous measurements on days 1 and 2 and a period above the mixed-phase threshold on days 7 and 8. Precipitation was nearly

split between rain (57%) and snow (43%). Wind speed was typically 0 m s^{-1} days 1 through 5 before peaking above 0.5 m s^{-1} days 6 through 8. Peak streamflow was 2.7 and 3.5 mm h^{-1} at WS8 and Lookout Creek (Figure 3.7, Table 3.3).

Table 3.3. Selected climatic and hydrologic data for storms in the persistent accumulation category.

Start date	Total ppt. (mm)	Total net melt (mm)	Total WAR (mm)	Mean dew. temp. (°C)	Mean wind speed (m s^{-1})	WS8 peak flow (mm h^{-1})	Lookout Creek peak flow (mm h^{-1})
1996-01-15	265.6	-176.2	89.4	0.1	0.3	0.6	0.7
1996-11-29	338.0	-109.6	228.4	0.4	0.1	2.5	3.3
2006-11-02	334.7	-273.3	61.4	6.3	0.1	1.2	1.9
2008-12-23	355.4	-95.3	260.1	-0.6	0.1	2.9	3.2
2008-12-27	385.6	-68.3	317.2	-0.5	0.1	2.9	4.6
2012-01-14	330.5	-101.0	229.5	4.0	0.1	2.7	3.5

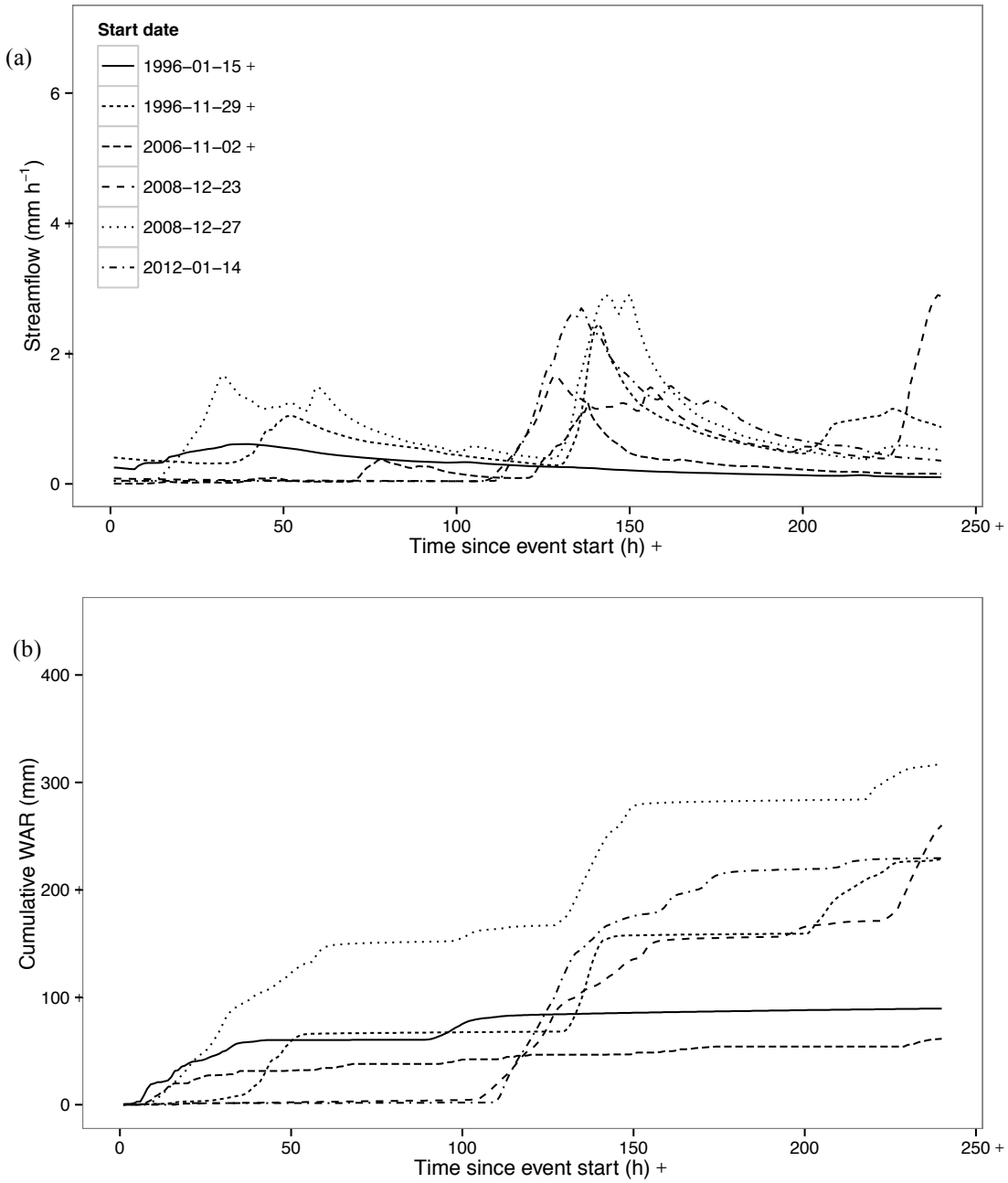

Figure 3.7. WS8 streamflow (a) and cumulative WAR (b) plotted against time for each event in the persistent accumulation response category. The steepness of the cumulative WAR line represents combined snowmelt and precipitation intensity.

3.1.4. Late melt (-/+) category

An initial period of snowpack absorption of precipitation followed by a later period of snowmelt defines the six events in the late melt category (Figure 3.8). This category is characterized by initial dewpoint temperature < 0.5°C, snow and mixed-phase precipitation and negative net snowmelt, followed by a multi-day period of dewpoint temperature > 0.5°C, rain, and positive net snowmelt.

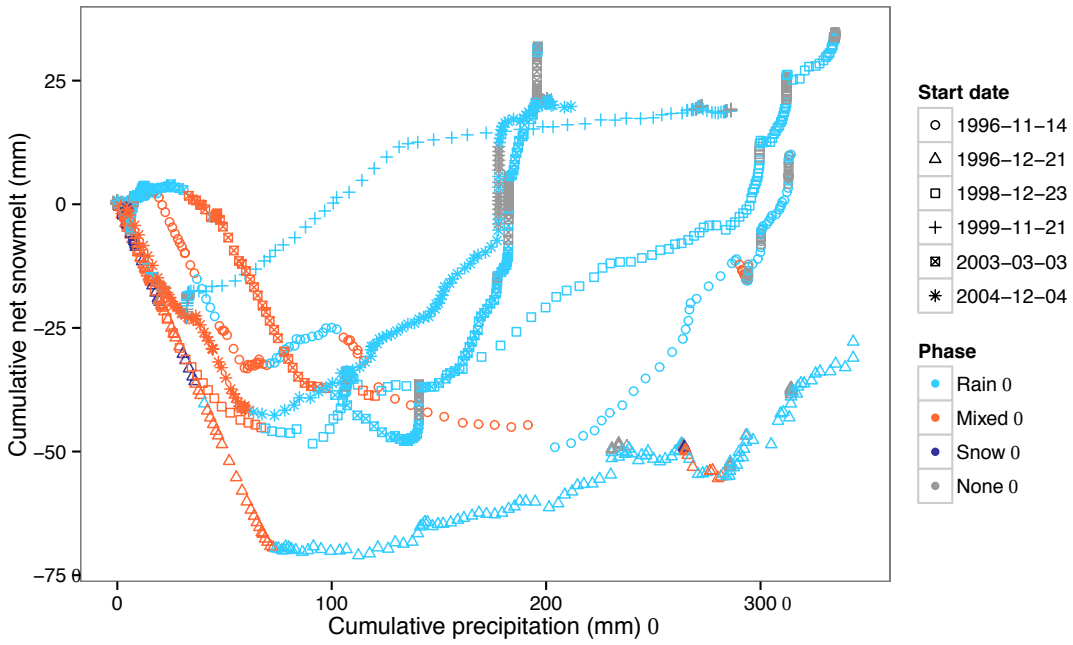

Figure 3.8. Cumulative net snowmelt as a function of cumulative precipitation for six storm events in the late melt response category. Each point corresponds to an hourly observation; therefore, points spaced farther apart in the horizontal (vertical) are indicative of higher rates of precipitation (net snowmelt).

The 1996-11-14 storm received the third highest total precipitation (314.2 mm) in this category, and total net snowmelt was 10.1 mm. Dewpoint temperature was near 0.5°C days 1 through 5 before rising on day 6, and precipitation was primarily rain. Wind speed fluctuated between 0 and 0.3 m s^{-1} for most of the events with spikes above 0.6 m s^{-1} on days 4 and 6. Peak streamflow was 4.4 and 4.9 mm h^{-1} at WS8 and Lookout Creek (Figure 3.9, Table 3.4).

The 1996-12-21 storm received the highest total precipitation (343.2 mm) in this category, and total net snowmelt was -27.8 mm. Dewpoint temperature was typically < 0.5°C days 1 through 4 before rising on the latter part of day 4, and

precipitation was primarily rain. Wind speed fluctuated between 0 and 0.6 m s^{-1} for most of the event. Peak streamflow was 3.3 and 3.9 mm h^{-1} at WS8 and Lookout Creek (Figure 3.9, Table 3.4).

The 1998-12-23 storm received the second highest total precipitation (334.8 mm) in this category, and total net snowmelt was 34.7 mm. Dewpoint temperature was < 0.5°C days 1 through 3 (with periods < 5.0°C on days 1 and 2) before rising on day 4, and precipitation was primarily rain. Wind speed fluctuated between 0 and 0.6 m s^{-1} for most of the event with a maximum over 1.0 m s^{-1} on days 5 and 6. Peak streamflow was 3.4 and 5.6 mm h^{-1} at WS8 and Lookout Creek (Figure 3.9, Table 3.4).

The 1999-11-21 storm received the third lowest total precipitation (286.2 mm) in this category, and total net snowmelt was 19.3 mm. Dewpoint temperature was typically < 0.5°C days 1 through 3 before rising on day 4, and precipitation was primarily rain. Wind speed was 0 m s^{-1} days 1 through 3 and fluctuated between 0 and 1.0 m s^{-1} from day 4 on. Peak streamflow was 2.9 and 5.2 mm h^{-1} at WS8 and Lookout Creek (Figure 3.9, Table 3.4).

The 2003-03-03 storm received the lowest total precipitation (196.1 mm) in this category, and total net snowmelt was 31.9 mm. Dewpoint temperature fluctuated around 0.5°C days 1 through 5 before rising on the latter part of day 5, and precipitation was primarily rain. Wind speed fluctuated between 0 and 0.8 m s^{-1} throughout the event. Peak streamflow was 1.0 and 1.3 mm h^{-1} at WS8 and Lookout Creek (Figure 3.9, Table 3.4).

The 2004-12-04 storm received the second lowest total precipitation (211.6 mm) in this category, and total net snowmelt was 19.8 mm. Dewpoint temperature was typically < 0.5°C days 1 through 4 before rising on day 5, and precipitation was primarily rain. Wind speed was generally 0 m s^{-1} days 1 through 4 and then fluctuated between 0 and 0.8 m s^{-1} for the rest of the event with a spike to 1.5 m s^{-1} on day 9. Peak streamflow was 1.2 and 1.9 mm h^{-1} at WS8 and Lookout Creek (Figure 3.9, Table 3.4).

Table 3.4. Selected climatic and hydrologic data for storms in the late melt category.

Start date	Total ppt. (mm)	Total net melt (mm)	Total WAR (mm)	Mean dew. temp. (°C)	Mean wind speed ($m\ s^{-1}$)	WS8 peak flow ($mm\ h^{-1}$)	Lookout Creek peak flow ($mm\ h^{-1}$)
1996-11-14	314.2	10.1	324.2	1.9	0.1	4.4	4.9
1996-12-21	343.2	-27.8	315.4	1.4	0.4	3.3	3.9
1998-12-23	334.8	34.7	369.5	0.4	0.2	3.4	5.6
1999-11-21	286.2	19.3	305.4	3.5	0.2	2.9	5.2
2003-03-03	196.1	31.9	228.0	2.2	0.2	1.0	1.3
2004-12-04	211.6	19.8	231.4	2.6	0.2	1.2	1.9

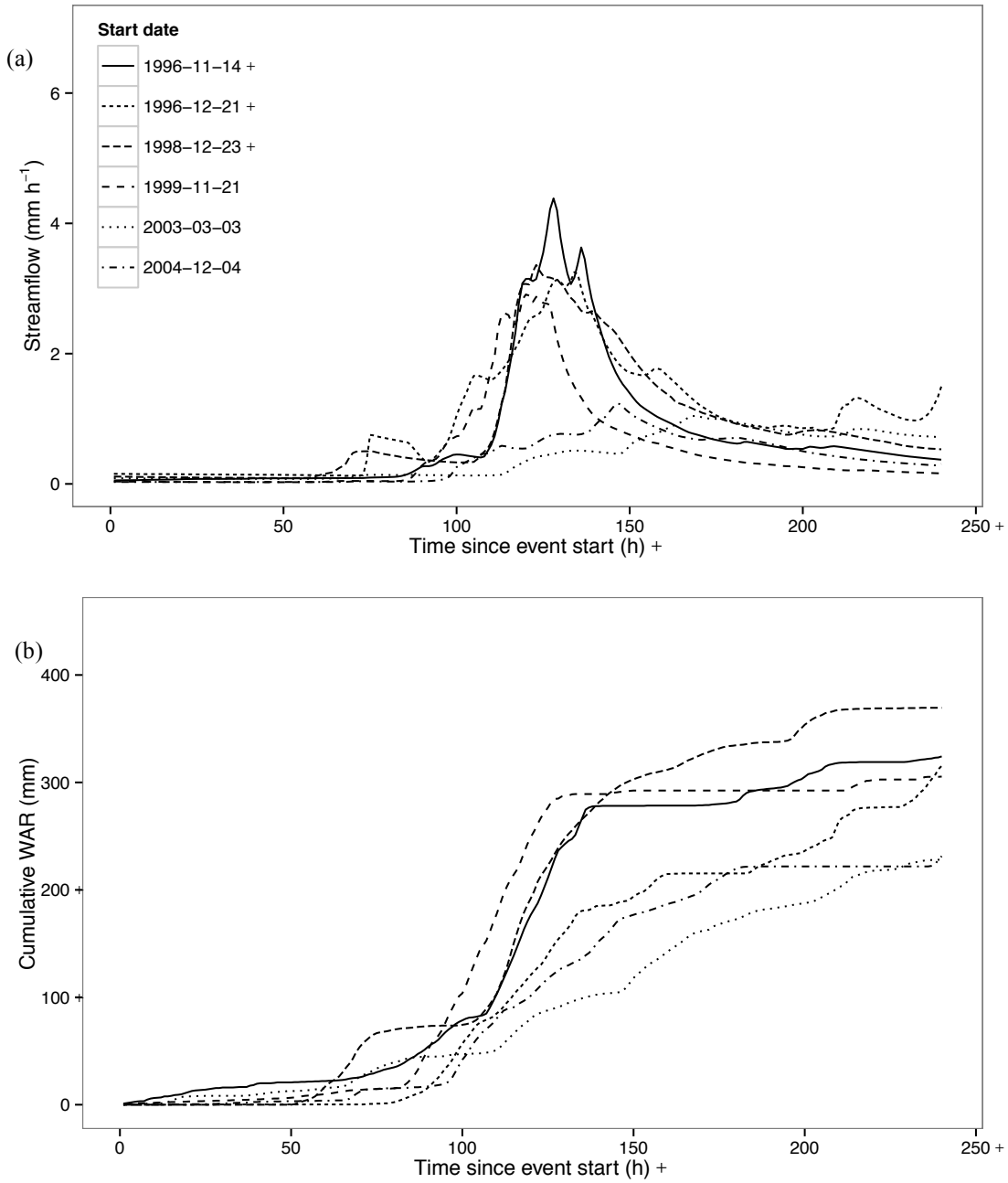

Figure 3.9. WS8 streamflow (a) and cumulative WAR (b) plotted against time for each event in the late melt response category. The steepness of the cumulative WAR line represents combined snowmelt and precipitation intensity.

3.1.5. Late accumulation (+/-) category

The three events in the late accumulation category are characterized by early periods of flat or increasing cumulative net snowmelt and late periods of snowpack accumulation triggered by changes in precipitation phase, which is controlled by dewpoint temperature (Figure 3.10).

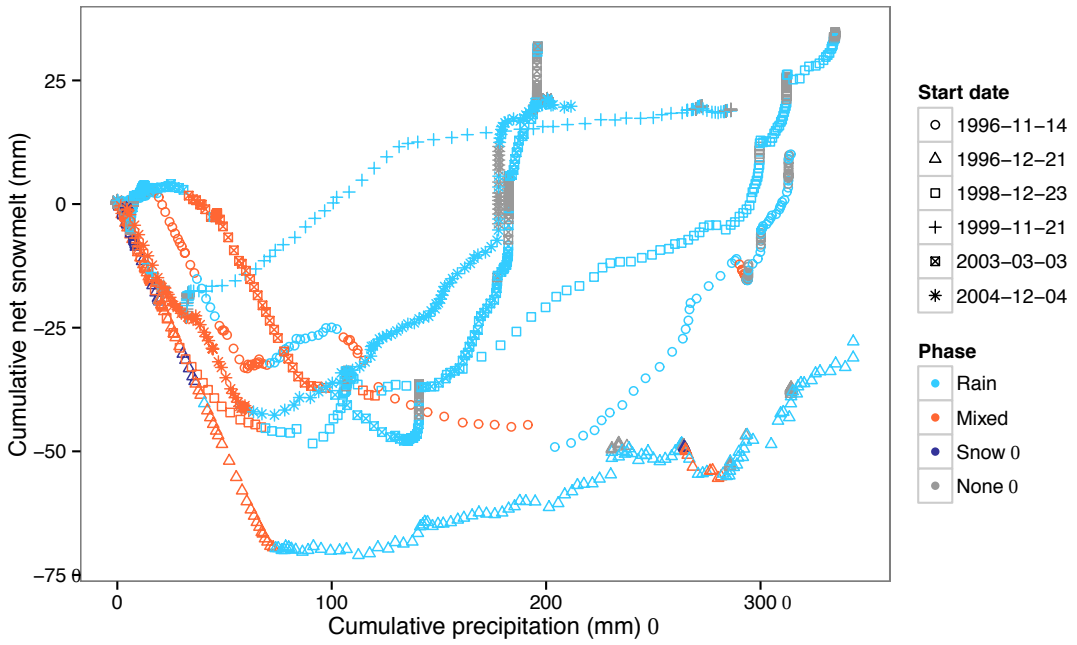

Figure 3.10. Cumulative net snowmelt as a function of cumulative precipitation for six storm events in the late melt response category. Each point corresponds to an hourly observation; therefore, points spaced farther apart in the horizontal (vertical) are indicative of higher rates of precipitation (net snowmelt).

The 2003-12-08 storm received the lowest total precipitation (193.0 mm) in this category, and total net snowmelt was -8.9 mm. Dewpoint temperature fluctuated above and below 0.5°C days 1 through 6 before falling on day 7, and precipitation was mostly rain (72%). Wind speed fluctuated between 0 and 0.8 m s^{-1} throughout the event with sustained periods at 0 m s^{-1}. Peak streamflow was 2.6 and 3.4 mm h^{-1} at WS8 and Lookout Creek (Figure 3.11, Table 3.5).

The 2005-03-03 storm received the highest total precipitation (213.8 mm) in this category, and total net snowmelt was -36.7 mm. Dewpoint temperature typically fluctuated above and below 0.5°C throughout the event with two sustained periods > 0.5°C, and precipitation was mostly rain (82%). Wind speed fluctuated between 0 and

0.6 m s^{-1} throughout the event with sustained periods at 0 m s^{-1}. Peak streamflow was 1.0 and 1.2 mm h^{-1} at WS8 and Lookout Creek (Figure 3.11, Table 3.5).

The 2007-11-13 storm received the median total precipitation (197.9 mm) in this category, and total net snowmelt was -28.0 mm. Dewpoint temperature was typically > 0.5°C days 1 through 6 before dropping on day 7, and precipitation was mostly rain (89%). Wind speed fluctuated between 0 and 0.6 m s^{-1} throughout the event with sustained periods at 0 m s^{-1}. Peak streamflow was 1.6 and 1.3 mm h^{-1} at WS8 and Lookout Creek (Figure 3.11, Table 3.5).

Table 3.5. Selected climatic and hydrologic data for storms in the late accumulation category.

Start date	Total ppt. (mm)	Total net melt (mm)	Total WAR (mm)	Mean dew. temp. (°C)	Mean wind speed (m s^{-1})	WS8 peak flow (mm h^{-1})	Lookout Creek peak flow (mm h^{-1})
2003-12-08	193.0	-8.9	184.1	0.5	0.1	2.6	3.4
2005-03-23	213.8	-36.7	177.1	1.3	0.1	1.0	1.2
2007-11-13	197.9	-28.0	169.8	2.9	0.1	1.6	1.3

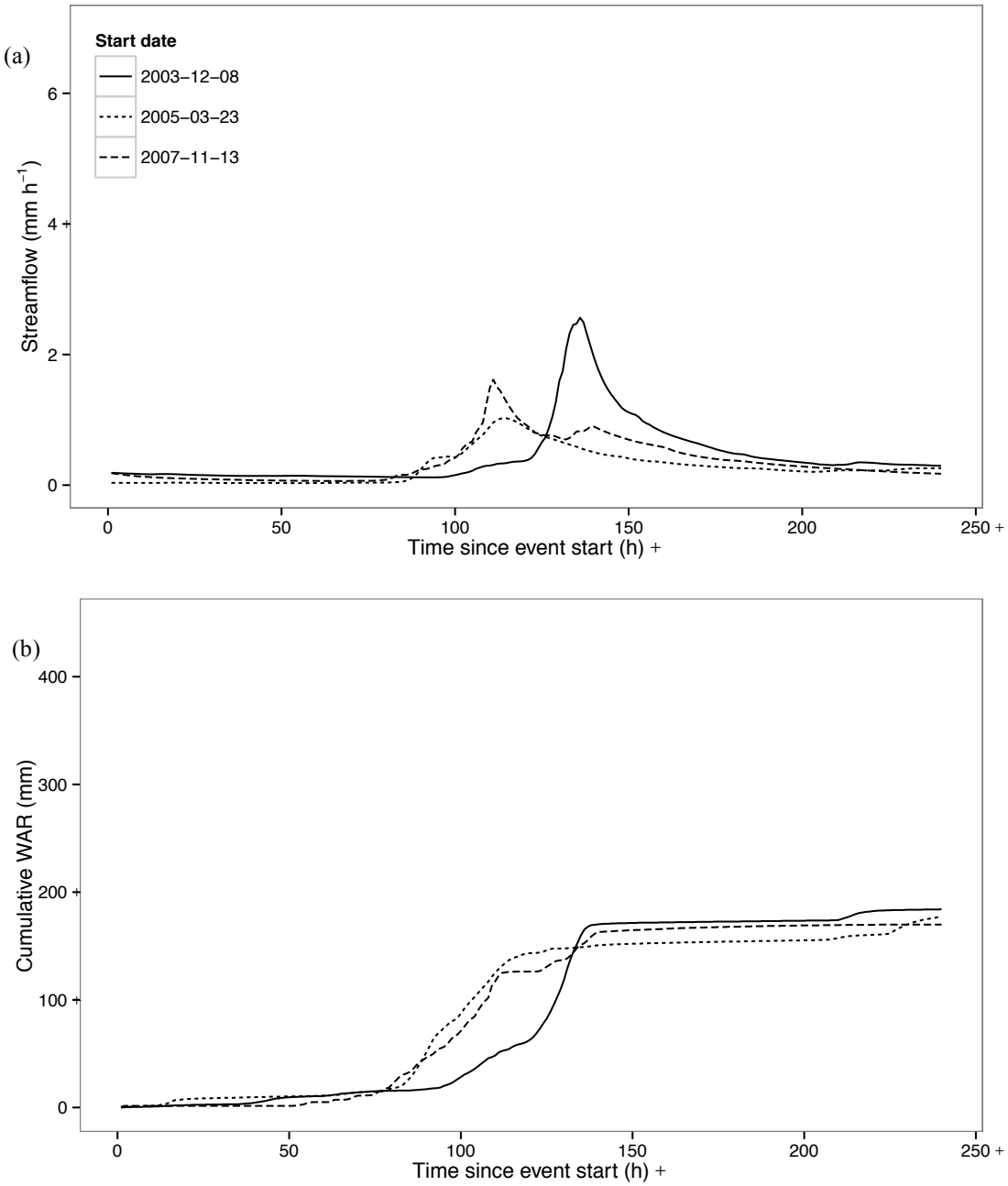

Figure 3.11. WS8 streamflow (a) and cumulative WAR (b) plotted against time for each event in the late accumulation response category. The steepness of the cumulative WAR line represents combined snowmelt and precipitation intensity.

3.1.6. Category comparisons

Total water available for runoff (WAR) is highest for the persistent melt category and lowest for the late accumulation category (Figures 3.2 and 3.13b) and differs significantly among categories (ANOVA F = 2.84, $p < 0.01$), but the only significant pairwise differences are between the persistent net melt (+) category vs. the persistent accumulation (-) category (difference 141 mm, $p < 0.01$) and (+) vs. the late accumulation (+/-) category (difference = 162 mm, $p < 0.02$). The ratio of total WAR to total precipitation is highest for the persistent melt category (+) and lowest for the persistent accumulation (-) category (Figure 3.13a) and differs significantly among categories (ANOVA F = 20.56, $p < 0.0001$). This ratio is significantly higher for the (+) category than for the (=), (-), (-/+), or (+/-) category (differences = 0.4, 0.8, 0.3, 0.5; $p < 0.02$); the ratio is also significantly lower for the (-) category compared to the flat (=) and late melt (-/+) categories (differences = 0.4, 0.5, $p < 0.003$).

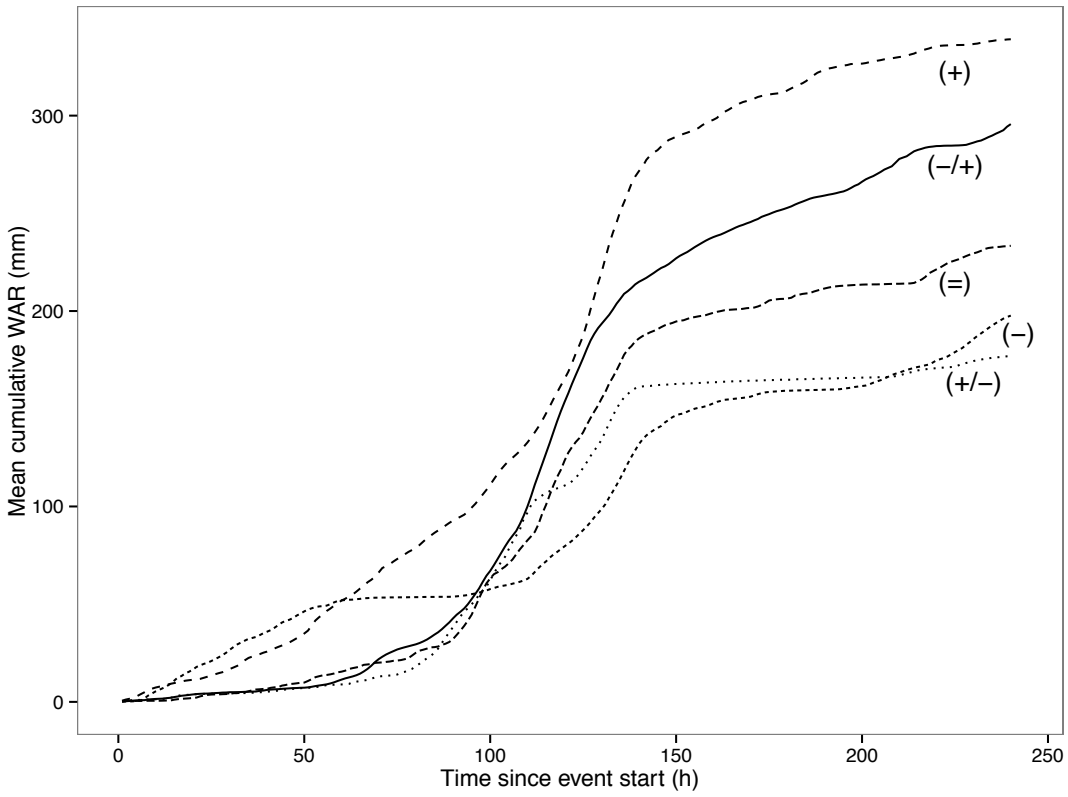

Figure 3.12. The mean cumulative water available for runoff (WAR, precipitation plus net snowmelt) curves plotted against time for each response category.

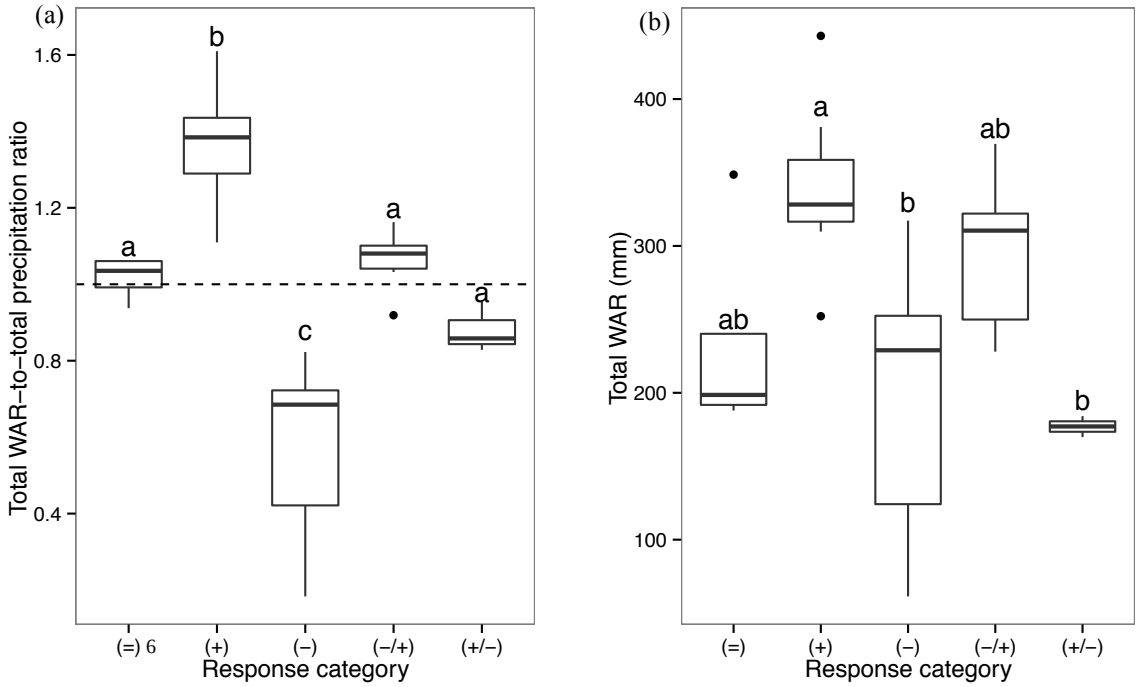

Figure 3.13. WAR-to-precipitation ratio (a) and total WAR (b) boxplots for each response category. Values above the dashed line in (a) correspond to storms where total WAR was augmented by positive total net snowmelt, while values below the line correspond to storms where negative total net snowmelt reduced total WAR relative to total precipitation. The letter above each box represents that response category's grouping according to the Tukey-Kramer test. The means of response categories displaying the same group letter are not statistically different from one another at the $p < 0.05$ level.

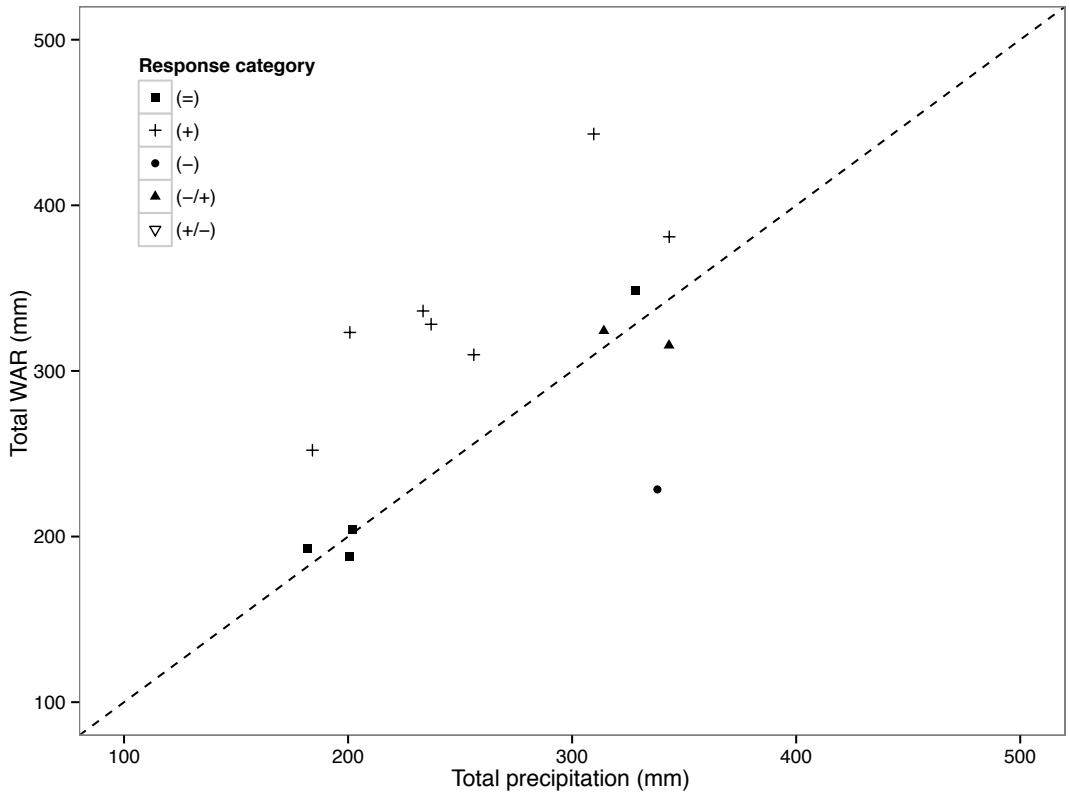

Figure 3.14. Total WAR plotted against total precipitation for all storms. The dashed line represents a 1:1 relationship between the two variables. The farther a point lies above (below) the line, the greater the degree of WAR augmentation (reduction) by net snowmelt.

Total net snowmelt (Figure 3.15a) is highest for the persistent melt category (+) and lowest for the persistent accumulation (-) category, and differs significantly among categories (ANOVA F = 22; $p < 0.0001$). Snowmelt is significantly higher for the (+) category than for the (=), (-), (-/+), and (+/-) categories (differences = 81.8 mm, 224.3 mm, 72.4 mm, 111.5 mm; $p < 0.05$) and it is significantly lower for the (-) category than the (=), (+), (-/+), and (+/-) categories (differences = -142.5 mm, -224.3 mm, -151.9 mm, -112.7 mm; $p < 0.002$).

Rain fraction (Figure 3.15b) is highest for the (=) category and lowest for the (-) category, and differs significantly among categories (ANOVA F = 8.6; $p < 0.0003$). The only significant pairwise differences are between the (-) category and the (=), (+), and (-/+) categories (differences = 0.25, 0.23, 0.16; $p < 0.002$).

Mean dewpoint and air temperature (Figure 3.16) are highest for the (=) and (+) categories, but there are no significant differences among groups (ANOVA F =

2.4 and 2.0; $p < 0.09$ and 0.2). There are also no significant differences among groups in wind speed (ANOVA F = 1.6, $p < 0.3$).

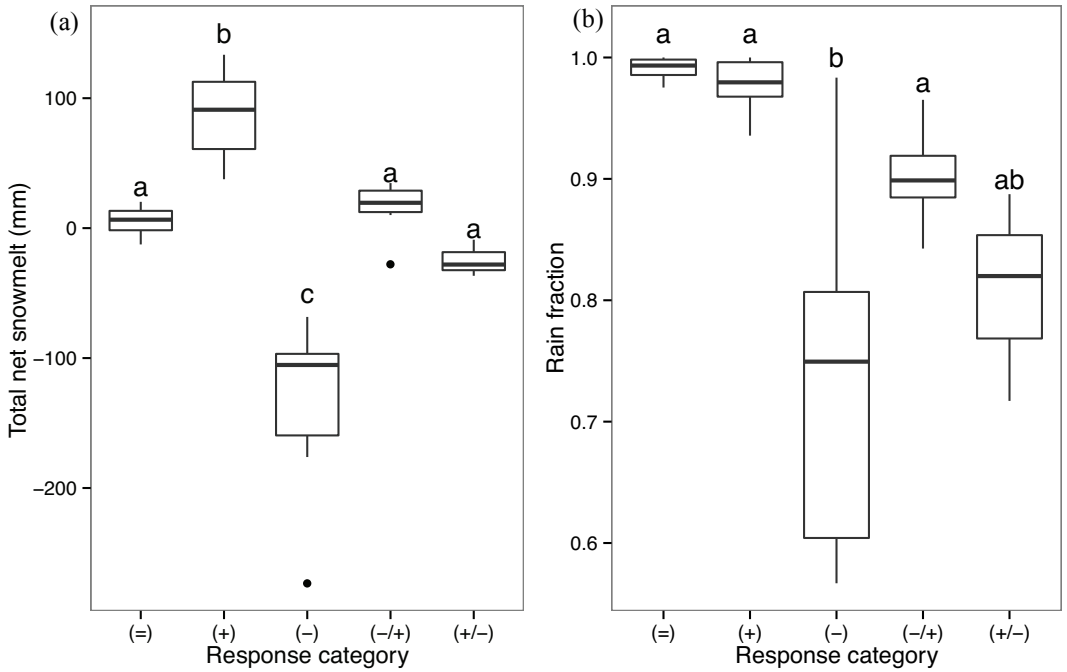

Figure 3.15. Total net snowmelt (a) and rain fraction (b) values per response category. The letter above each box represents that response category's grouping according to the Tukey-Kramer test. The means of response categories displaying the same group letter are not statistically different from one another at the $p < 0.05$ level.

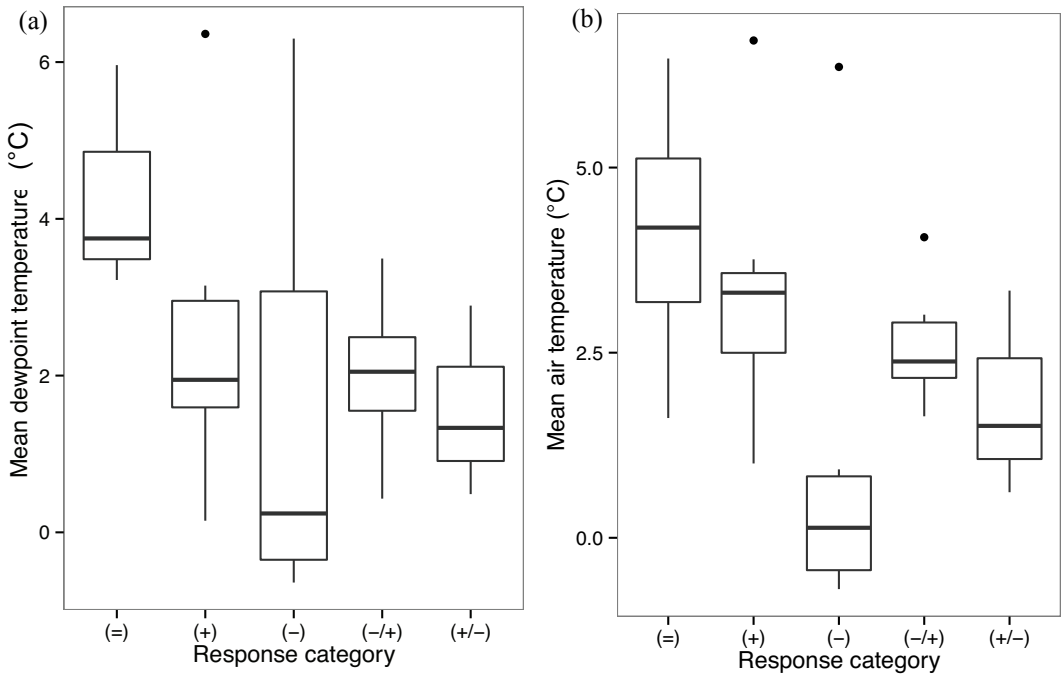

Figure 3.16. Mean dewpoint (a) and air temperature (b) values per response category. There are no significant differences at the $p < 0.05$ level between response categories according to the Tukey-Kramer test.

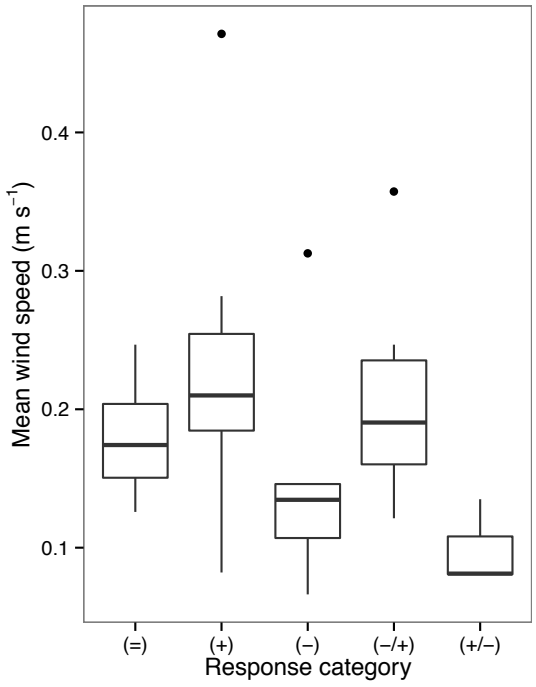

Figure 3.17. Mean wind speed values per response category. There are no significant differences at the $p < 0.05$ level between response categories according to the Tukey-Kramer test.

WS8 and Lookout Creek peak flow are highest for (+) events, but there are no significant differences among groups (ANOVA F = 1.9 and 1.6; $p < 0.2$). The (+) category contains the 1st, 3rd, 4th, and 5th ranked WS8 peak flow values and the 1st, 2nd, and 5th ranked Lookout Creek peak flow values. The (-/+) category includes the rest of the top-five ranked peak flows at WS8 and Lookout Creek.

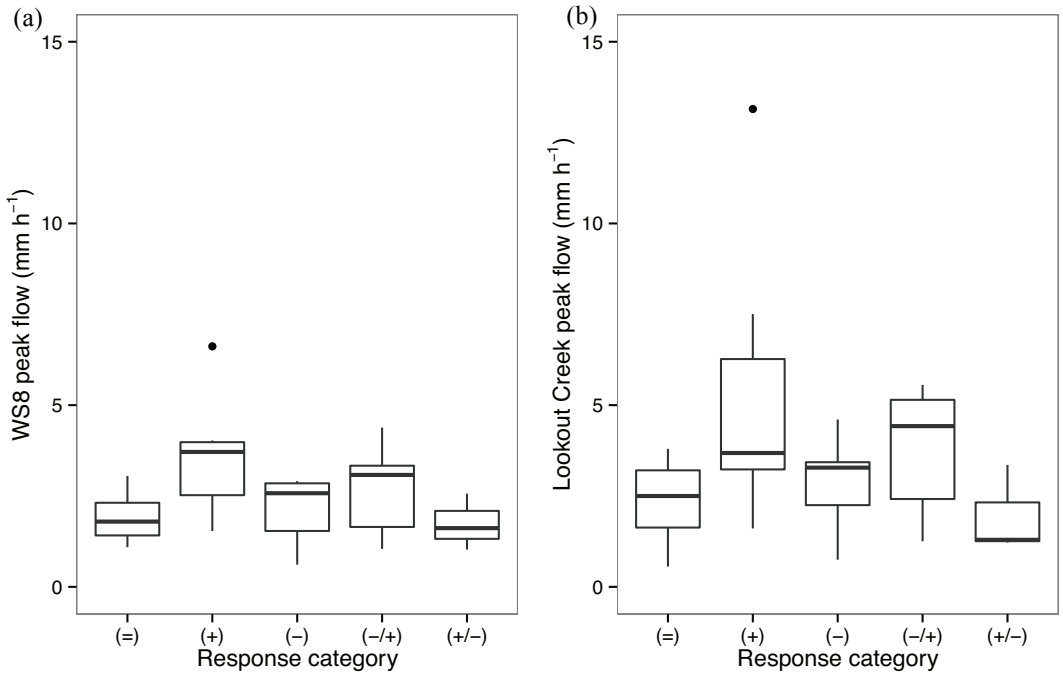

Figure 3.18. WS8 (a) and Lookout Creek peak flow values (b) per response category. There are no significant differences at the $p < 0.05$ level between response categories according to the Tukey-Kramer test.

All but one of the persistent melt (+) events fall above the dashed lines in Figure 3.19 and the category is ranked highest in flow augmentation (Table 3.6), which is defined as the mean of the category's residuals from the linear regression in Figure 3.19. Late melt (-/+) storms are ranked 2nd in mean flow augmentation and two-thirds of these storms lie above the augmentation line for WS8 (they are split evenly above and below the augmentation line for Lookout Creek). The flat (=) and late accumuluation (+/-) categories each contribute one event above the dashed lines, but both have negative mean augmentation values, meaning peak flow was lower than what would be expected based on precipitation alone. All persistent accumulation (-)

events lie below the dashed line and the category is ranked lowest in mean flow augmentation.

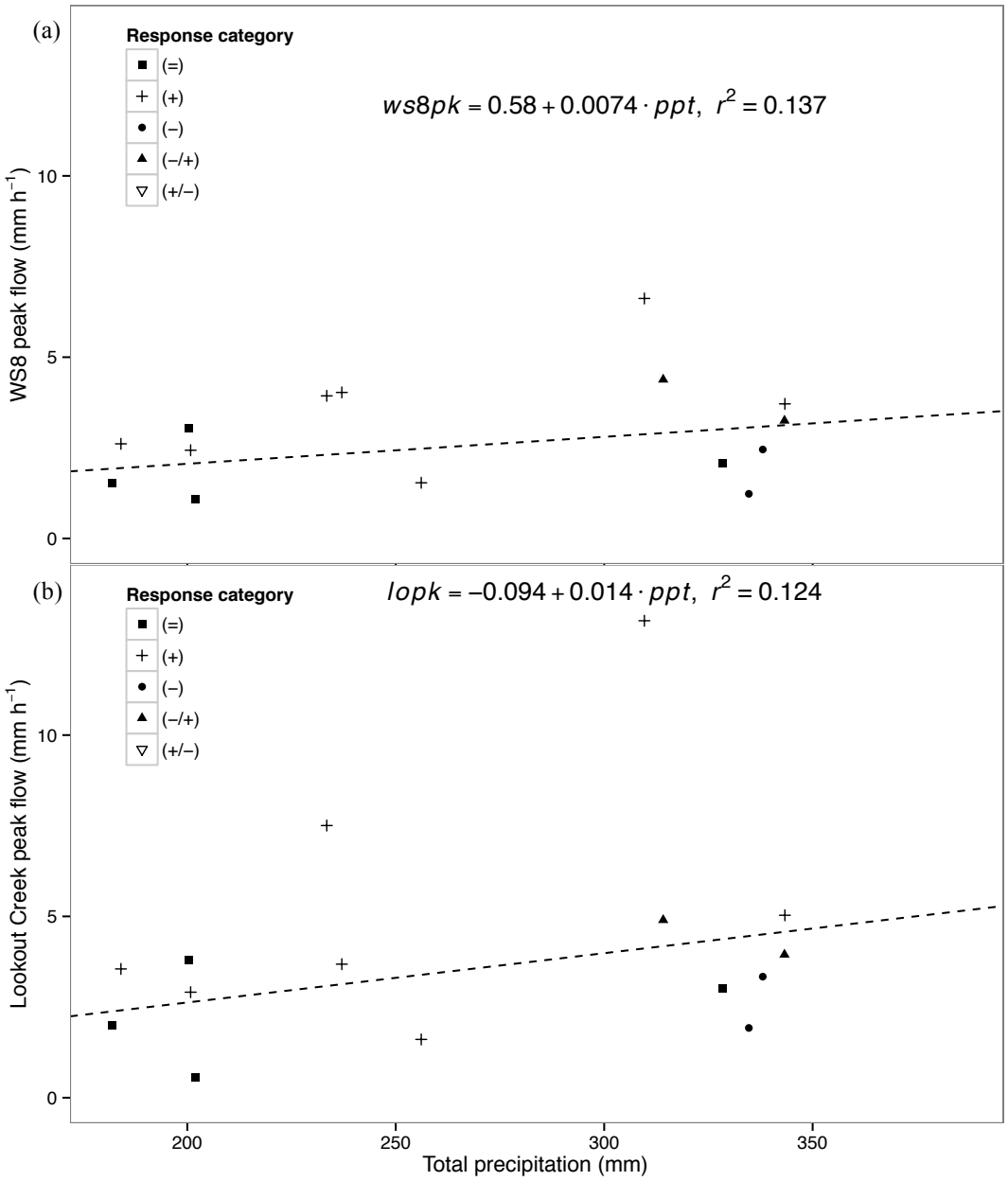

Figure 3.19. WS8 (a) and Lookout Creek (b) peak flow plotted against H15MET total precipitation per storm. The dashed line represents the linear regression of peak flow as predicted by total precipitation. In this case, the line is used to represent a border above which peak flow values are higher and below which values are lower than what might be expected based on total precipitation alone.

Table 3.6. Mean peak flow and peak flow augmentation values for WS8 and Lookout Creek per response category. Mean augmentation is defined as the average of the residuals of each category from the linear regressions in Figure 3.19a and b.

Response category	Mean WS8 peak flow (mm h^{-1})	Mean WS8 peak flow augmentation (mm h^{-1})	Mean Lookout Creek peak flow (mm h^{-1})	Mean Lookout Creek peak flow augmentation (mm h^{-1})
Flat	2.0	-0.3	2.3	-0.7
Persistent melt	3.6	1.1	5.3	2.0
Persistent accumulation	2.1	-0.9	2.9	-1.6
Late melt	2.7	0.0	3.8	0.1
Late accumulation	1.7	-0.3	2.0	-0.7

For the 26 storm events total water available for runoff explains 64% and 68% of the variation in WS8 and Lookout Creek peak flow (Figures 3.20 and 3.21) while WS8 peak flow explains 89% of the variation in Lookout Creek peak flow (Figure 3.22).

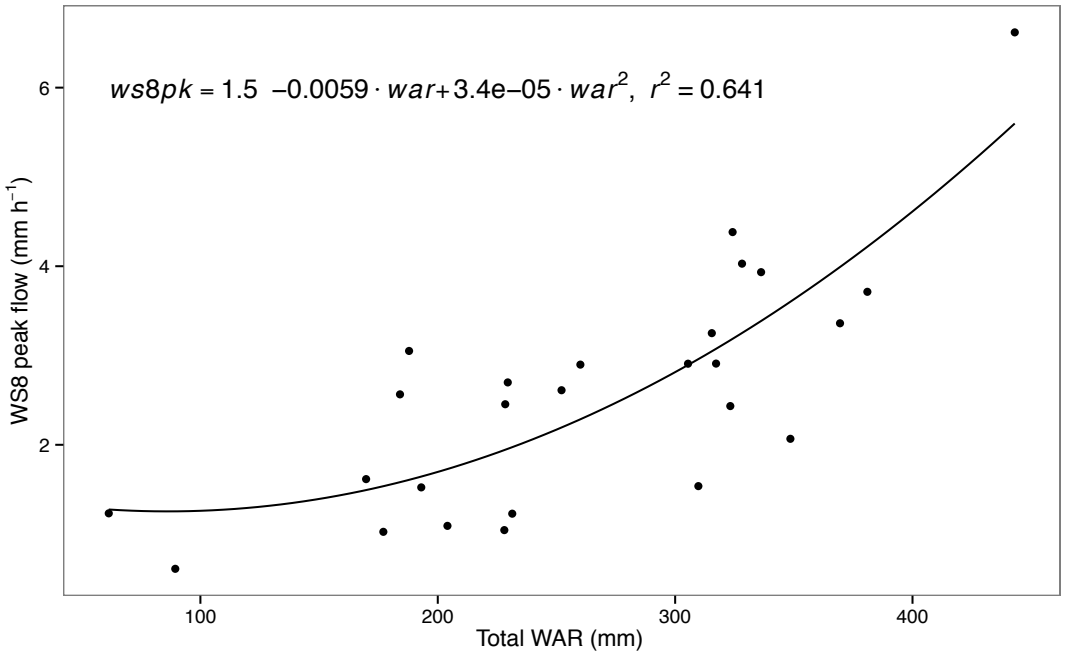

Figure 3.20. WS8 peak flow plotted against total water available for runoff (WAR). The black line represents the quadratic regression of WS8 peak flow (*ws8pk*) as predicted by WAR (*war*).

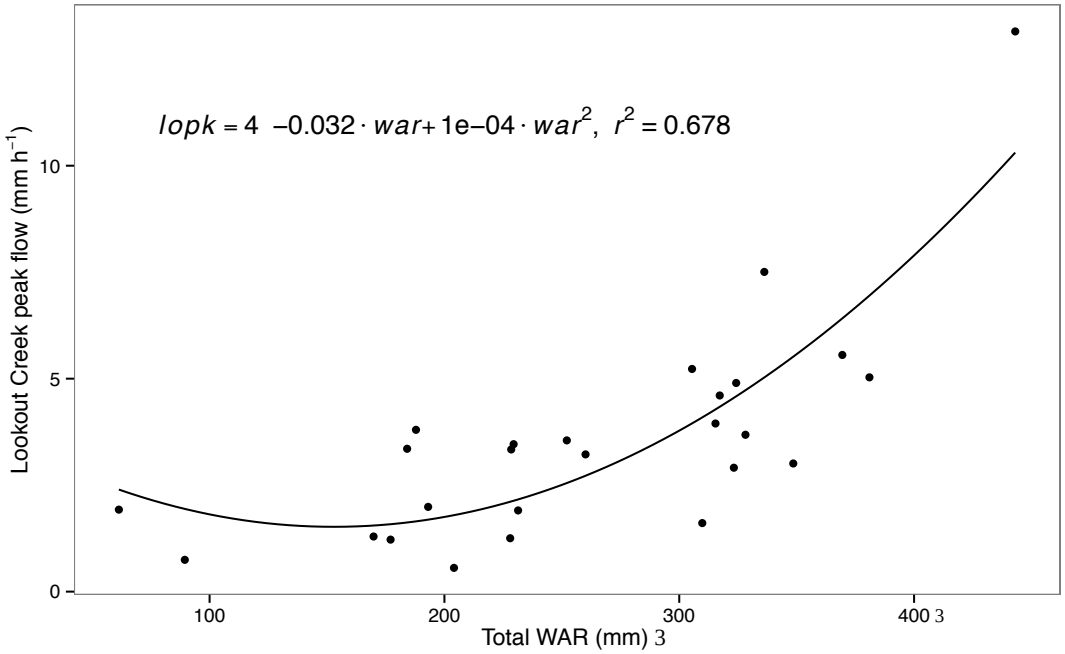

Figure 3.21. Lookout Creek peak flow plotted against total water available for runoff (WAR). The black line represents the quadratic regression of Lookout Creek peak flow (*lopk*) as predicted by WAR (*war*).

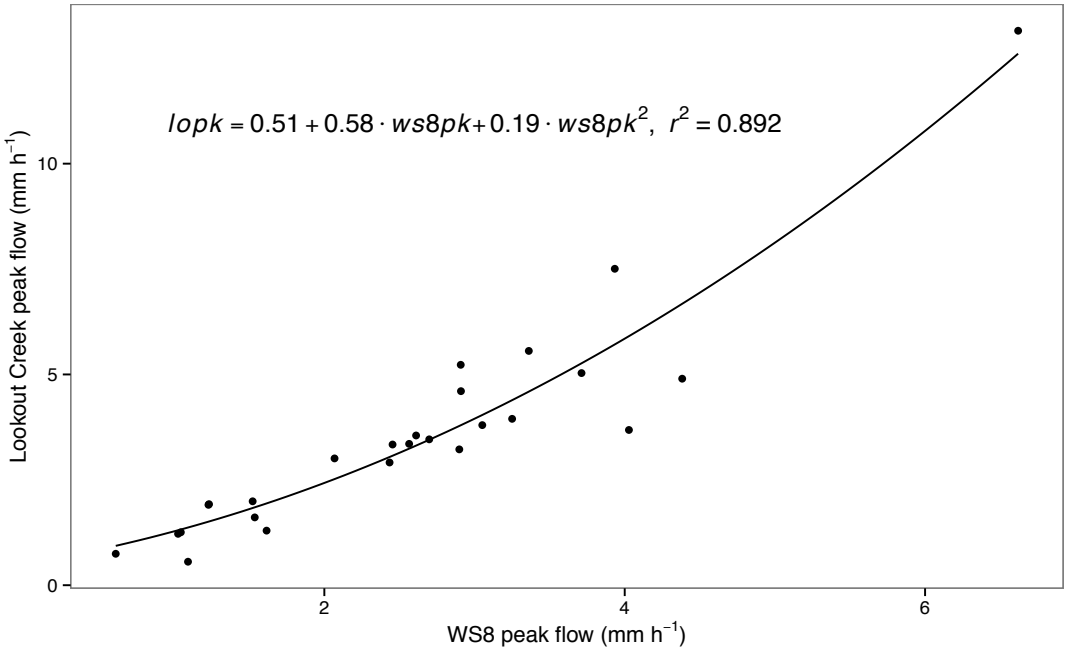

Figure 3.22. Lookout Creek peak flow plotted against WS8 peak flow. The black line represents the quadratic regression of Lookout Creek peak flow (*lopk*) as predicted by WS8 peak flow (*ws8pk*).

3.1.7. SNOTEL snow water equivalent data

At least 20 mm of SWE was recorded at one of the SNOTEL stations (Figures 3.23, 3.24, and 3.25) at the start of each event except for two (1995-11-22 and 2007-10-15). On average, persistent melt events had the greatest SWE at event start (375.1 mm), followed by flat (224.6 mm), late melt (205.5 mm), persistent accumulation (161.0 mm), and late accumulation (119.7). Please see Appendix D for complete SNOTEL and H.J. Andrews SWE data.

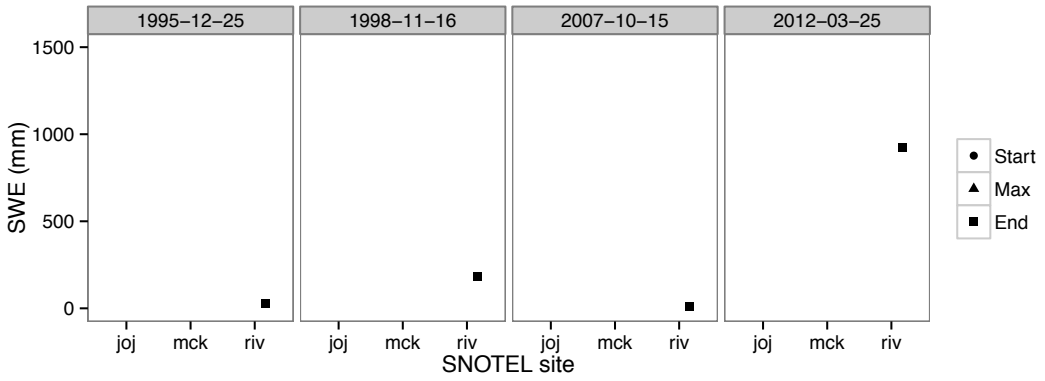

Figure 3.23. Daily SWE data for the three SNOTEL stations (joj = Jump off Joe; mck = McKenzie; riv = Roaring River) closest to the H.J. Andrews for flat storms. Start = SWE at event start; Max = maximum recorded SWE; End = SWE at event end.

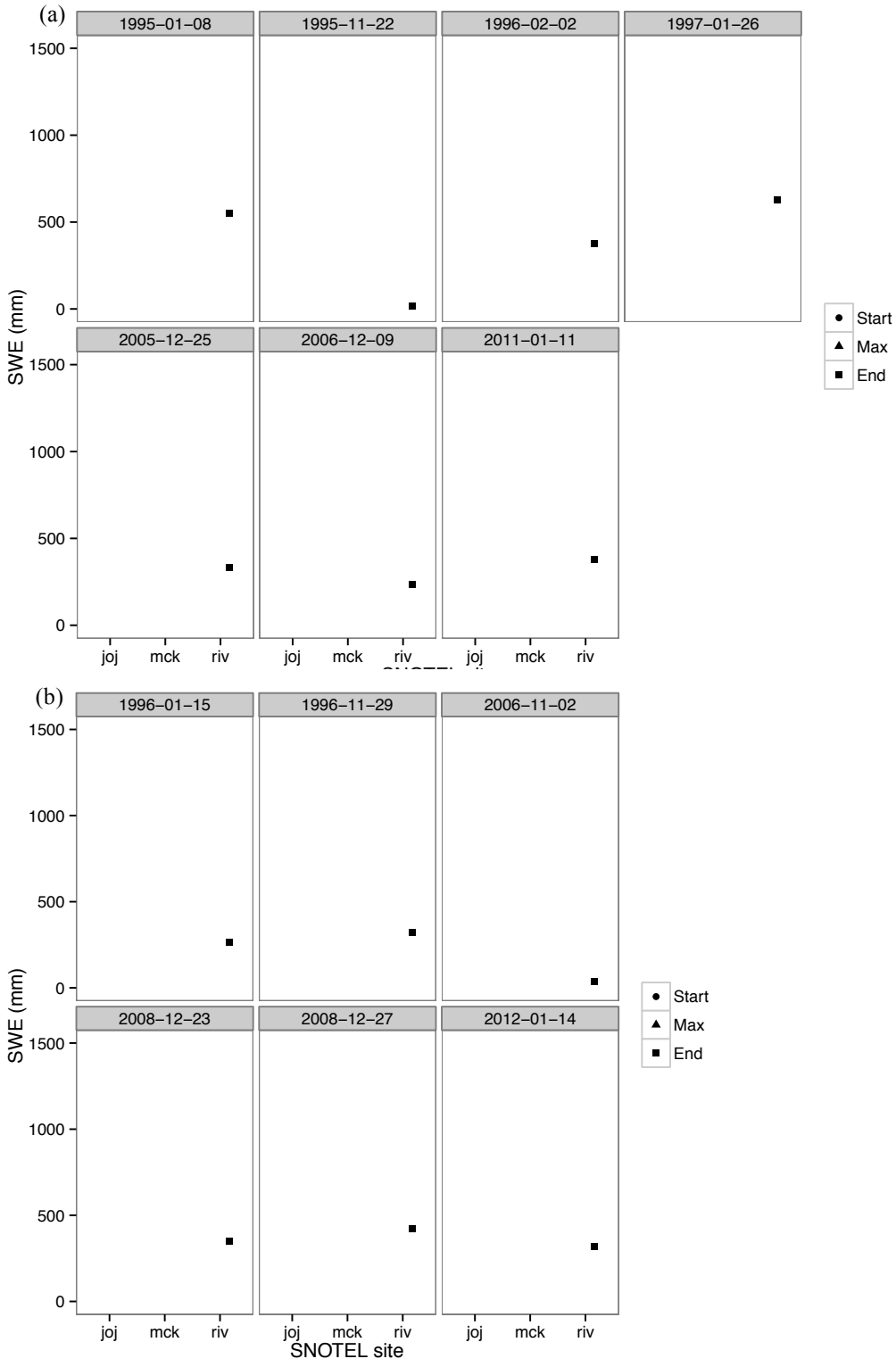

Figure 3.24. Daily SWE data for the three SNOTEL stations (joj = Jump off Joe; mck = McKenzie; riv = Roaring River) closest to the H.J. Andrews for persistent melt (a) and persistent accumulation (b) storms. Start = SWE at event start; Max = maximum recorded SWE; End = SWE at event end.

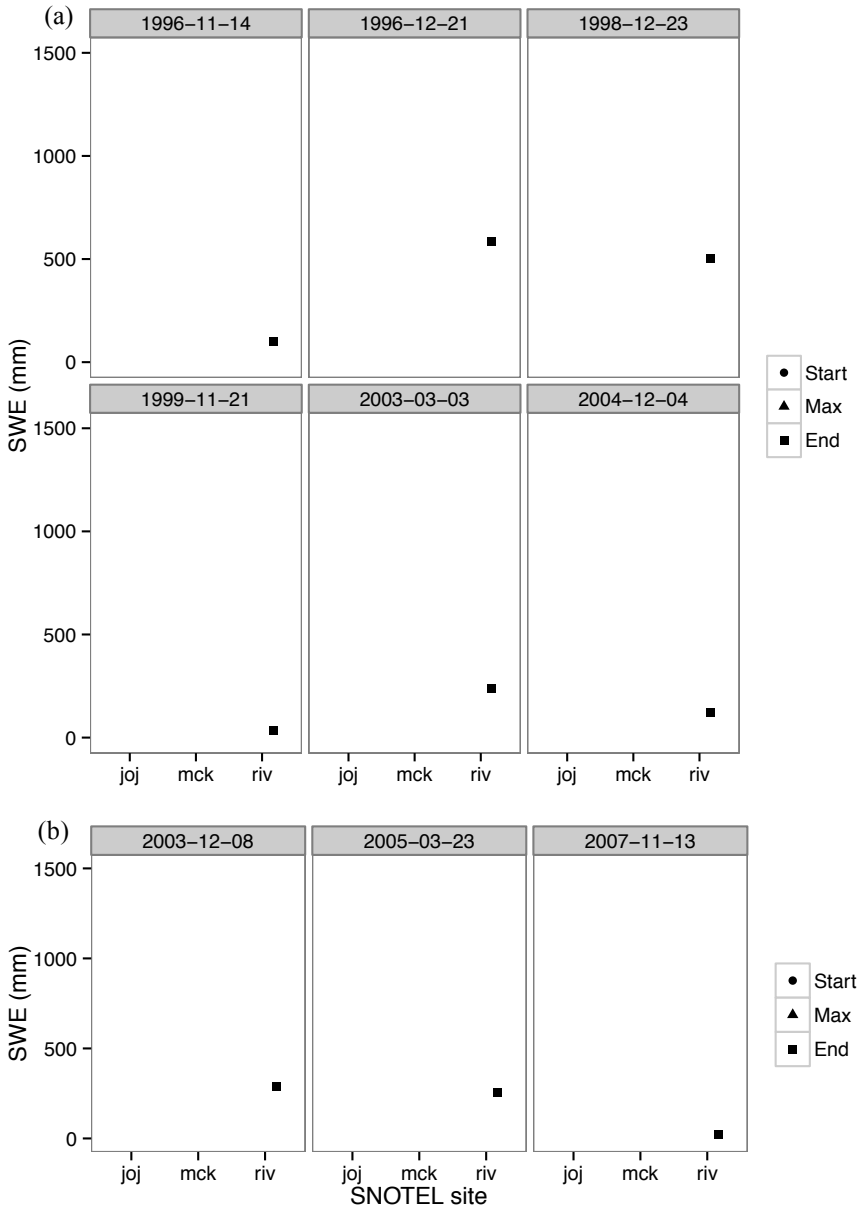

Figure 3.25. Daily SWE data for the three SNOTEL stations (joj = Jump off Joe; mck = McKenzie; riv = Roaring River) closest to the H.J. Andrews for late melt (a) and late accumulation (b) storms. Start = SWE at event start; Max = maximum recorded SWE; End = SWE at event end.

3.1.8. Wind, temperature, and precipitation characteristics of net snowmelt

Hourly net snowmelt rates (mm h^{-1}) were positively related to wind speed, air and dewpoint temperature, and precipitation within and among storms (Figures 3.26, 3.27, and 3.28, Table 3.7). Wind speed, air and dewpoint temperature, and precipitation were lowest during hours with zero net snowmelt and highest during hours with > 2 mm h^{-1} net snowmelt rates. Hourly precipitation increased for categories with > 1 mm h^{-1} net snowmelt rates when hourly precipitation was lagged by 1 hour.

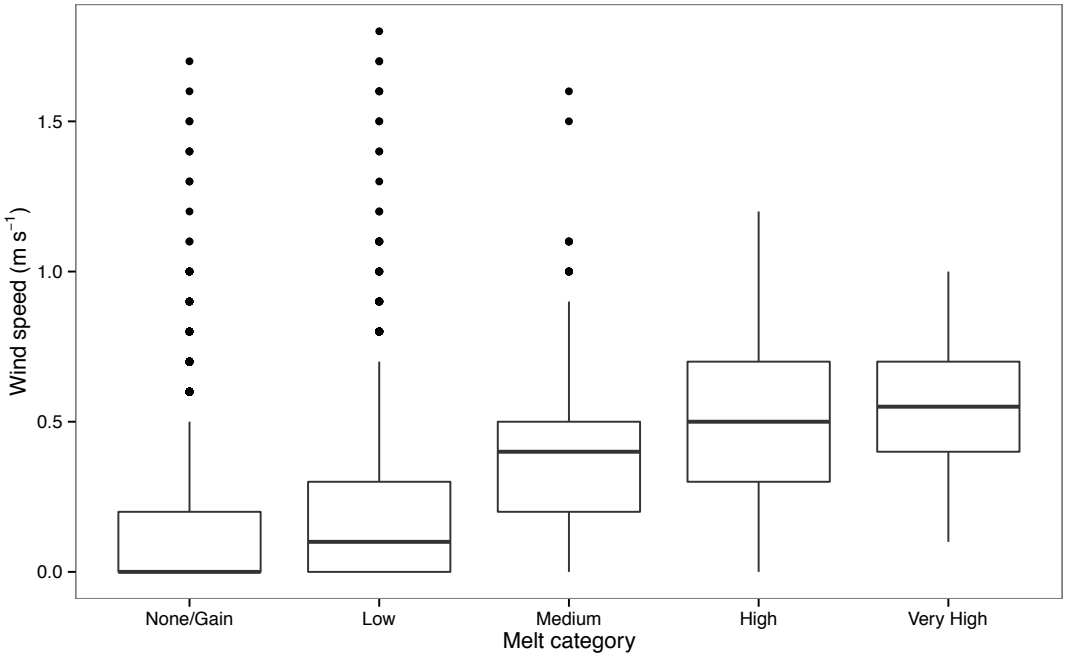

Figure 3.26. Hourly wind speed for the five net snowmelt categories.

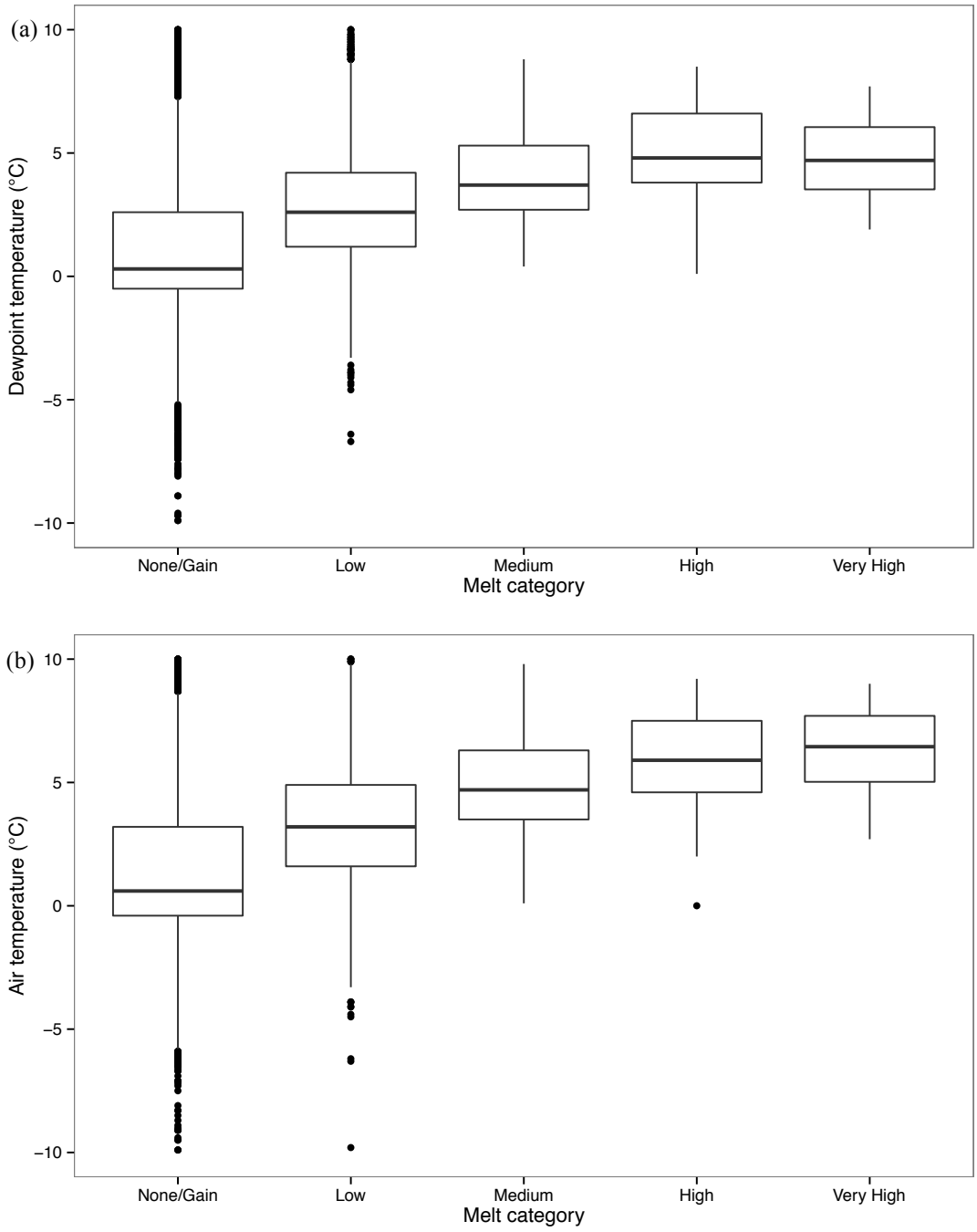

Figure 3.27. Hourly dewpoint (a) and air temperature (b) for the five net snowmelt categories.

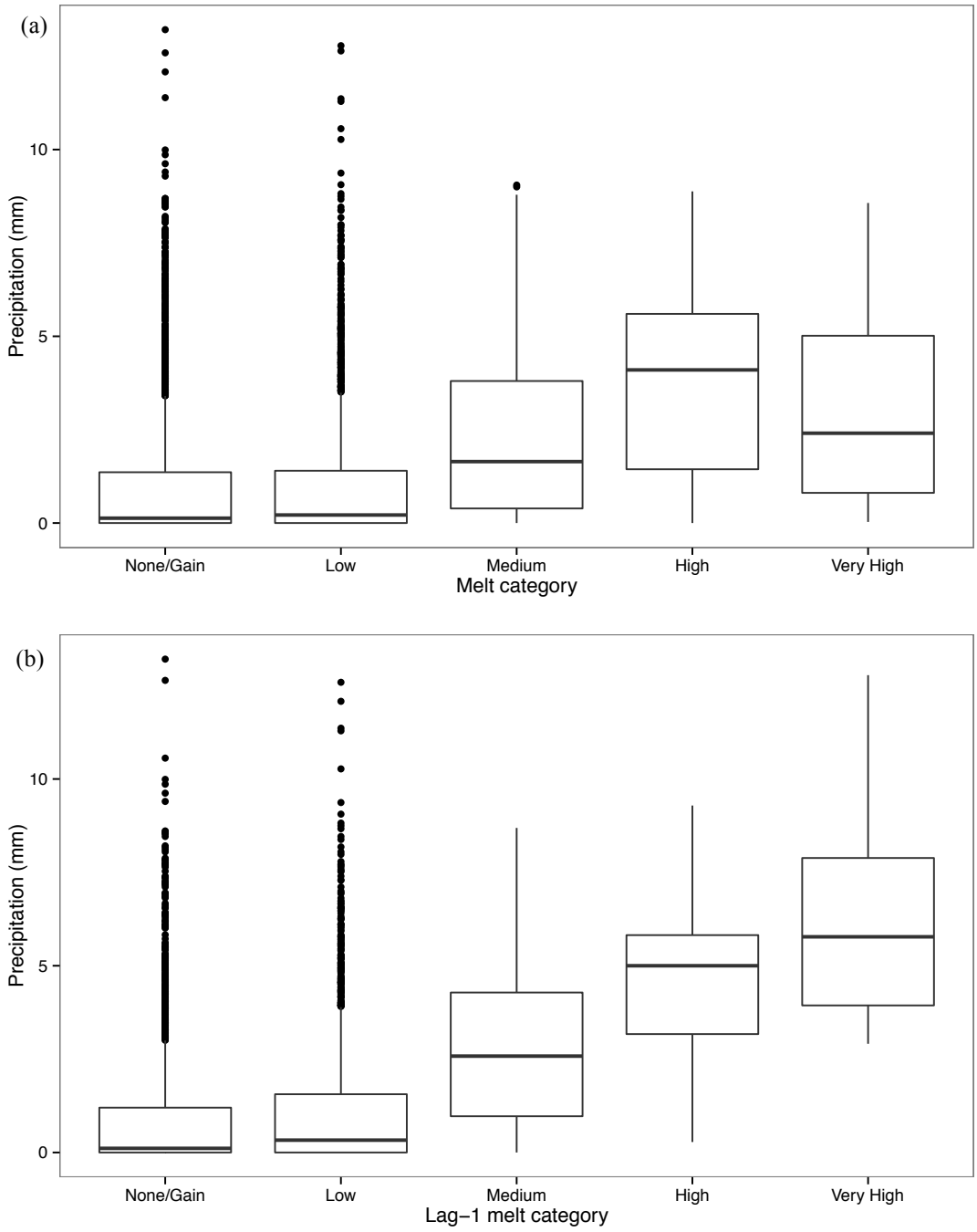

Figure 3.28. Precipitation values for the five net snowmelt (a) and lag-1 net snowmelt (b) categories. The lag-1 categories were assigned by lagging the precipitation values by 1 hour behind net snowmelt.

Table 3.7. Mean wind speed, temperature, and precipitation values for the five net snowmelt categories.

Net snowmelt category	Mean wind speed ($m\ s^{-1}$)	Mean dewpoint temperature (°C)	Mean air temperature (°C)	Mean precipitation ($mm\ h^{-1}$)	Mean ppt. for lag-1 melt category ($mm\ h^{-1}$)
None/Gain	0.1	1.5	1.7	1.0	0.8
Low	0.2	3.1	3.5	1.0	1.1
Medium	0.4	4.0	4.9	2.3	2.8
High	0.5	4.8	6.0	3.7	4.7
Very High	0.5	5.1	6.3	3.2	6.1

3.2. Wavelet coherence and the relative timing of pulses of precipitation and net snowmelt

Wavelet coherence plots were interpreted to examine the relative timing of pulses of precipitation and snowmelt (Figure 3.29). The term *phase difference* in this section refers to the difference in the cycles of the wavelet power of precipitation and net snowmelt (not precipitation phase) (Figure 3.30). Additional wavelet coherence and phase difference distribution plots are presented in Appendix E and F.

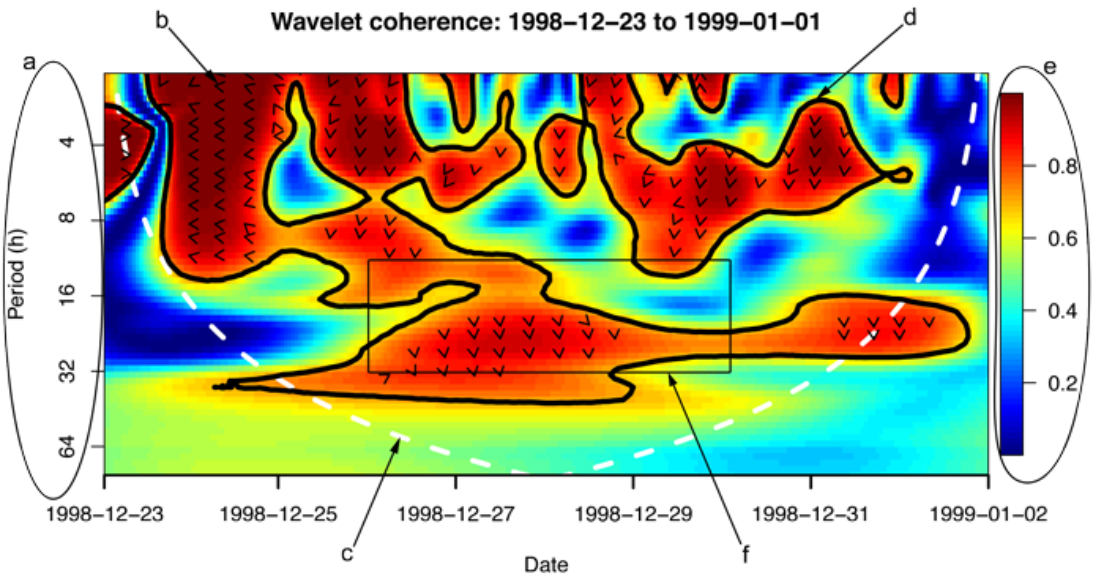

Figure 3.29. How to read a wavelet coherence plot.

The left circle (a) in Figure 3.29 denotes the period of analysis, i.e. the scale of the mother wavelet (the higher the period, the larger the mother wavelet). The mother wavelet picks up small-scale (high-frequency) fluctuations at low periods and large-scale (low-frequency) fluctuations at high periods. Additionally, the range of periods is limited at the lower end by the temporal resolution of precipitation and net snowmelt observations and at the upper end by the largest scale of the mother wavelet that would calculate values inside the cone of influence. The upper left arrow (b) shows a phase difference arrow. When precipitation and snowmelt are in phase (their cycles of wavelet power hit their maxima and minima simultaneously), the arrow points to the right. When the two are in anti-phase (the wavelet power cycle of one variable reaches its minima while the other reaches is maxima), the arrow points to

the left. A downward-pointing arrow denotes the cycle of precipitation wavelet power is leading net snowmelt, and vice-versa for an upward-pointing arrow (for a more detailed explanation on phase differences, please see Figure 3.30). The center arrow (c) marks the cone of influence. Values inside the cone are free from edge effects that result from the increasing scale of the mother wavelet and the resulting dataset-edge overlap. The upper right arrow (d) shows the contour line that marks significant regions of wavelet coherence against a null hypothesis of random red noise. Wide but short areas of significant coherence, as can be seen in the horizontal band from 16 to 32 h, are indicative of a strong relationship between precipitation and net snowmelt across the dataset at that temporal scale. Conversely, narrow but tall areas of significant coherence, as can be seen from 1998-12-24 to 1998-12-26, are indicative of a strong relationship between precipitation and net snowmelt across temporal scales at that time range in the dataset. The right circle (e) encompasses the wavelet coherence color bar. Dark blue denotes low coherence and dark red marks high coherence. Wavelet coherence is squared, so high coherence may be observed whether precipitation and net snowmelt are in or out of phase. Therefore, one must note the direction of the phase difference arrow when interpreting wavelet coherence results. The black box (f) marks the region from which phase difference values were extracted to create the mid-storm, mid-period phase difference distribution.

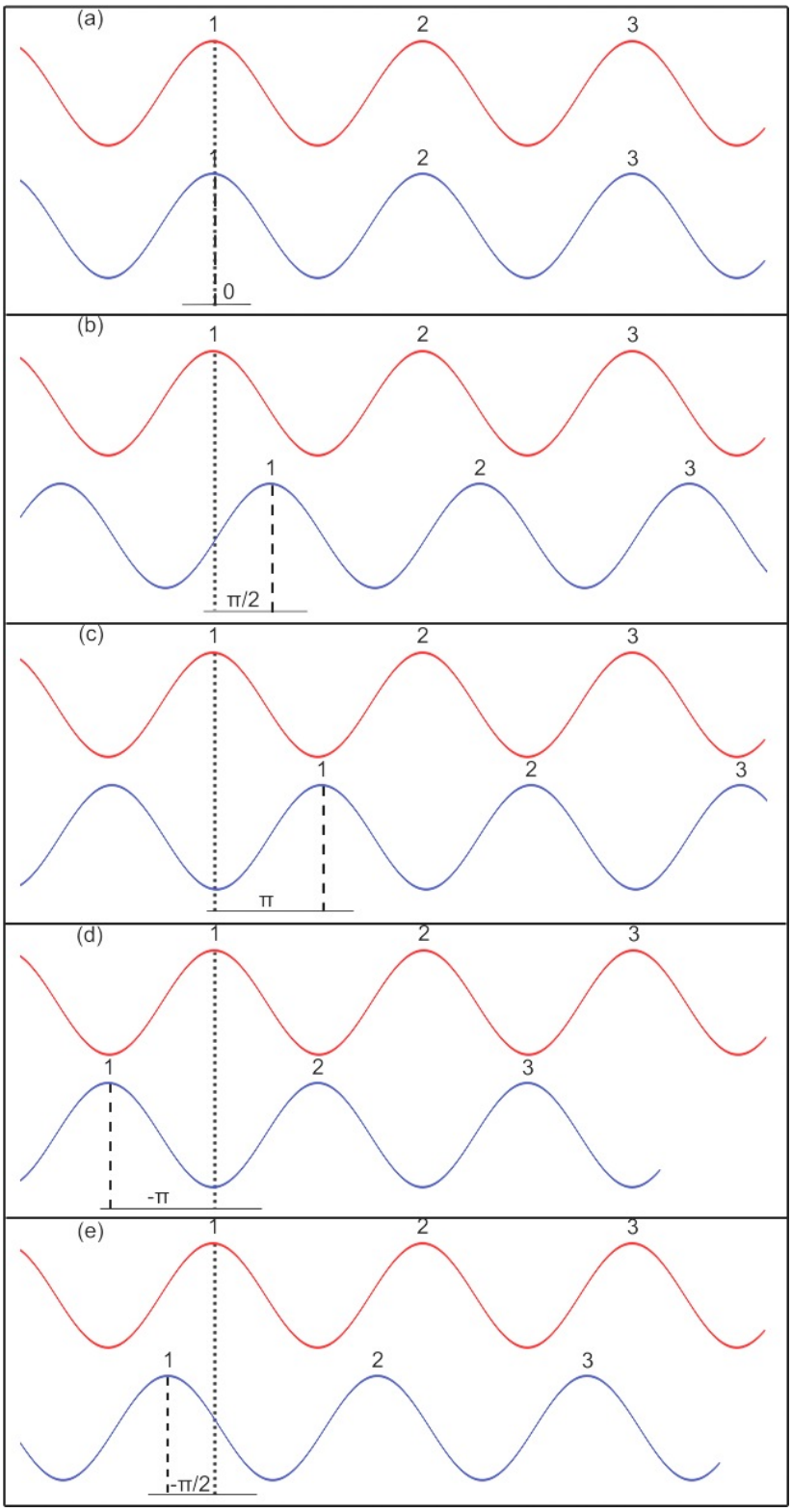

Figure 3.30. How to interpret phase difference values.

For each time step and period, the local—as defined by the scale of the mother wavelet—phase difference is calculated, which is denoted in the wavelet coherence plot by a black arrow (Figure 3.29). In each box in Figure 3.30 above, red represents variable *x* (precipitation) and blue represents *y* (net snowmelt). The numbers correspond to the cycle of wavelet power from which the phase difference is computed (1 is always compared to 1, 2 always to 2, etc.). The dotted line represents the maximum of *x* for cycle 1 and the dashed line represents the maximum of *y* for cycle 1. The number between the two lines is the phase difference. Box (a) shows when the two variables are perfectly in phase (i.e., *x* reaches its maximum concomitantly with *y*). Box (b) shows when the maximum of *x* leads *y* by $\pi/2$. Boxes (c) and (d) show when the two variables are in anti-phase (i.e., *x* reaches its maximum when *y* reaches its minimum, and vice-versa). Box (e) shows when the maximum of *x* trails *y* by $-\pi/2$.

3.2.1. Flat category

The storm of 2007-10-15 is characterized by significant coherence only at smaller temporal scales (< 16 h), and regions of significant coherence are generally small and disconnected (Figure 3.31). At the 12-32-hour time scale, there is no strongly dominant phase difference (Figure 3.32). The other storms in this category display varied patterns in wavelet coherence (Appendix E), while only the 1995-12-25 and 1998-11-16 storms exhibit a dominant mid-storm, mid-period phase difference distribution (Appendix F).

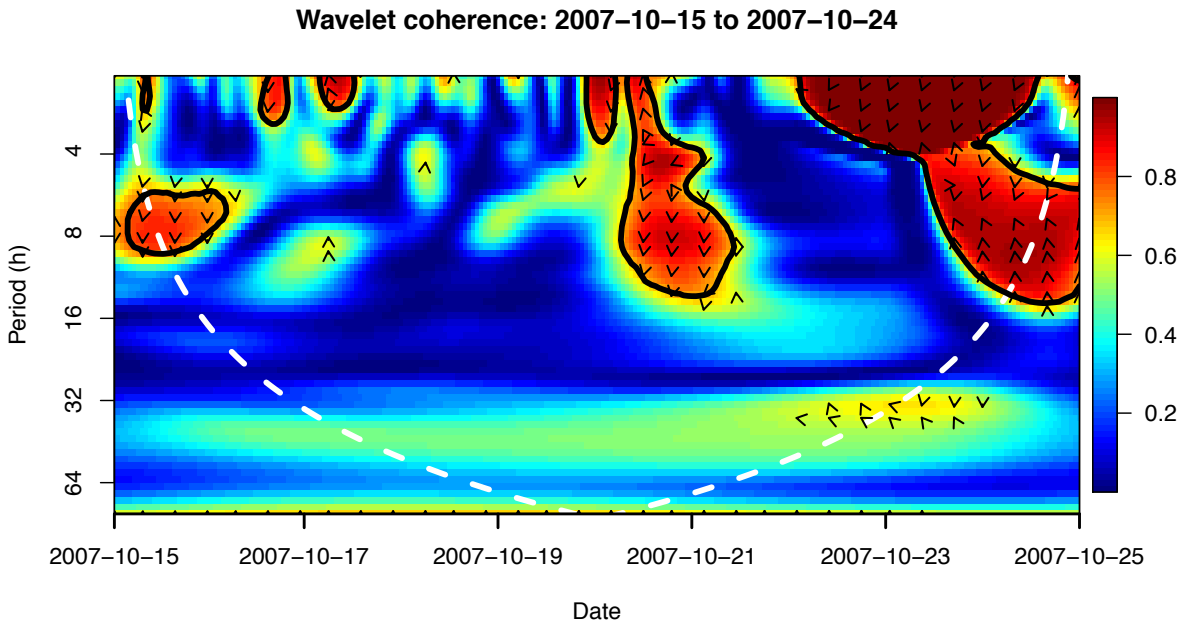

Figure 3.31. Wavelet coherence plot for the 2007-10-15 event.

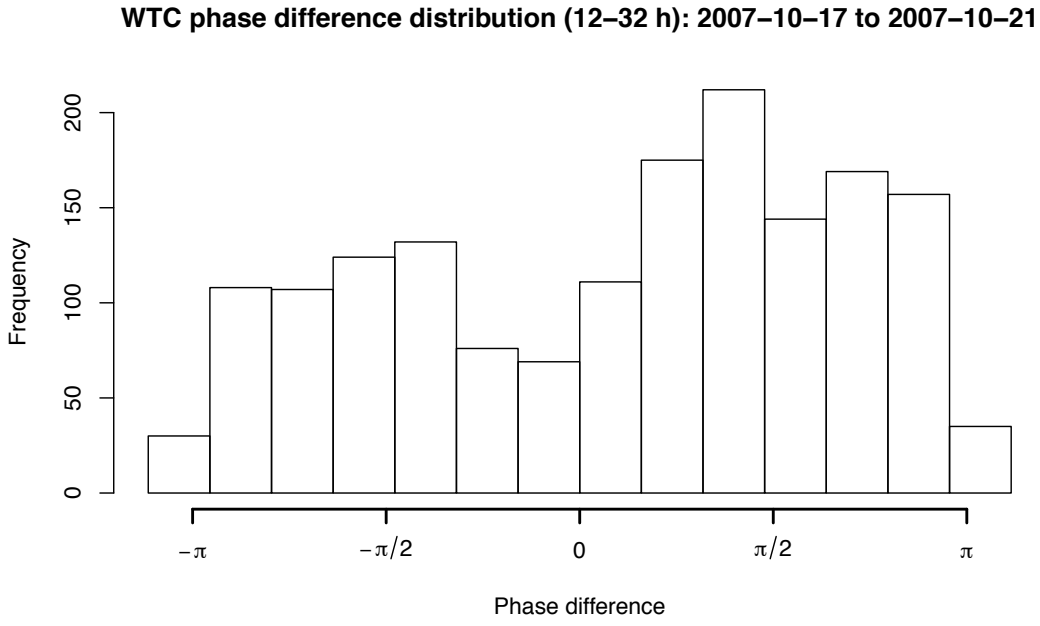

Figure 3.32. Mid-storm, mid-period phase difference histogram for the 2007-10-15 event. Bins display the number of phase difference observations in a given range between $-\pi$ and π for each storm's middle four days at time scales between 12 and 32 h. See Figure 3.30 for an explanation of phase differences.

3.2.2. Persistent melt category

The storm of 1996-02-02 is characterized by a large contiguous region of significant coherence across temporal scales (Figure 3.33). At the 12-32-hour time scale, the phase difference distribution peaks at π/2 (Figure 3.34). The 2011-01-11 storm displays a similar wavelet coherence pattern and mid-storm, mid-period phase difference distribution (Appendix E and F). The other storms in this category express varying patterns of wavelet coherence, and only the 1995-11-22 and 2005-12-25 storms exhibit a mid-storm, mid-period phase difference distribution that does not peak at π/2 (Appendix E and F).

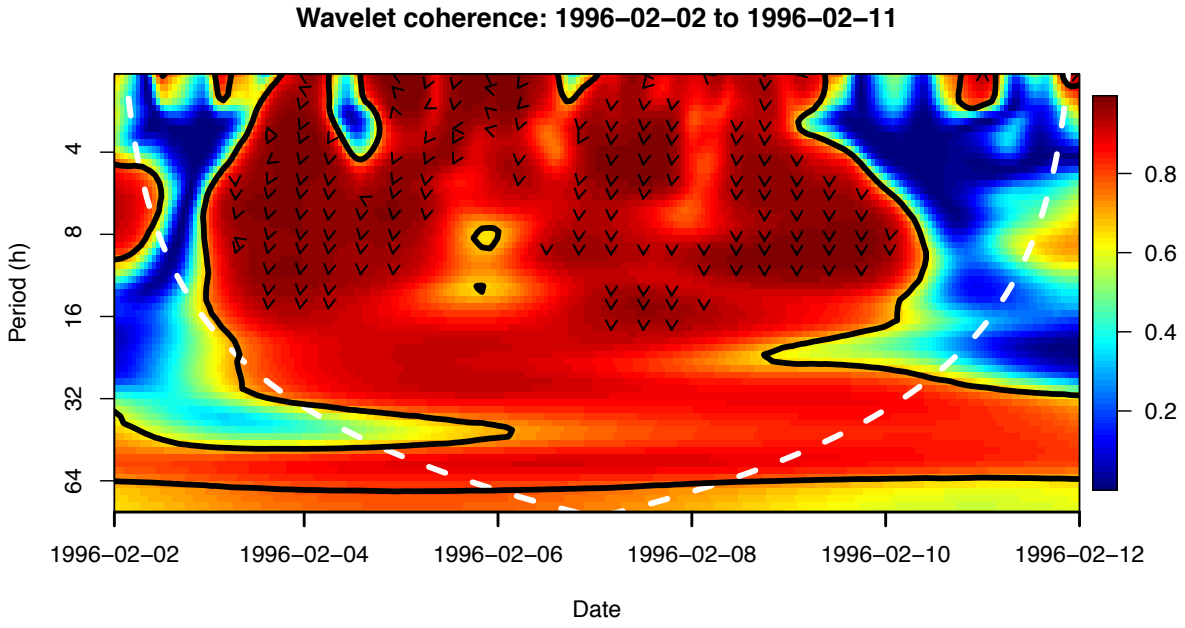

Figure 3.33. Wavelet coherence plot for the 1996-02-02 event.

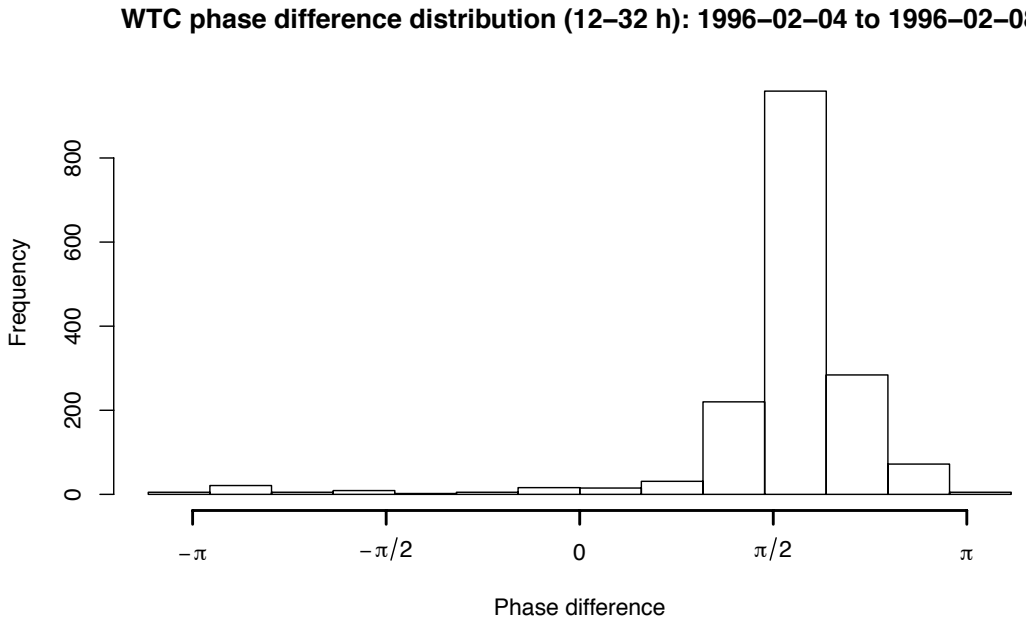

Figure 3.34. Phase difference histogram for the 1996-02-02 event. Bins display the number of phase difference observations in a given range between –π and π for each storm's middle four days at time scales between 12 and 32 h. See Figure 3.30 for an explanation of phase differences.

3.2.3. Persistent accumulation category

The storm of 1996-01-19 is characterized by a large contiguous region of significant coherence at all temporal scales (Figure 3.35). At the 12-32-hour time scale, the phase difference distribution peaks at $-\pi$ and π (Figure 3.36). The 2006-11-02 storm displays a similar wavelet coherence pattern and mid-storm, mid-period phase difference distribution (Appendix E and F). The other storms in this category express similar, but less contiguous, patterns of wavelet coherence at multiple temporal scales (Appendix E), and the associated mid-storm, mid-period phase difference distributions display peaks at π (2008-12-23 and 2012-01-14) and $\pi/2$ (1996-11-29 and 2008-12-27) (Appendix F).

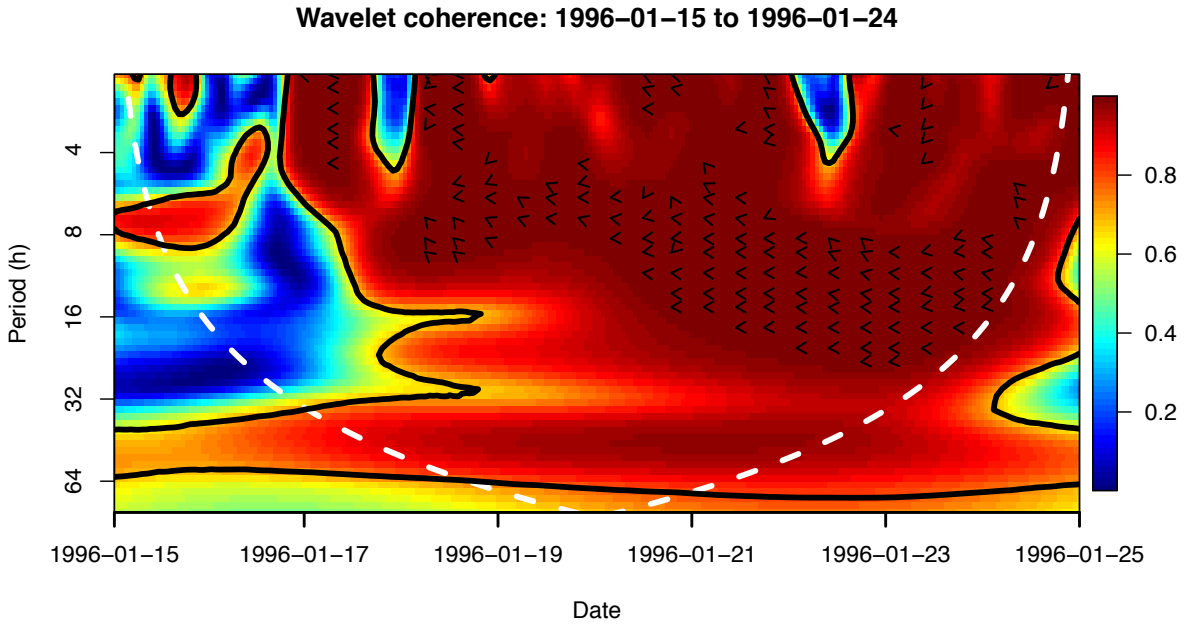

Figure 3.35. Wavelet coherence plot for the 1996-01-15 event.

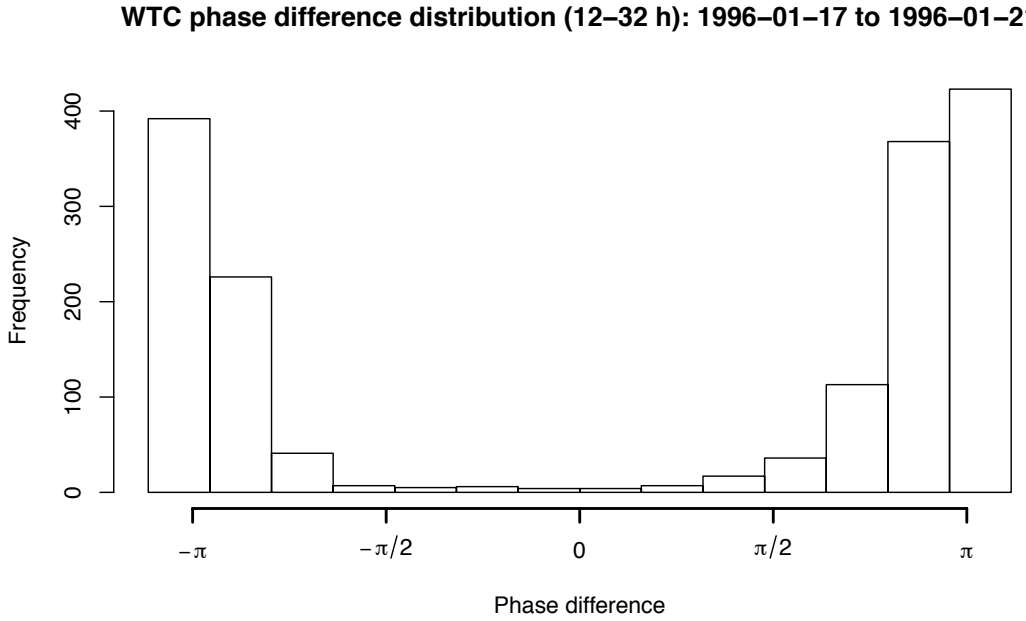

Figure 3.36. Phase difference histogram for the 1996-01-15 event. Bins display the number of phase difference observations in a given range between –π and π for each storm's middle four days at time scales between 12 and 32 h. See Figure 3.30 for an explanation of phase differences.

3.2.4. Late accumulation (late melt) category

The storm of 1996-11-14 is characterized by an early region of significant coherence at smaller temporal scales (< 16 h), and a region of significant coherence at larger time scales (32-64 h) that lasts throughout the event (Figure 3.37). At the 12-32-hour time scale, there is no strongly dominant phase difference (Figure 3.38). The early region of significant coherence is displayed by the other storms in this category and the phase difference arrows typically point left in this region, indicating an anti-phase relationship (Appendix E). Mid-storm, mid-period phase difference distributions are varied for this category with four storms peaking between 0 and π (1996-12-21, 1998-12-23, 1999-11-21 and 2004-12-04) and the other (2003-03-03) displaying no dominant distribution (Appendix F).

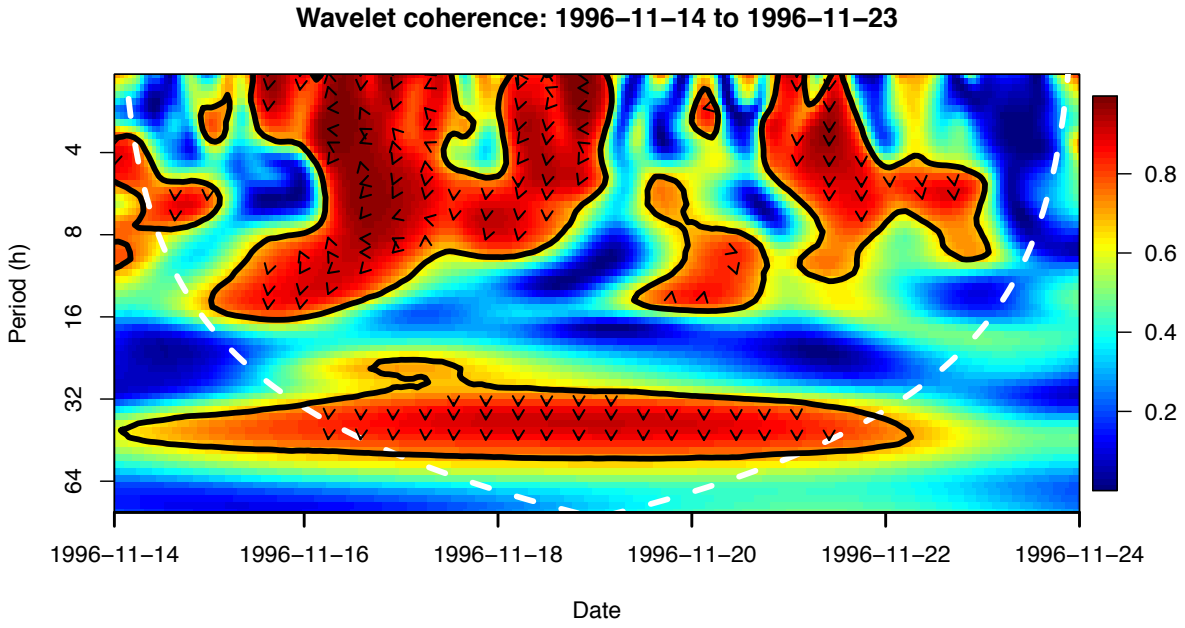

Figure 3.37. Wavelet coherence plot for the 1996-11-14 event.

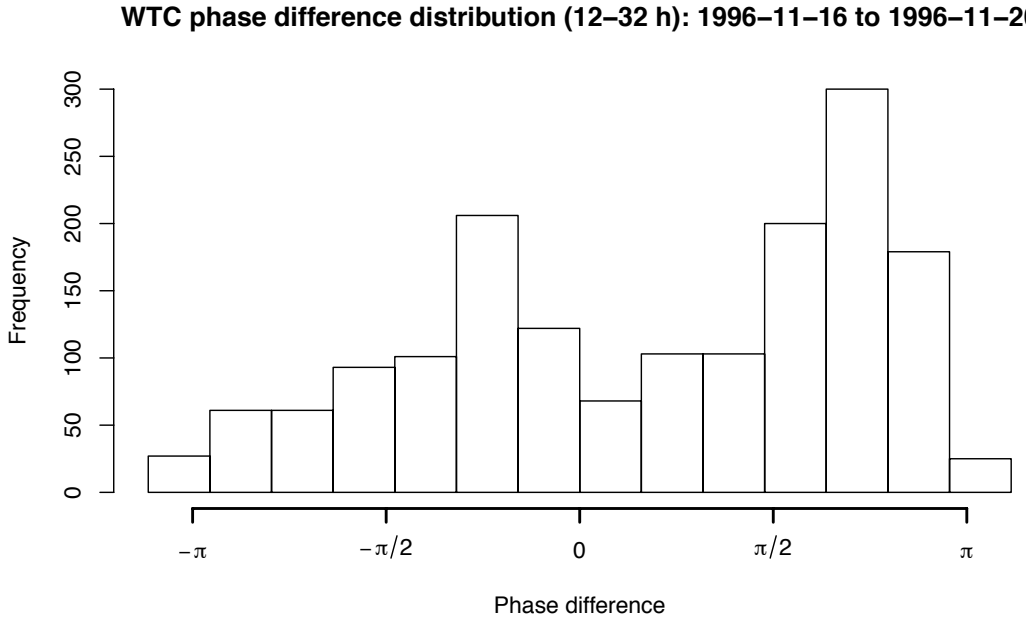

Figure 3.38. Phase difference histogram for the 1996-11-14 event. Bins display the number of phase difference observations in a given range between $-\pi$ and π for each storm's middle four days at time scales between 12 and 32 h. See Figure 3.30 for an explanation of phase differences.

3.2.5. Late melt category

The storm of 2005-03-23 is characterized by early and late periods of significant coherence at temporal scales < 32 h (Figure 3.39). At the 12-32-hour time scale, there is no strongly dominant phase difference (Figure 3.40). The late period of significant coherence is displayed by the other storms in this category and the 2003-12-08 storm also exhibits a band of significant coherence at 16-32 h from the 12th through 16th (Appendix E). The 2007-11-13 storm displays no dominant mid-storm, mid-period phase difference distribution, while the distribution for 2003-12-08 peaks at $\pi/4$ (Appendix F).

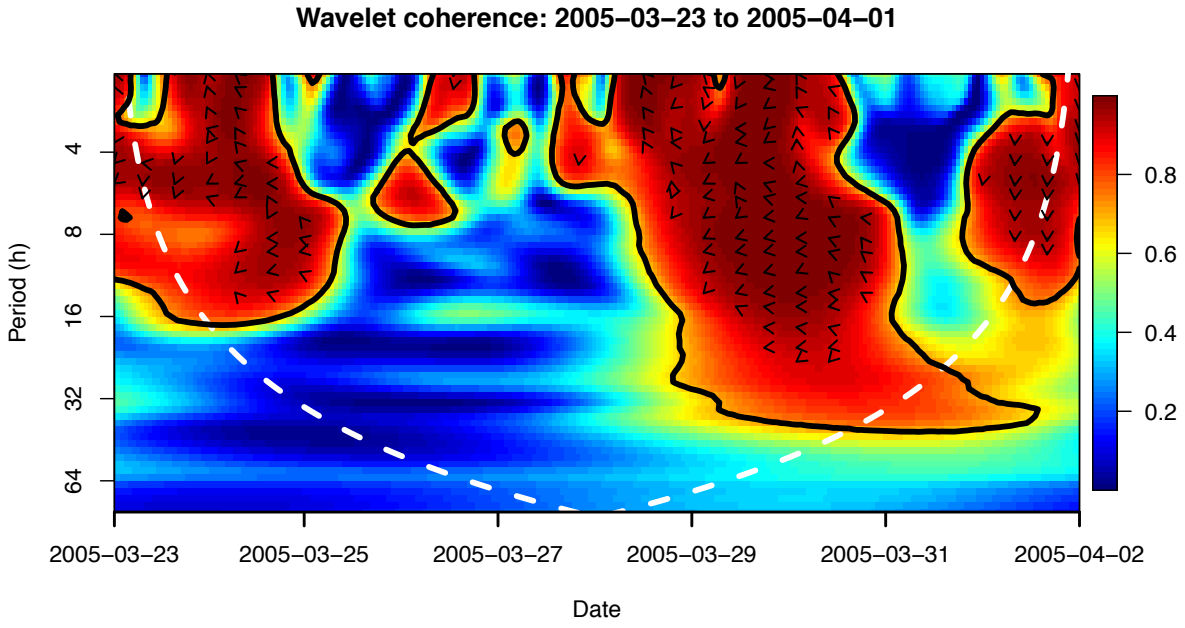

Figure 3.39. Wavelet coherence plot for the 2005-03-23 event.

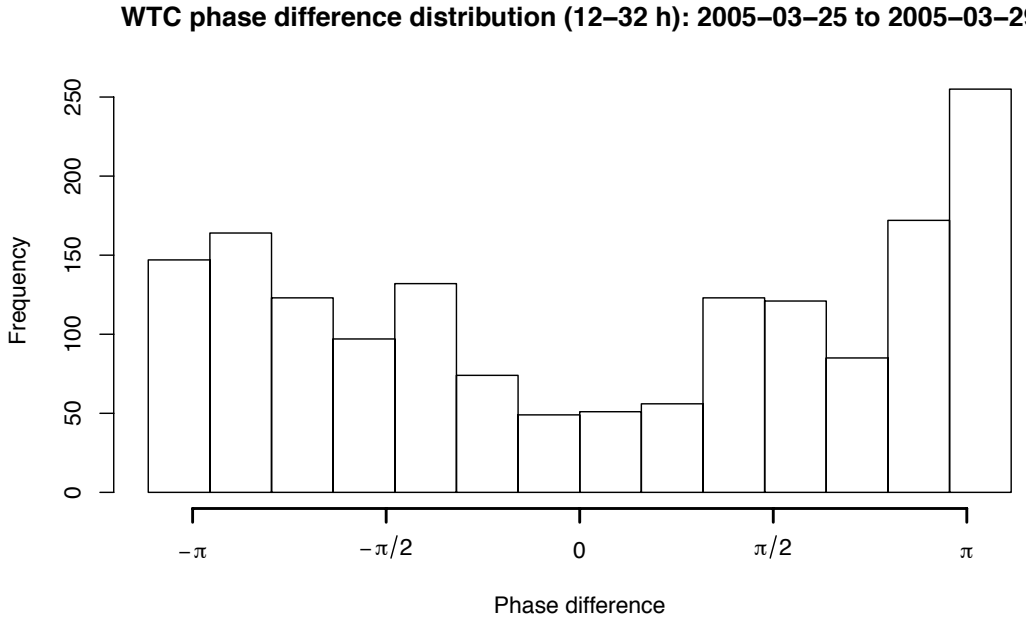

Figure 3.40. Phase difference histogram for the 2005-03-23 event. Bins display the number of phase difference observations in a given range between $-\pi$ and π for each storm's middle four days at time scales between 12 and 32 h. See Figure 3.30 for an explanation of phase differences.

4. DISCUSSION

4.1. Precipitation-net snowmelt response categories

Storm events with the greatest amount of snowmelt augmentation of precipitation (persistent melt category) were associated with the highest peak flows at WS8 and Lookout Creek. By quantifying the amount and timing of net snowmelt, the categorization scheme distinguishes among rain-on-snow events, and provides a means of predicting peak discharge magnitude.

4.2. What drives net snowmelt?

Net snowmelt occurs once a snowpack is ripe, meaning it is isothermal at 0°C and its water holding capacity is satisfied (USACE, 1956). In order for a non-isothermal, dry snowpack to become ripe and commence net snowmelt, energy must be added to the system. This energy can come in several forms: shortwave and longwave radiation; latent and sensible heat; advective heat from rainwater; and heat conducted from the ground (USACE, 1956). At seasonal timescales, shortwave and longwave radiation play dominant roles in driving melt (Mazurkiewicz et al., 2008), while at shorter event timescales, particularly during rain-on-snow storms, the turbulent fluxes—latent and sensible heat—dominate (e.g., Harr, 1981; Berris and Harr, 1987; van Heeswijk et al., 1996; Marks et al., 1998).

For storms examined in this study, periods of rapid snowmelt (> 2.0 mm h^{-1}) were accompanied by high winds, consistent with van Heeswijk et al. (1996). The events with the highest melt totals also had the 1st- and 3rd-ranked average wind speed. The 1996-02-02 storm, which had the highest average wind speed, was the only event which had consistently high wind speed during the time period of maximum melt and peak streamflow. Such a pattern is likely responsible for the storm's supersized melt as described by Marks et al. (1998).

Dewpoint temperature and its effect on precipitation phase explained net snowmelt magnitude and timing. Increasing dewpoint temperature above 0.5°C was associated with shifts from net negative to net positive snowmelt, and vice-versa. While rain accounted for 66% of precipitation time, 91% of net snowmelt time

coincided with rain. In contrast, mixed precipitation and snow accounted for 24%, and 10% of precipitation time, but only 8% and 2% of net snowmelt time coincided with mixed precipitation and snow, respectively.

Advective heat from rainfall typically comprises a small portion of the rain-on-snow energy budget (e.g., USACE, 1956; Harr, 1981; van Heeswijk, 1996). Nevertheless, higher rates of snowmelt (> 2.0 mm h^{-1}) were associated with higher rates of precipitation. This may occur because heavy precipitation coincides with high wind and warmer temperature, enhancing net snowmelt. On the other hand, high rates of precipitation may push meltwater through the snowpack matrix like a piston, a notion suggested by Jones and Perkins (2010) based off the catchment hydrology work of Torres et al. (1998), Torres (2002), and Ebel and Loague (2008). The latter effect may account for the strong positive relationship between precipitation and net snowmelt values lagged by 1 hour (Figure 3.28; Table 3.7; for a discussion of time lag through the snowpack matrix, please see Chapter 4.3 below).

4.3. Wavelet coherence: Assessing the timing of precipitation and net snowmelt

The two largest Lookout Creek peak discharge events in the study (1996-02-02, 2011-01-11) and two of the smallest events (1996-01-15, and 2006-11-02) displayed a pattern of significant wavelet coherence at multiple time scales over several days, indicating a tightly linked relationship between precipitation and snowmelt. However, pulses of snowmelt were tightly coupled to pulses of precipitation in the former (large) events, but out of phase in the latter (small) events. Cazelles and Stone (2003) noted the peakedness of a phase difference distribution can represent the synchrony between two variables, with larger peaks representing greater synchrony. Therefore, the strongly peaked mid-storm, mid-period phase difference histograms (Appendix F) of these four events are indicative of high degrees of rainfall-net snowmelt synchrony.

For the two large events, the $\pi/2$ distribution peak corresponds to a system where pulses of precipitation lead pulses of snowmelt, implying that precipitation pushes snowmelt through the snowpack matrix. Such an idea is consistent with the timing of the two measurements (Figure 4.1). Precipitation is recorded near-

instantaneously in the heated raingage, while lysimeter outflow measures snowmelt and precipitation that has already traveled through the snowpack (if one is present and deep enough to cause a temporal lag) and the snowmelt lysimeter instrumentation. A perfect synchrony of concomitant precipitation and net snowmelt would only be hypothetically possible in a shallow, fully ripe snowpack. In fact, such a relationship was only observed during two events: 1995-11-22 and 1995-12-25. In both instances, pre-event SWE was limited.

The nature of the observed temporal lag is complicated by how water moves through the snowpack. Unlike soil, the snowpack matrix is inherently dynamic with flow pathways constantly changing as snow and ice crystals undergo metamorphosis. Once the snowpack is ripe and its water holding capacity has been satisfied, water can move through the snowpack in several ways, including: as a Darcian front (Wankiewicz, 1978), through preferential flow pathways such as flow fingers (Marsh, 1999), or as a kinematic wave (Jones and Perkins, 2010). It is also unknown whether the snowpack's water output is being sourced from meltwater, precipitation, or a combination of the two.

In the two small storms, precipitation reached its maximum when net snowmelt reached its minimum. This relationship is representative of a system where incoming precipitation is being stored within the snowpack.

Net snowmelt appears to effectively augment peak discharge in any storm in which net snowmelt pulses lag precipitation pulses by $\pi/2$. For example, precipitation led net snowmelt by $\pi/2$ during the middle portion of the 2008-12-27 storm, a persistent accumulation event with negative net snowmelt, which nevertheless produced a peak flow of 4.6 mm h^{-1} at Lookout Creek, the highest of the category.

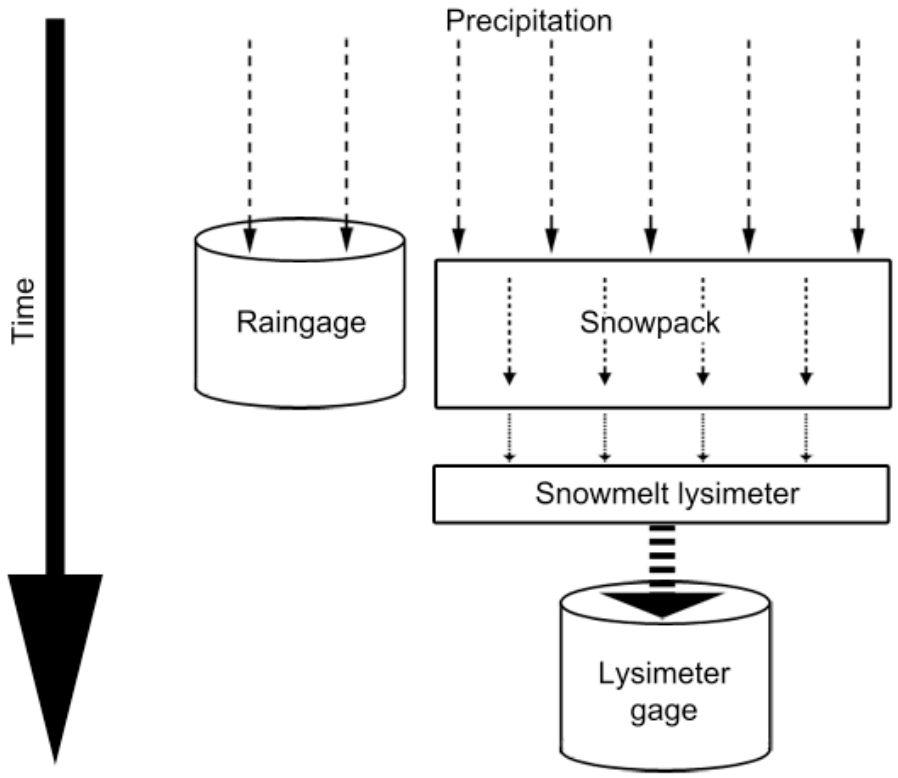

Figure 4.1. Conceptual diagram of the timing of precipitation and net snowmelt. The dashed arrows represent water moving through the system and time is denoted by the solid arrow on the left with time progressing from top to bottom.

4.4. Potential issues and limiters

The rainfall-net snowmelt classification scheme developed for this paper depends on the accuracy of the snowmelt lysimeter data. Although these data were not used to make predictions or assign treatment effects to the various response categories, inaccuracies could lead to the misclassification of events, which would affect the conclusions drawn from the characteristics of each category. Despite these considerations, it is reasonable to assume the snowmelt data were accurate given the lysimeter's low water year bias and the observed coupling between precipitation phase and net snowmelt.

Snow pillow data are lacking at H15MET. Although there is a snow pillow at VANMET, a few km away and in the same elevation range and aspect as WS8, it has many missing values and reported values are not consistent with the lysimeter (sometimes showing no snowpack when the lysimeter is recording positive net

snowmelt or reporting SWE change figures that are vastly different from the lysimeter). Therefore, SNOTEL and Andrews SWE data are presented as a reference only. Additionally, limited snowpack data in the Andrews has hindered past modeling efforts (Perkins and Jones, 2008), making a true assessment of pre-event SWE difficult. Sproles et al. (2013) reported a validated model for SWE in the McKenzie River Basin—in which Lookout Creek is located—but also noted issues with the Andrews SWE data.

This study had a small sample size (n = 26). By expanding the precipitation and peak streamflow selection ranges, it is conceivable that other precipitation-net snowmelt response categories could be observed. In addition, a larger sample size might alter the distribution of the events among categories. Generally, the frequency of rain-on-snow events increases in mountain environments with increases in elevation and decreases in cold-season average temperature (McCabe et al., 2007; Pradhanang et al., 2013), meaning a change in study site could alter the distribution and/or categorization of event types. Furthermore, the small sample size made it difficult to find significant differences between the response categories using the Tukey-Kramer test. Perhaps a larger storm selection would lead to more statistically significant differences.

These analyses were restricted to the snowpack; soil moisture and soil temperature were not considered despite their obvious effect on runoff. Using modeled data for the Andrews, Perkins and Jones (2008) showed that increased soil moisture was associated with higher baseflow and runoff ratios for storms of a given size. In addition, frozen soil has been shown to augment runoff and increase the risk of flooding via reduced soil infiltration capacities (e.g., Niu and Yang, 2006; Shanley and Chalmers, 1999). During 14 of the 26 analyzed storms, at least one monitoring station in the Andrews showed a minimum daily soil temperature at or below 0°C (Daly and McKee, 2012). Nevertheless, despite the omission of soil moisture and soil temperature, total snowmelt explained 63% of the variation in peak discharge at WS8 and 68% at Lookout Creek in the 26 storms in this study.

4.5. Implications

Climate change is expected to reduce mountain snowpacks in the western US (e.g., Mote et al., 2005; Nolin and Daly, 2006; Sproles et al., 2013), but it is unclear how these changes will affect extreme floods in the transient and seasonal snow zones of the Oregon Cascades and other western mountain ranges. Some studies predict an increase in winter daily flows in western Oregon with a warming climate (Jung and Chang, 2011; Surfleet and Tullos, 2012), but the complex interactions between temperature, precipitation, and streamflow in the transient snow zone make broad-scale predictions difficult (Hamlet and Lettenmaier, 2007). This study demonstrates that prediction of future extreme flood events in the transient snow zone will require accurate hourly scale modeling of precipitation rate and snowpack accumulation and melt dynamics in order to identify future conditions that produce synchrony of precipitation and net snowmelt at multiple, coinciding, hourly time scales. Such resolution is not possible with many current global climate models; therefore, the temporal distance between model time steps should be decreased to better correspond with physical flood-generation processes.

Furthermore, identifying climate change scenarios that lead to an increase in highly synchronous persistent melt events could aid in the prediction of future peak flows in the transient snow zone. Modeling could also explore the sensitivity of net snowmelt and peak discharge to changes to boundary conditions (e.g., snowpack depth and thermal quality) and storm characteristics (e.g., wind speed and dewpoint temperature). Hourly-scale precipitation-snowmelt modeling may also be relevant for reservoir operation and flood forecasting. An additional opportunity for further work is the identification of lysimeter output water sources during large events. Isotopic analysis could be used to determine whether output is primarily derived from new precipitation or older meltwater that originated in the snowpack.

5. SUMMARY AND CONCLUSIONS

Hourly precipitation and snowmelt lysimeter data were used to define five precipitation-net snowmelt response categories for 26 large storms in the transient snow zone of Oregon's western Cascades. Each category was defined by the hourly rate of precipitation and precipitation type (rain, mixed, snow), which was based on air temperature and relative humidity effects on dewpoint temperature; these two variables accurately predicted total net snowmelt, which explained 63% of peak discharge at WS8 and 68% at Lookout Creek for these 26 storms. In turn, peak flows at WS8 explained 89% of peak flow at Lookout Creek. Persistent melt events, characterized by concomitant rain and positive net snowmelt, generated on average the largest peak flows at WS8 and Lookout Creek, including the record-setting 1996-02-02 event that caused widespread damage across western Oregon.

Although persistent melt events led to the largest average peak flows, each of the five categories contained storms with peak flows over 3.3 mm h^{-1} at Lookout Creek. The use of wavelet coherence and the mid-storm, mid-period phase difference distribution helped elucidate how this could occur. Many storms contained periods when a pulse of precipitation at the 16-32-hour time scale coincided with conditions suitable for net snowmelt (dewpoint temperature > 0.5°C). Under these conditions, a snowmelt pulse occurred within 4 to 8 hours of the pulse of precipitation, producing a snowmelt-augmented peak discharge. During the two largest peak flows at Lookout Creek, pulses of precipitation at all time scales from 2 to 64 hours coincided with pulses of net snowmelt within $\pi/2$ radians or 1/4 of the wavelength of the precipitation pulses. Essentially, precipitation and net snowmelt were strongly coupled across the dataset at multiple temporal scales with pulses of precipitation leading pulses of net snowmelt. This coupling explains the observation that peak pulses of precipitation at WS8 were reflected in pulses of peak discharge at Lookout Creek, almost 10 km away (Jones and Perkins 2010). The multi-scale precipitation-snowmelt synchrony demonstrated in this present study appears to be the mechanism producing extreme floods, such as the February 1996 and January 2011 events.

Furthermore, it is expected these conclusions regarding the classification of rain-on-snow events and the influence of precipitation-net snowmelt timing on peak

streamflow could be applied to regions with similar snowpack characteristics, such as: the remainder of the Cascade range of the Pacific Northwest, California's Sierra Nevada mountains, the northern Appalachians of New England, and the high Rocky Mountains of the interior western United States in late spring and summer.

BIBLIOGRAPHY

Andreo, B., Jiménez, P., Durán, J. J., Carrasco, F., Vadillo, I., & Mangin, A. (2006). Climatic and hydrological variations during the last 117–166 years in the south of the iberian peninsula, from spectral and correlation analyses and continuous wavelet analyses. Journal of Hydrology, 324(1), 24-39. doi:10.1016/j.jhydrol.2005.09.010

Ashley, S.T., & Ashley, W.S. (2008). Flood fatalities in the United States. J. Appl. Meteor. Climatol., 47, 805–818.

Baliunas, S., Frick, P., Sokoloff, D., & Soon, W. (1997). Time scales and trends in the central england temperature data (1659–1990): A wavelet analysis. Geophysical Research Letters, 24(11), 1351. doi:10.1029/97GL01184

Baptiste, A. (2012). gridExtra: Functions in Grid graphics. R package version 0.9.1. http://CRAN.R-project.org/package=gridExtra

Bierlmaier, Frederick A.; McKee, Arthur. (1989). Climatic summaries and documentation for the primary meteorological station, H.J. Andrews Experimental Forest, 1972 to 1984. Gen. Tech. Rep. PNW-242. Portland, OR: U.S. Department of Agriculture, Forest Service, Pacific Northwest Research Station. 56 p.

Brown, R. B.; Parsons, R. B. (1973). Soils of the reference stands--Oregon IBP. Seattle: University of Washington; Coniferous For. Biome Internal Rep. 128. 76 p. [Online]. Available: http://ir.library.oregonstate.edu/dspace/bitstream/1957/7809/1/Internal%20Report_128.pdf

Carey, S. K., D. Tetzlaff, J. Buttle, H. Laudon, J. McDonnell, K. McGuire, J. Seibert, C. Soulsby, & Shanley, J. (2013). Use of color maps and wavelet coherence to discern seasonal and interannual climate influences on streamflow variability in northern catchments. Water Resour. Res., 49, doi:10.1002/wrcr.20469.

Cazelles, B., & Stone, L. (2003). Detection of imperfect population synchrony in an uncertain world. Journal of Animal Ecology, 72(6), 953-968.

Cazelles, B., Chavez, M., Berteaux, D., Ménard, F., Vik, J. O., Jenouvrier, S., & Stenseth, N. C. (2008). Wavelet analysis of ecological time series. Oecologia, 156(2), 287-304. doi:10.1007/s00442-008-0993-2

Christner, J. & Harr, R. D. (1982). Peak streamflows from the transient snow zone, western Cascades, Oregon. In: Proceedings of the 50th western snow conference; Reno, NV. Fort Collins, CO: Colorado State University Press: 27-38.

Daly, C. & McKee, W. (2012). Air and soil temperature data from the Reference Stand network at the Andrews Experimental Forest, 1971 to present. Long-Term Ecological Research. Forest Science Data Bank, Corvallis, OR. [Database]. Available: http://andrewsforest.oregonstate.edu/data/abstract.cfm?dbcode=MS005 (22 May 2014).

Daly, C. & McKee, W. (2013). Meteorological data from benchmark stations at the Andrews Experimental Forest, 1957 to present. Long-Term Ecological Research. Forest Science Data Bank, Corvallis, OR. [Database]. Available: http://andrewsforest.oregonstate.edu/data/abstract.cfm?dbcode=MS001.

Dyrness, C. T. (1969). Hydrologic properties of soils on three small watersheds in the western Cascades of Oregon. Res. Note PNW-111. Portland, OR: U.S. Department of Agriculture, Forest Service, Pacific Northwest Forest and Range Experiment Station. 17 p.

Dyrness, C. T. & Hawk, G. (1972). Internal Report 43: Vegetation and Soils of the Hi-15 Watersheds, H. J. Andrews Experimental Forest. Coniferous Forest Biome, U. S. Analysis of Ecosystems International Biological Program. University of Washington, Seattle, Washington. pp. 28.

Ebel, B. A., & Loague, K. (2008). Rapid simulated hydrologic response within the variably saturated near surface. Hydrol. Process., 22, 464–471.

Farge, M. (1992). Wavelet transforms and their application to turbulence. Annu. Rev. Fluid Mech., 24, 395-457.

Franklin, Jerry F.; Dyrness, C. T. (1971). A checklist of vascular plants on the H.J. Andrews Experimental Forest, western Oregon. Res. Note PNW-138. Portland, OR: U.S. Department of Agriculture, Forest Service, Pacific Northwest Forest and Range Experiment Station. 37 p.

Gaucherel, C. (2002). Use of wavelet transform for temporal characterisation of remote watersheds. Journal of Hydrology, 269(3), 101-121. doi:10.1016/S0022-1694(02)00212-3

Gouhier, T. (2014). biwavelet: Conduct univariate and bivariate wavelet analyses (Version 0.14). Available from http://biwavelet.r-forge.r-project.org

Grinsted, A., Moore, J.C., Jevrejeva, S. (2004). Application of the cross wavelet transform and wavelet coherence to geophysical time series, Nonlin. Processes Geophys., 11, 561–566, doi:10.5194/npg-11-561-2004. (http://noc.ac.uk/using-science/crosswavelet-wavelet-coherence)

Gu, D., & Philander, S. G. H. (1995). Secular changes of annual and interannual variability in the Tropics during the past century. J. Climate, 8, 864–876.

Hamlet, A. F., & Lettenmaier, D. P. (2007). Effects of 20th century warming and climate variability on flood risk in the western U.S. Water Resources Research, 43(6), W06427. doi:10.1029/2006WR005099

Harr, R. D. (1977). Water flux in soil and subsoil on a steep forested slope. Journal of Hydrology. 33: 37-58.

Harr, R.D. (1981). Some characteristics and consequences of snowmelt during rainfall in western Oregon. J. Hydrol., 53, 277-304.

Harr, R. D. (1986). Effects of clearcutting on rain-on-snow runoff in western oregon: A new look at old studies. Water Resources Research, 22(7), 1095. doi:10.1029/WR022i007p01095

Hothorn, T., Bretz, F., & Westfall, P. (2008). Simultaneous Inference in General Parametric Models. Biometrical Journal 50(3), 346--363.

Johnson, S.; Rothacher, J. 2013. Stream discharge in gaged watersheds at the Andrews Experimental Forest, 1949 to present. Long-Term Ecological Research. Forest Science Data Bank, Corvallis, OR. [Database]. Available: http://andrewsforest.oregonstate.edu/data/abstract.cfm?dbcode=HF004.

Jones, J. A. & Grant, G. E. (1996). Peak flow responses to clear-cutting and roads in small and large basins, western Cascades, Oregon. Water Resources Research. 32(4): 959-974.

Jones, J. A., & Perkins, R. M. (2010). Extreme flood sensitivity to snow and forest harvest, western cascades, oregon, united states. Water Resources Research, 46(12) doi:10.1029/2009WR008632

Jung, I., & Chang, H. (2011). Assessment of future runoff trends under multiple climate change scenarios in the willamette river basin, oregon, USA. Hydrological Processes, 25(2), 258-277. doi:10.1002/hyp.7842

Labat, D. (2005). Recent advances in wavelet analyses: Part 1. A review of concepts. Journal of Hydrology, 314(1), 275-288. doi:10.1016/j.jhydrol.2005.04.003

Labat, D. (2008). Wavelet analysis of the annual discharge records of the world's largest rivers. Advances in Water Resources, 31(1), 109-117. doi:10.1016/j.advwatres.2007.07.004

Labat, D. (2010). Cross wavelet analyses of annual continental freshwater discharge and selected climate indices. Journal of Hydrology, 385(1), 269-278. doi:10.1016/j.jhydrol.2010.02.029

Labat, D., Ronchail, J., & Guyot, J. L. (2005). Recent advances in wavelet analyses: Part 2—Amazon, parana, orinoco and congo discharges time scale variability. Journal of Hydrology, 314(1), 289-311. doi:10.1016/j.jhydrol.2005.04.004

Maraun, D., & Kurths, J. (2004). Cross wavelet analysis: Significance testing and pitfalls. Nonlinear Processes in Geophysics, 11(4), 505-514. doi:10.5194/npg-11-505-2004

Marks, D., Kimball, J., Tingey, D., & Link, T. (1998). The sensitivity of snowmelt processes to climate conditions and forest cover during rain-on-snow: A case study of the 1996 pacific northwest flood. Hydrological Processes, 12(10-11), 1569-1587. doi:10.1002/(SICI)1099-1085(199808/09)12:10/11<1569::AID-HYP682>3.0.CO;2-L

Marks, D., Link, T., Winstral, A., & Garen, D. (2001). Simulating snowmelt processes during rain-on-snow over a semi-arid mountain basin. Annals of Glaciology, 32(1), 195-195. doi:10.3189/172756401781819751

Marks, D., Winstral, A., Reba, M., Pomeroy, J., & Kumar, M. (2013). An evaluation of methods for determining during-storm precipitation phase and the rain/snow transition elevation at the surface in a mountain basin. Advances in Water Resources, 55, 98-110. doi:10.1016/j.advwatres.2012.11.012

Marsh, P. (1999). Snowcover formation and melt: Recent advances and future prospects. Hydrological Processes, 13(14-15), 2117-2134.

Mazurkiewicz, A. B., Callery, D. G., & McDonnell, J. J. (2008). Assessing the controls of the snow energy balance and water available for runoff in a rain-on-snow environment. Journal of Hydrology, 354(1), 1-14. doi:10.1016/j.jhydrol.2007.12.027

McCabe, G. J., Hay, L. E., & Clark, M. P. (2007). Rain-on-snow events in the western united states. Bulletin of the American Meteorological Society, 88(3), 319-328. doi:10.1175/BAMS-88-3-319

McKee, Arthur; Bierlmaier, Frederick. (1987). H.J. Andrews Experimental Forest, Oregon. In: Greenland, David, ed. The climates of the Long-Term Ecological Research sites. Occas. Pap. 44. Boulder, CO: Institute of Arctic and Alpine Research, University of Colorado: 11-17.

Mote, P.W., A.F. Hamlet, M.P. Clark, & Lettenmaier, D.P. (2005). Declining mountain snowpack in western North America. Bull. of the Amer. Meteorol. Soc.,86, 39–49.

N.W.S. (National Weather Service). (2013). 74-year list of severe weather fatalities. Retrieved May 20th, 2014 from http://www.nws.noaa.gov/om/hazstats/resources/weather_fatalities.pdf

Niu, G.Y. &Yang, Z.L. (2006). Effects of frozen soil on snowmelt runoff and soil water storage at a continental scale. Journal of Hydrometeorology, 7: 937–952

Nolin, A. W. & Daly, C. (2006). Mapping "at-risk" snow in the Pacific Northwest, U. S. A., J. Hydrometeorol. 7, 1166-1173.

O'Connor, J. E., & Costa, J. E. (2004). Spatial distribution of the largest rainfall-runoff floods from basins between 2.6 and 26,000 km2 in the united states and puerto rico. Water Resources Research, 40(1), W01107. doi:10.1029/2003WR002247

Perkins, R. M., & Jones, J. A. (2008). Climate variability, snow, and physiographic controls on storm hydrographs in small forested basins, western cascades, oregon. Hydrological Processes, 22(25), 4949-4964. doi:10.1002/hyp.7117

Pradhanang, S. M., Frei, A., Zion, M., Schneiderman, E. M., Steenhuis, T. S., & Pierson, D. (2013). Rain-on-snow runoff events in new york. Hydrological Processes, 27(21), 3035-3049. doi:10.1002/hyp.9864

R Core Team (2014). R: A language and environment for statistical computing. R Foundation for Statistical Computing, Vienna, Austria. URL http://www.R-project.org/.

Ralph, F. M., & Dettinger, M. D. (2012; 2011). Historical and national perspectives on extreme west coast precipitation associated with atmospheric rivers during december 2010. Bulletin of the American Meteorological Society, 93(6), 783. doi:10.1175/BAMS-D-11-00188.1

Ramsey, F. L., Schafer, D. W., & Schafer, D. W. (2013). The statistical sleuth: A course in methods of data analysis. Boston: Brooks/Cole, Cengage Learning, 760 pp.

Ranken, Darrel Wesley. (1974). Hydrologic properties of soil and subsoil on a steep, forested slope. Corvallis, OR: Oregon State University. 117 p. M.S. thesis.

RStudio (2013). RStudio: Integrated development environment for R (Version 0.98.501) [Computer software]. Boston, MA. Available from http://www.rstudio.org/

Ryan, J. & Ulrich, J. (2014). xts: eXtensible Time Series. R package version 0.9-7. http://CRAN.R-project.org/package=xts

Schaefli, B., Maraun, D., & Holschneider, M. (2007). What drives high flow events in the swiss alps? recent developments in wavelet spectral analysis and their application to hydrology. Advances in Water Resources, 30(12), 2511-2525. doi:10.1016/j.advwatres.2007.06.004

Shanley, J.B. & Chalmers, A. (1999). The effect of frozen soil on snowmelt runoff at Sleepers River, Vermont. Hydrological Processes 13:1843–1857.

Smith, J.L. (1974). Hydrology of warm snowpacks and their effects upon water delivery…some new concepts. In: Advanced Concepts and Techniques in the Study of Snow and Ice Resources. National Academy of Sciences, Washington D.C., 76-89.

Sproles, E., Nolin, A., Rittger, K., & Painter, T. (2012). Climate change impacts on maritime mountain snowpack in the oregon cascades. Hydrology and Earth System Sciences Discussions, 9(11), 13037-13081.

Surfleet, C. G., & Tullos, D. (2013). Variability in effect of climate change on rain-on-snow peak flow events in a temperate climate. Journal of Hydrology, 479, 24. doi:10.1016/j.jhydrol.2012.11.021

Swanson, F.J. & Jones, J.A. (2002). Geomorphology and hydrology of the H.J. Andrews Experimental Forest, Blue River, Oregon. In: Moore, George W., ed. Field guide to geologic processes in Cascadia: field trips to accompany the 98th annual meeting of the Cordilleran section of the Geological Society

of America; Corvallis, Oregon. Special paper 36. Portland, OR: Oregon Department of Geology and Mineral Industries: 288-314.

Swanson, Frederick J.; James, Michael E. (1975). Geology and geomorphology of the H.J. Andrews Experimental Forest, western Cascades, Oregon. Res. Pap. PNW-188. Portland, OR: U.S. Department of Agriculture, Forest Service, Pacific Northwest Forest and Range Experiment Station. 14 p.

Swanson, Frederick J.; Swanston, Douglas N. (1977). Complex mass-movement terrains in the western Cascade Range, Oregon. Reviews in Engineering Geology. 3: 113-124.

Torrence, C., Compo, G.P. (1998). A practical guide to wavelet analysis, Bull. Am. Meteorol. Soc., 79, 61–78. (Wavelet software was provided by C. Torrence and G. Compo, and is available at URL: http://atoc.colorado.edu/research/wavelets/)

Torres, R. (2002). A threshold condition for soil-water transport. Hydrol. Process., 16, 2703–2706.

Torres, R., Dietrich, W. E., Montgomery, D. R., Anderson, S. P., & Loague, K. (1998). Unsaturated zone processes and the hydrologic response of a steep, unchanneled catchment. Water Resour. Res., 34(8), 1865–1879, doi:10.1029/98WR01140.

U.S.A.C.E. (U.S. Army Corps of Engineers). (1956). Snow Hydrology. U.S. Army Corps of Engineers, Portland, Oregon, 437 pp.

U.S.A.C.E. (U.S. Army Corps of Engineers). (1996). The Northwest's great storms and floods of Nov. 1995 and Feb. 1996. U.S. Army Corps of Engineers, Portland, Oregon, 24 pp.

Van Heeswijk, M., Kimball, J. & Marks, D. (1996). Simulation of water available for runoff in clearcut forest openings during rain-on-snow events in the western Cascade Range of Oregon and Washington. U.S. Geological Survey Water-Resources Investigations Report, 95-4219.
US Geological Survey, Tacoma, Washington,. 67 pp.

Veleda, D., Montagne, R., & Araujo, M. (2012). Cross-wavelet bias corrected by normalizing scales. Journal of Atmospheric and Oceanic Technology, 29(9), 1401.

Wang, B. & Wang, Y. (1996). Temporal structure of the SouthernOscillation as revealed by waveform and wavelet analysis. J.Climate, 9, 1586–1598.

Wankiewicz, A. (1978). A review of water movement in snow. In Proceedings, Modeling of Snow Cover Runoff, ed. Colbeck, S.C. & Ray, M. Cold Regions Research Engineering Lab, U.S. Army Corps of Engineers: pp. 222 -268.

Wickham, H. (2009). ggplot2: Elegant graphics for data analysis. New York; London: Springer Science + Business Media.

Wickham, H. (2011). The Split-Apply-Combine Strategy for Data Analysis. Journal of Statistical Software, 40(1), 1-29. URL http://www.jstatsoft.org/v40/i01/.

Zeileis, A. & Grothendieck, G. (2005). zoo: S3 Infrastructure for Regular and Irregular Time Series. Journal of Statistical Software, 14(6), 1-27. URL http://www.jstatsoft.org/v14/i06/

APPENDICES

Appendix A.

Table A-1. Lookout Creek and WS8 peak flow and CS2MET and H15MET 3-day precipitation values for the storms selected per the methodology of section 2.2. *Indicates storm was removed from event list due to missing data.

Event	Date of peak flow	Lookout Creek peak flow (mm h^{-1})	WS8 peak flow (mm h^{-1})	Peak CS2MET 3-day precipitation (mm)	Peak H15MET 3-day precipitation (mm)
1	1/13/95	2.9	2.4	150.4	110.5
2	11/27/95	1.6	1.5	151.9	118
3	12/30/95	2.0	1.5	159.8	140.8
4	1/20/96	0.7	0.6	155.2	110.9
5	2/7/96	13.2	6.6	277.6	258.9
6	11/19/96	4.9	4.4	229.9	232.4
7	12/4/96	3.3	2.5	160	129.9
8	12/26/96	3.9	3.3	229.9	173.8
9	1/31/97	3.6	2.6	155.2	145.3
10*	10/30/97	2.4	1.3	163.9	150.7
11	11/21/98	3.0	2.1	225.3	223.5
12	12/28/98	5.6	3.4	269.5	201
13	11/26/99	5.2	2.9	270.3	238.1
14*	1/10/00	0.8	0.3	182.4	114.7
15	3/8/03	1.3	1.0	168.9	117.1
16	12/13/03	3.4	2.6	187.2	149
17	12/9/04	1.9	1.2	156	138.4
18	3/28/05	1.2	1.0	153.1	126.2
19	12/30/05	5.0	3.7	205.2	203.2
20*	1/10/06	4.4	4.1	184.2	219.5
21	11/7/06	1.9	1.2	169.4	178.4
22	12/14/06	3.7	4.0	165.9	173.9
23	10/20/07	0.6	1.1	171.7	168.7
24	11/18/07	1.3	1.6	156	155.2
25	12/28/08	3.2	2.9	204.5	192.6
26	1/1/09	4.6	2.9	119.2	131.9
27	1/16/11	7.5	3.9	157.8	142.9
28*	12/30/11	1.1	2.2	220.4	219.6
29	1/19/12	3.5	2.7	258.5	257.3
30	3/30/12	3.8	3.1	157.8	160.3

Table B-1. Climatic and hydrologic data for the 26 selected events.

Response category	Start date	Total ppt. (mm)	Rain fraction	Snow fraction	Total net melt (mm)	Total WAR (mm)	Total WAR: ppt. ratio	Mean dew. temp. (°C)	Mean air temp. (°C)	Mean wind speed ($m\ s^{-1}$)	WS8 peak flow ($mm\ h^{-1}$)	Lookout Creek peak flow ($mm\ h^{-1}$)
(=)	1995-12-25	182.1	1.0	0.0	11.0	193.1	1.1	3.8	4.7	0.2	1.5	2.0
	1998-11-16	328.3	1.0	0.0	20.2	348.5	1.1	3.2	3.7	0.2	2.1	3.0
	2007-10-15	202.0	1.0	0.0	2.0	204.1	1.0	6.0	6.5	0.1	1.1	0.6
	2012-03-25	200.5	1.0	0.0	-12.5	187.9	0.9	31.7	1.6	0.2	3.1	3.8
(+)	1995-01-08	200.8	1.0	0.0	122.5	323.3	1.6	1.9	2.4	0.3	2.4	2.9
	1995-11-22	256.1	1.0	0.0	53.7	309.8	1.2	6.4	6.7	0.2	1.5	1.6
	1996-02-02	309.6	1.0	0.0	133.4	443.1	1.4	1.3	3.4	0.5	6.6	13.2
	1997-01-26	184.1	1.0	0.0	68.1	252.1	1.4	2.8	3.8	0.2	2.6	3.6
	2005-12-25	343.3	1.0	0.0	37.7	381.0	1.1	3.1	3.3	0.2	3.7	5.0
	2006-12-09	237.1	0.9	0.1	91.1	328.2	1.4	0.1	1.0	0.2	4.0	3.7
	2011-01-11	233.5	1.0	0.0	102.8	336.2	1.4	1.9	2.6	0.1	3.9	7.5
(-)	1996-01-15	265.6	0.6	0.4	-176.2	89.4	0.3	0.1	0.5	0.3	0.6	0.7
	1996-11-29	338.0	0.8	0.2	-109.6	228.4	0.7	0.4	0.9	0.1	2.5	3.3
	2006-11-02	334.7	1.0	0.0	-273.3	61.4	0.2	6.3	6.4	0.1	1.2	1.9
	2008-12-23	355.4	0.7	0.3	-95.3	260.1	0.7	-0.6	-0.5	0.1	2.9	3.2
	2008-12-27	385.6	0.8	0.2	-68.3	317.2	0.8	-0.5	-0.3	0.1	2.9	4.6
	2012-01-14	330.5	0.6	0.4	-101.0	229.5	0.7	4.0	-0.7	0.1	2.7	3.5
(-/+)	1996-11-14	314.2	0.9	0.1	10.1	324.2	1.0	1.9	2.2	0.1	4.4	4.9
	1996-12-21	343.2	0.9	0.1	-27.8	315.4	0.9	1.4	2.2	0.4	3.3	3.9
	1998-12-23	334.8	0.9	0.1	34.7	369.5	1.1	0.4	1.6	0.2	3.4	5.6
	1999-11-21	286.2	1.0	0.0	19.3	305.4	1.1	3.5	4.1	0.2	2.9	5.2
	2003-03-03	196.1	0.8	0.2	31.9	228.0	1.2	2.2	2.6	0.2	1.0	1.3
	2004-12-04	211.6	0.9	0.1	19.8	231.4	1.1	2.6	3.0	0.2	1.2	1.9
(+/-)	2003-12-08	193.0	0.7	0.3	-8.9	184.1	1.0	0.5	0.6	0.1	2.6	3.4
	2005-03-23	213.8	0.8	0.2	-36.7	177.1	0.8	1.3	1.5	0.1	1.0	1.2
	2007-11-13	197.9	0.9	0.1	-28.0	169.8	0.9	2.9	3.3	0.1	1.6	1.3

Table C-1. Mean climatic and streamflow values per response category.

	Mean values per response category											
Response category	Total ppt. (mm)	Total rain (mm)	Rain fraction	Snow fraction	Total net melt (mm)	Total WAR (mm)	Total WAR:ppt. ratio	Mean dew. temp. (°C)	Mean air temp. (°C)	Mean wind speed ($m\ s^{-1}$)	WS8 peak flow ($mm\ h^{-1}$)	Lookout Creek peak flow ($mm\ h^{-1}$)
(=)	228.2	225.9	1.0	0.0	5.2	233.4	1.0	11.2	4.1	0.2	1.9	2.3
(+)	252.1	246.5	1.0	0.0	87.0	339.1	1.4	2.5	3.3	0.2	3.6	5.3
(-)	335.0	249.9	0.7	0.3	-137.3	197.7	0.6	1.6	1.1	0.1	2.1	2.9
(-/+)	281.0	254.6	0.9	0.1	14.6	295.7	1.1	2.0	2.6	0.2	2.7	3.8
(+/-)	201.6	163.1	0.8	0.2	-24.5	177.0	0.9	1.6	1.8	0.1	1.7	2.0

Table D-1. Daily SWE values at the Jump Off Joe (JOJ), McKenzie (MCK), and Roaring River (RR) SNOTEL stations. Start = SWE at event start; end = SWE at event end; max = maximum SWE during event.

Response category	Start date	JOJ start SWE (mm)	JOJ end SWE (mm)	JOJ max SWE (mm)	MCK start SWE (mm)	MCK end SWE (mm)	MCK max SWE (mm)	RR start SWE (mm)	RR end SWE (mm)	RR max SWE (mm)
(=)	1995-12-25	0.0	0.0	0.0	99.1	170.2	195.6	38.1	27.9	53.3
	1998-11-16	0.0	50.8	50.8	40.6	215.9	215.9	55.9	182.9	182.9
	2007-10-15	0.0	0.0	0.0	0.0	40.6	53.3	0.0	10.2	25.4
	2012-03-25	373.4	386.1	388.6	1211.6	1300.5	1303.0	876.3	924.6	924.6
(+)	1995-01-08	416.6	378.5	421.6	678.2	736.6	736.6	500.4	551.2	556.3
	1995-11-22	0.0	0.0	0.0	0.0	73.7	132.1	0.0	17.8	50.8
	1996-02-02	297.2	238.8	320.0	817.9	777.2	960.1	396.2	375.9	408.9
	1997-01-26	221.0	193.0	221.0	1082.0	1056.6	1137.9	673.1	627.4	706.1
	2005-12-25	73.7	55.9	73.7	370.8	485.1	485.1	284.5	330.2	330.2
	2006-12-09	182.9	109.2	195.6	340.4	411.5	411.5	226.1	236.2	241.3
	2011-01-11	246.4	200.7	248.9	635.0	614.7	673.1	434.3	378.5	454.7
(-)	1996-01-15	0.0	195.6	195.6	284.5	599.4	599.4	2.5	266.7	266.7
	1996-11-29	50.8	165.1	165.1	307.3	576.6	576.6	129.5	320.0	320.0
	2006-11-02	5.1	15.2	15.2	25.4	45.7	45.7	17.8	35.6	35.6
	2008-12-23	127.0	210.8	210.8	401.3	614.7	614.7	203.2	350.5	350.5
	2008-12-27	172.7	254.0	254.0	485.1	668.0	668.0	248.9	421.6	421.6
	2012-01-14	10.2	127.0	127.0	254.0	482.6	482.6	172.7	320.0	320.0
(-/+)	1996-11-14	0.0	50.8	73.7	142.2	261.6	292.1	68.6	101.6	129.5
	1996-12-21	238.8	256.5	289.6	812.8	970.3	970.3	495.3	584.2	596.9
	1998-12-23	142.2	172.7	182.9	482.6	701.0	701.0	383.5	500.4	513.1
	1999-11-21	5.1	0.0	35.6	33.0	55.9	86.4	20.3	33.0	55.9
	2003-03-03	66.0	116.8	149.9	480.1	754.4	759.5	172.7	238.8	256.5
	2004-12-04	12.7	15.2	63.5	109.2	246.4	292.1	33.0	119.4	167.6
(+/-)	2003-12-08	71.1	124.5	124.5	264.2	370.8	370.8	193.0	287.0	287.0
	2005-03-23	5.1	53.3	55.9	368.3	513.1	513.1	147.3	254.0	254.0
	2007-11-13	0.0	17.8	20.3	20.3	30.5	33.0	7.6	22.9	25.4

Table D-2. Daily SWE values at VANMET, UPLMET, and CENMET in the H.J. Andrews Experimental Forest. Start = SWE at event start; end = SWE at event end; max = maximum SWE during event.

Response category	Start date	VAN start SWE (mm)	VAN end SWE (mm)	VAN max SWE (mm)	UPL start SWE (mm)	UPL end SWE (mm)	UPL max SWE (mm)	CEN start SWE (mm)	CEN end SWE (mm)	CEN max SWE (mm)
(=)	1995-12-25	63	0	68	31	3	48	NA	NA	NA
	1998-11-16	NA	114	NA	54	171	171	0	26	26
	2007-10-15	NA	NA	NA	NA	NA	NA	NA	NA	NA
	2012-03-25	NA	NA	NA	NA	NA	NA	NA	NA	NA
(+)	1995-01-08	410	396	413	648	661	661	NA	NA	NA
	1995-11-22	0	0	28	2	1	61	NA	NA	NA
	1996-02-02	421	212	421	588	543	693	NA	NA	NA
	1997-01-26	377	260	391	681	771	791	35	9	44
	2005-12-25	NA	160	NA	234	244	283	85	22	85
	2006-12-09	NA	NA	NA	NA	NA	NA	NA	NA	NA
	2011-01-11	NA	NA	NA	NA	NA	NA	NA	NA	NA
(-)	1996-01-15	0	228	228	1	296	296	NA	NA	NA
	1996-11-29	39	217	217	132	375	375	12	140	140
	2006-11-02	0	NA	NA	0	NA	NA	0	NA	NA
	2008-12-23	NA	NA	NA	NA	NA	NA	NA	NA	NA
	2008-12-27	NA	NA	NA	NA	NA	NA	NA	NA	NA
	2012-01-14	NA	NA	NA	NA	NA	NA	NA	NA	NA
(-/+)	1996-11-14	NA	78	NA	19	147	167	0	3	52
	1996-12-21	372	436	483	586	726	817	198	180	273
	1998-12-23	275	356	455	368	478	519	79	24	85
	1999-11-21	1	NA	NA	NA	NA	NA	NA	0	NA
	2003-03-03	126	273	320	142	412	448	25	29	92
	2004-12-04	22	40	91	24	103	145	32	5	76
(+/-)	2003-12-08	43	152	152	135	259	259	18	74	74
	2005-03-23	NA	NA	NA	21	166	166	NA	62	NA
	2007-11-13	NA	NA	NA	NA	NA	NA	NA	NA	NA

Appendix E.

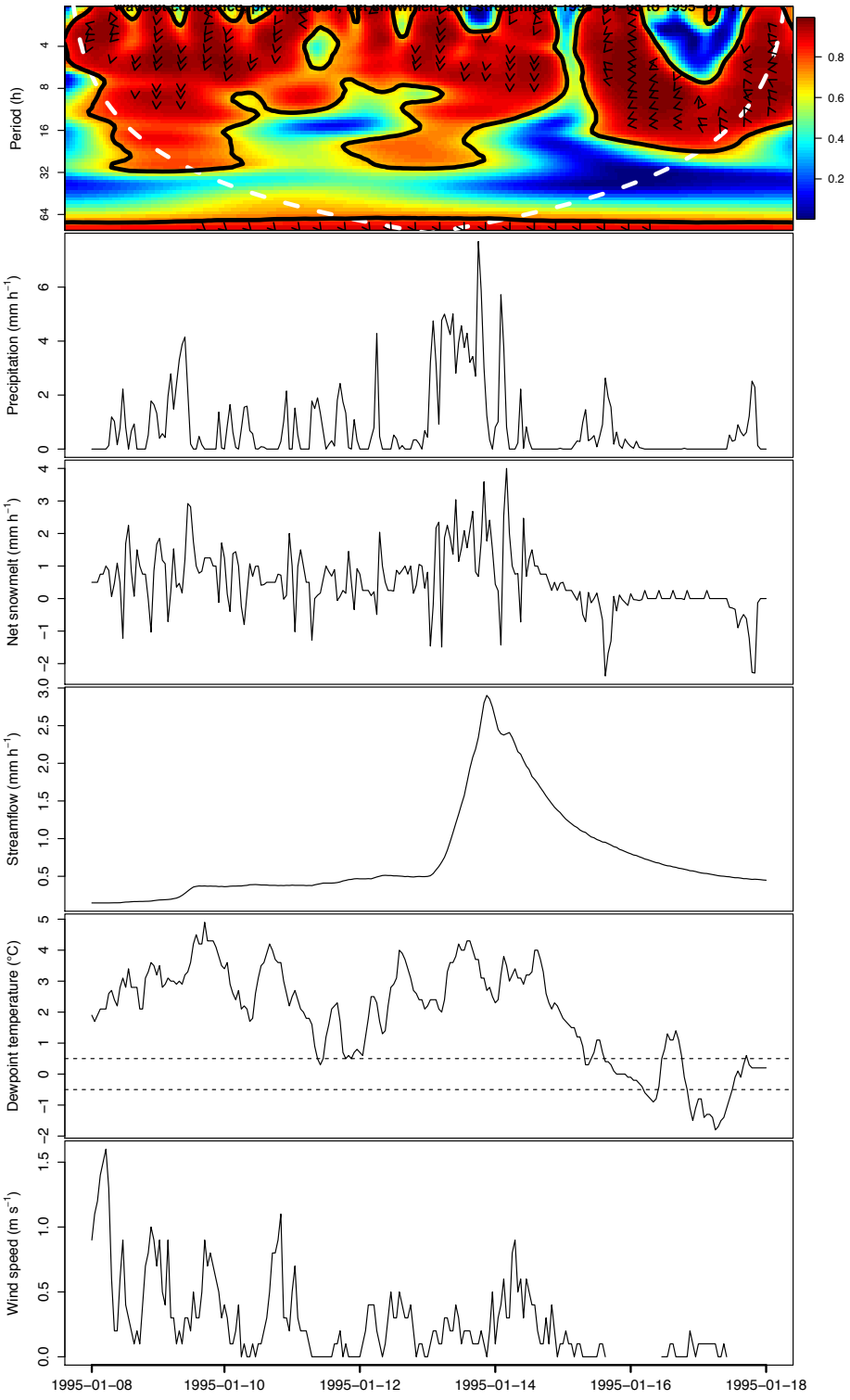

Figure E-1. From top to bottom: Wavelet coherence (with power bar on right), precipitation, net snowmelt, Lookout Creek streamflow, dewpoint temperature, and wind speed for the 1995-01-08 event.

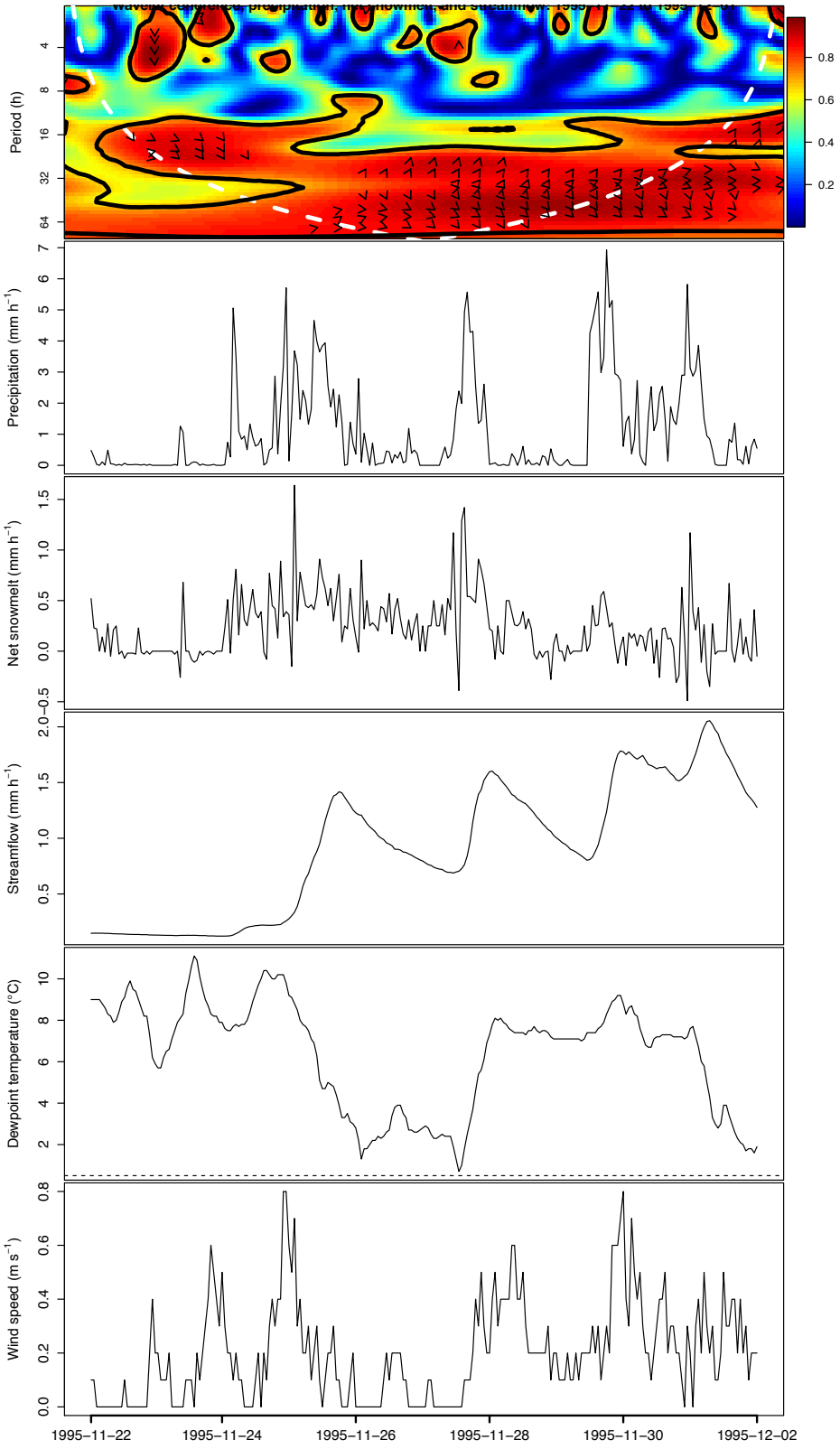

Figure E-2. From top to bottom: Wavelet coherence (with power bar on right), precipitation, net snowmelt, Lookout Creek streamflow, dewpoint temperature, and wind speed for the 1995-11-22 event.

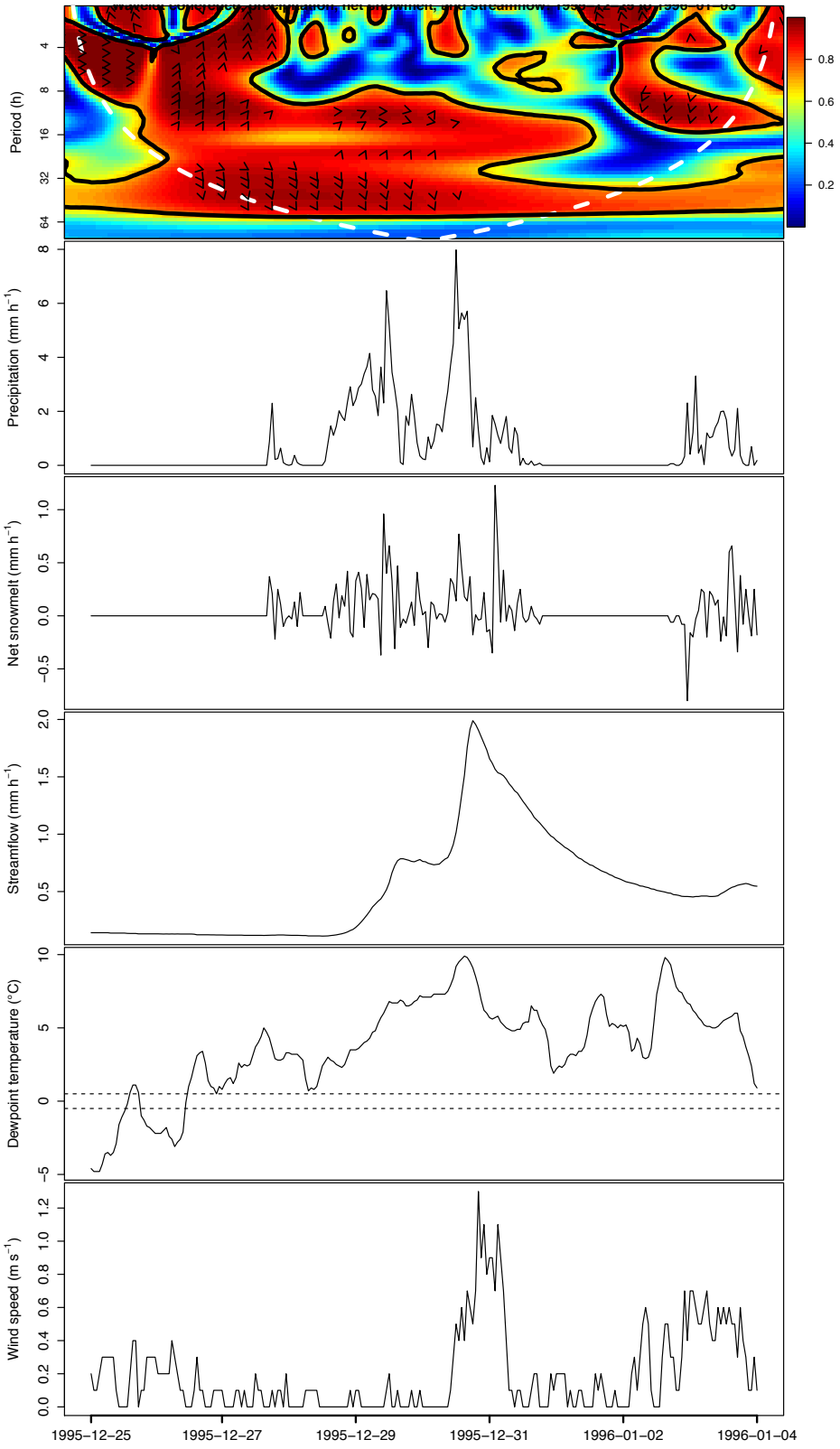

Figure E-3. From top to bottom: Wavelet coherence (with power bar on right), precipitation, net snowmelt, Lookout Creek streamflow, dewpoint temperature, and wind speed for the 1995-12-25 event.

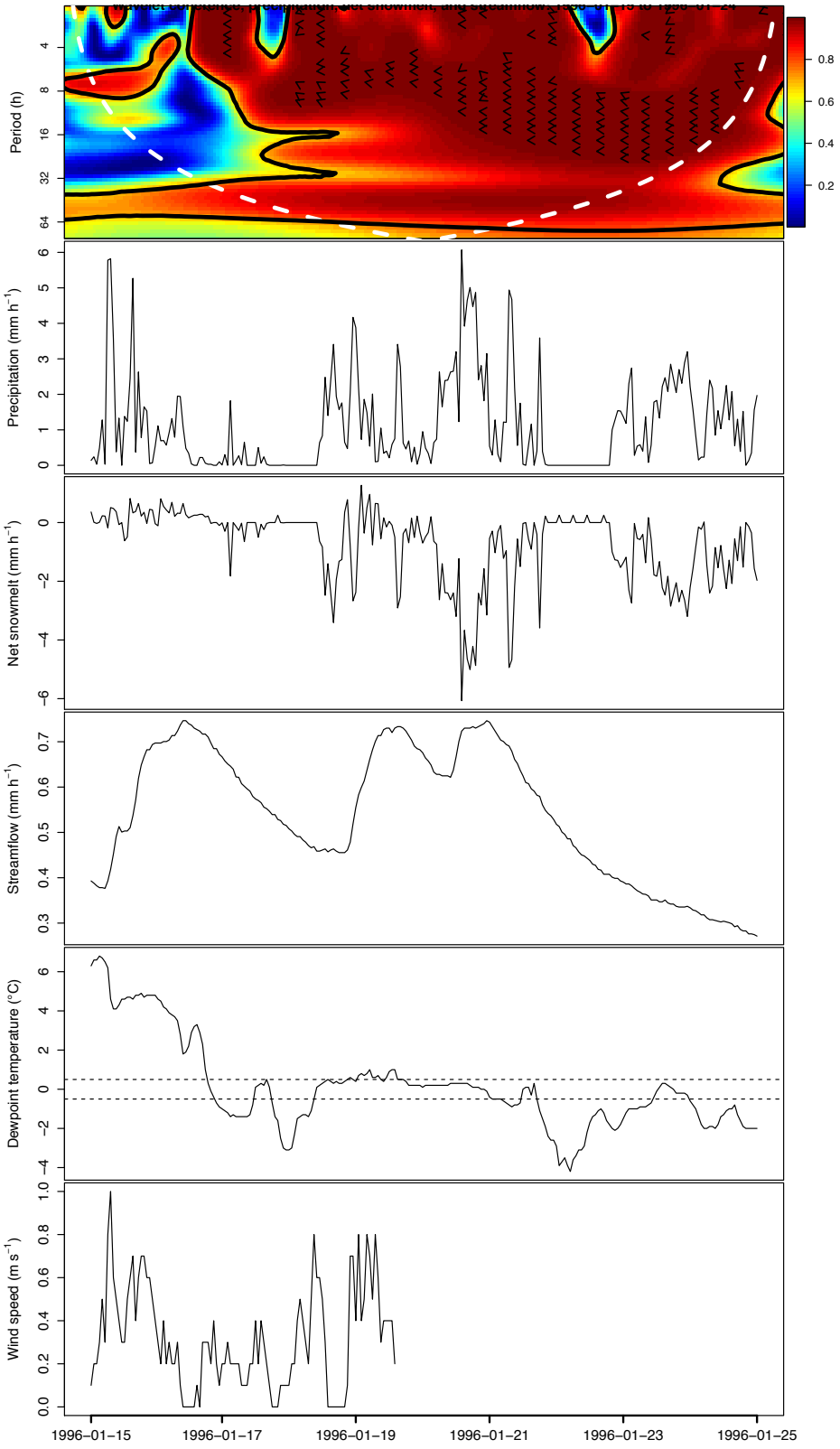

Figure E-4. From top to bottom: Wavelet coherence (with power bar on right), precipitation, net snowmelt, Lookout Creek streamflow, dewpoint temperature, and wind speed for the 1996-01-15 event.

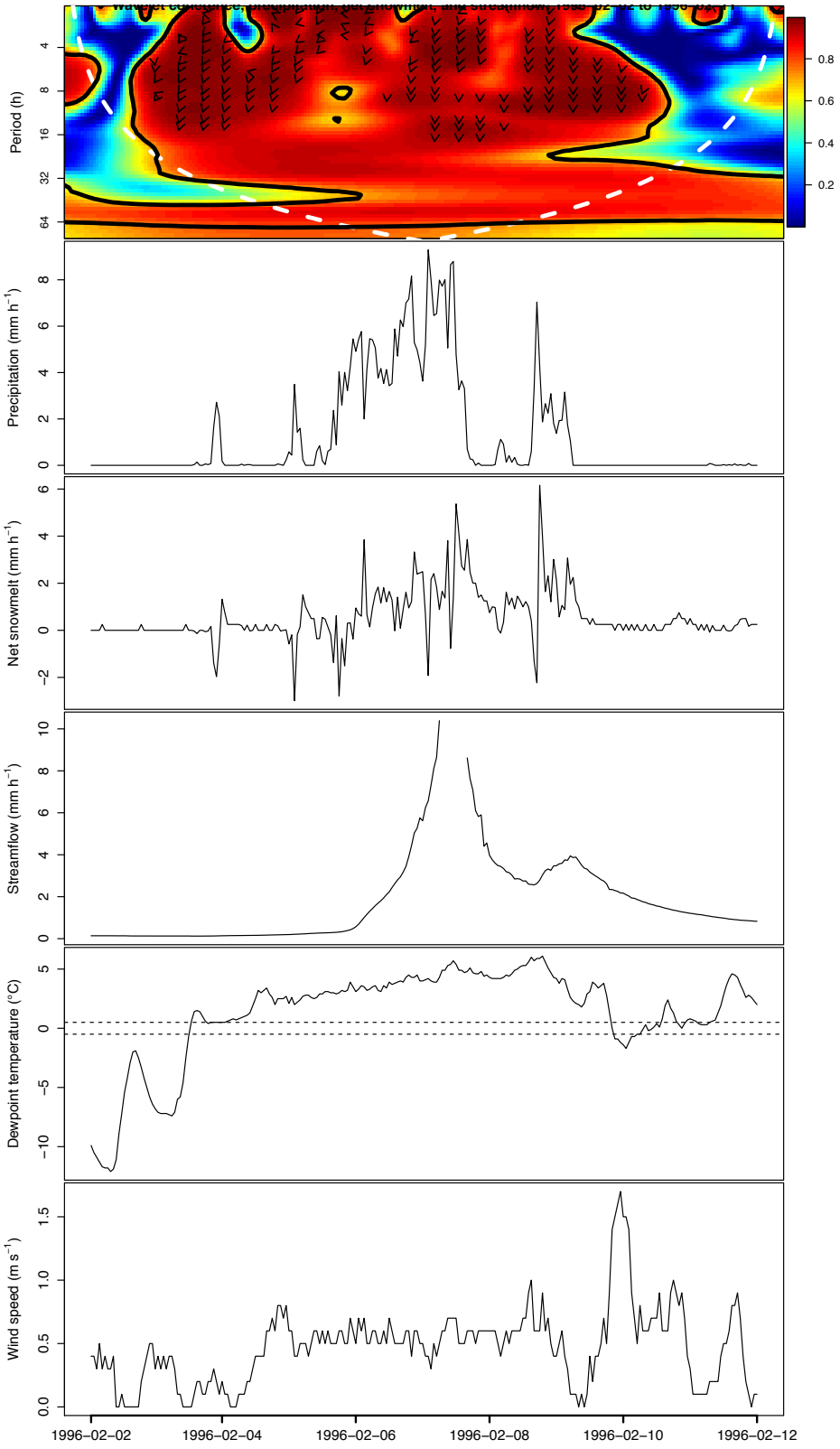

Figure E-5. From top to bottom: Wavelet coherence (with power bar on right), precipitation, net snowmelt, Lookout Creek streamflow*, dewpoint temperature, and wind speed for the 1996-02-02 event. *Lookout Creek peak streamflow was estimated at 13.2 mm h^{-1}.

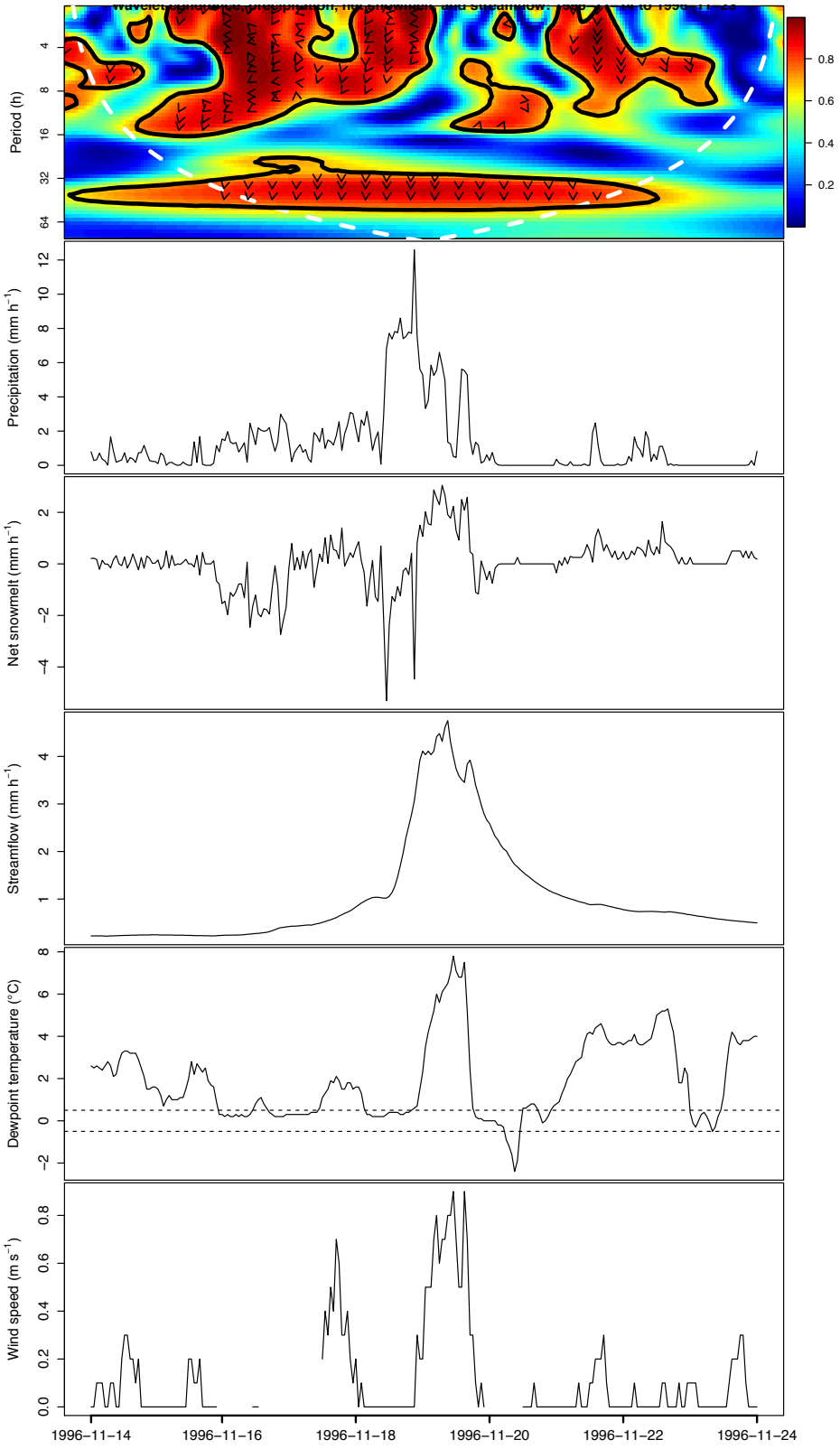

Figure E-6. From top to bottom: Wavelet coherence (with power bar on right), precipitation, net snowmelt, Lookout Creek streamflow, dewpoint temperature, and wind speed for the 1996-11-14 event.

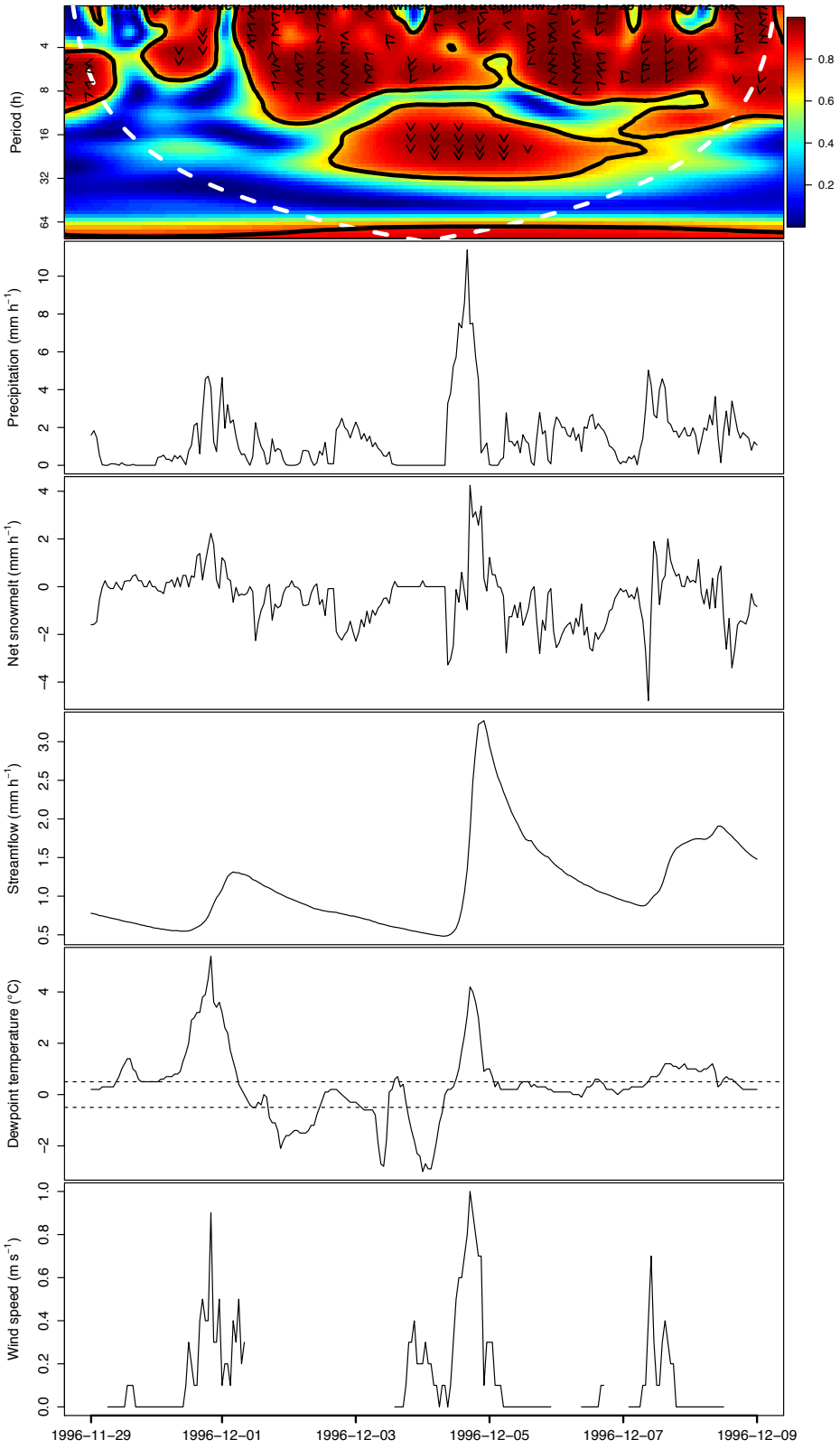

Figure E-7. From top to bottom: Wavelet coherence (with power bar on right), precipitation, net snowmelt, Lookout Creek streamflow, dewpoint temperature, and wind speed for the 1996-11-29 event.

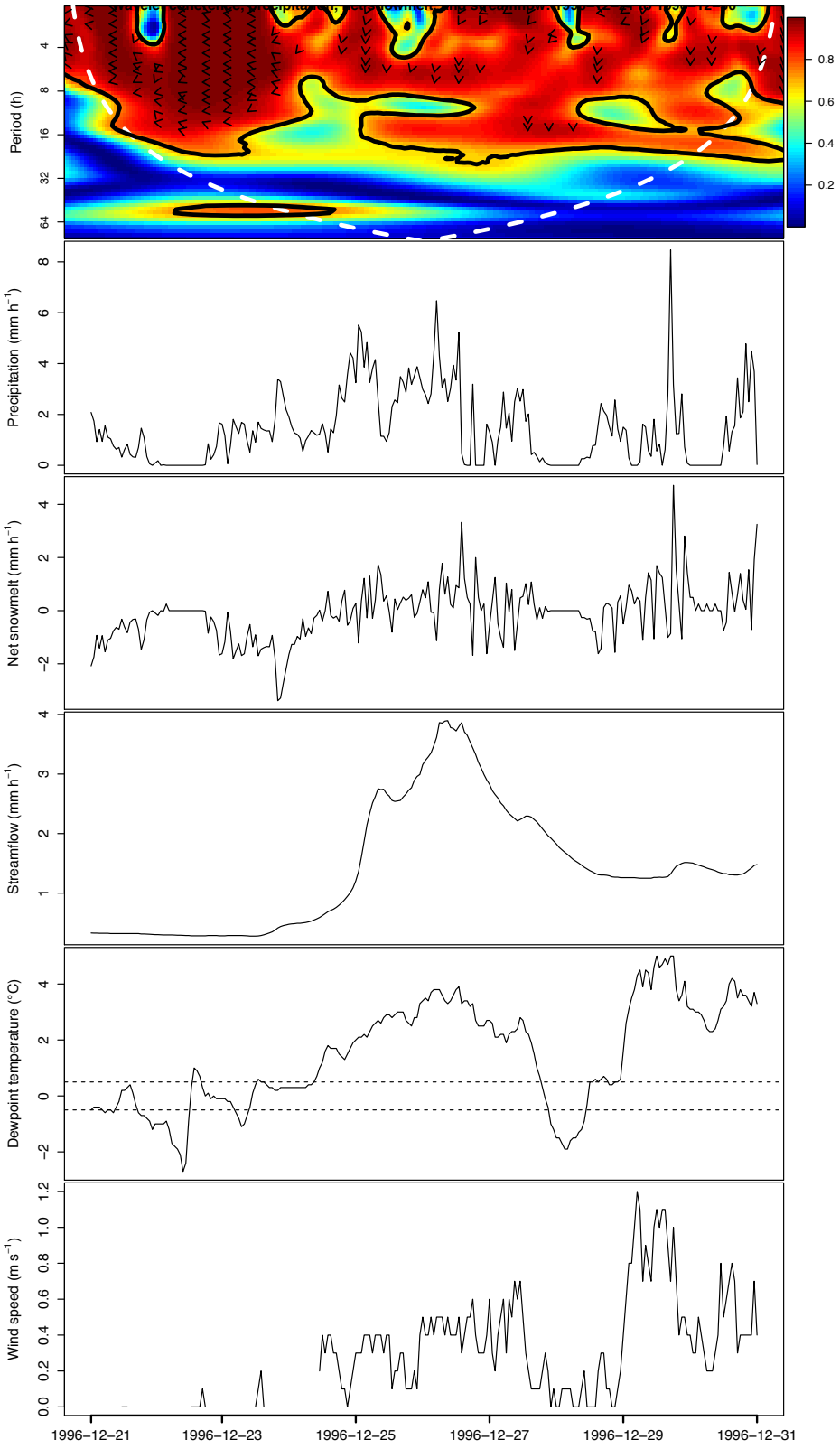

Figure E-8. From top to bottom: Wavelet coherence (with power bar on right), precipitation, net snowmelt, Lookout Creek streamflow, dewpoint temperature, and wind speed for the 1996-12-21 event.

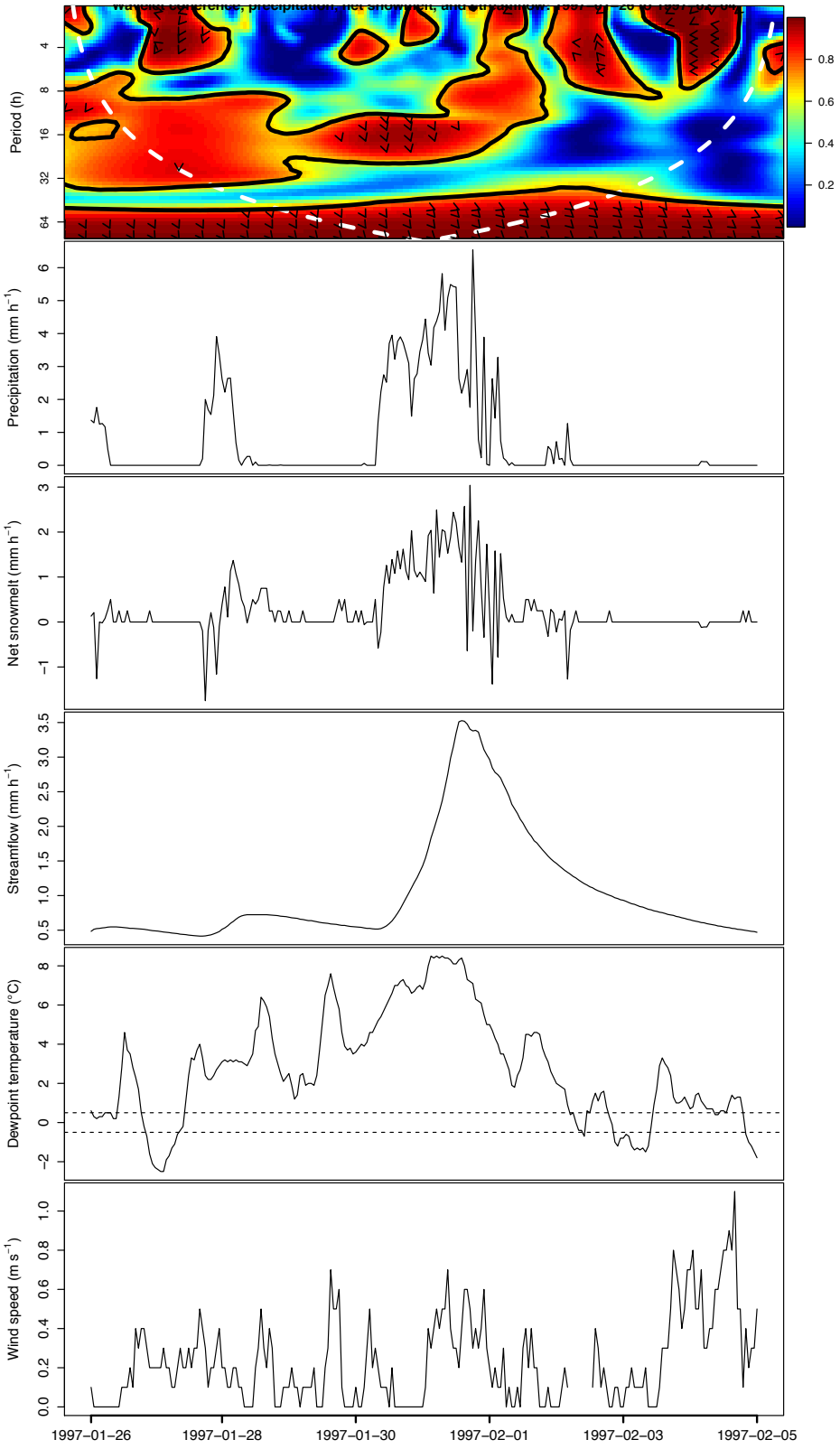

Figure E-9. From top to bottom: Wavelet coherence (with power bar on right), precipitation, net snowmelt, Lookout Creek streamflow, dewpoint temperature, and wind speed for the 1997-01-26 event.

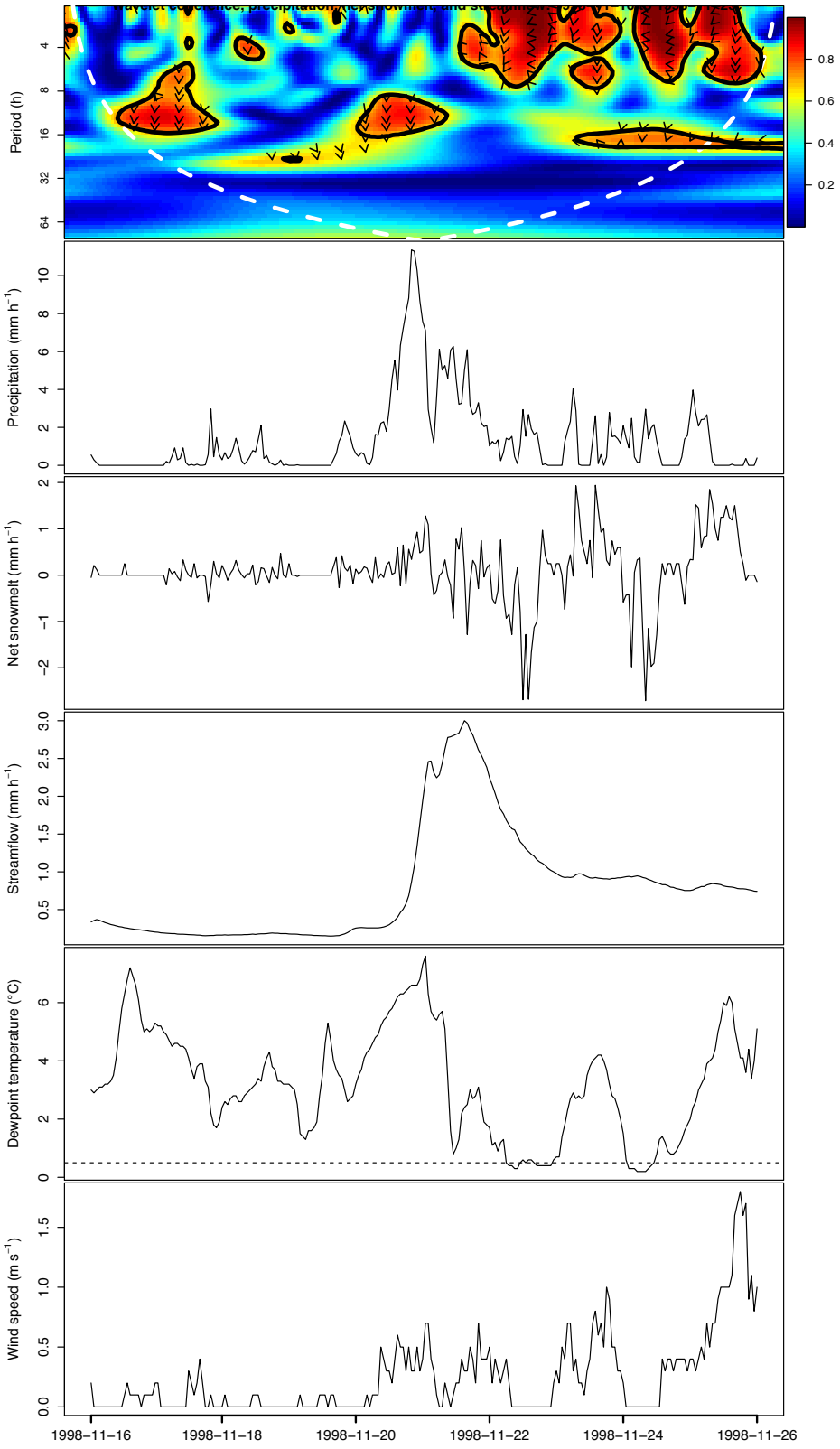

Figure E-10. From top to bottom: Wavelet coherence (with power bar on right), precipitation, net snowmelt, Lookout Creek streamflow, dewpoint temperature, and wind speed for the 1998-11-16 event.

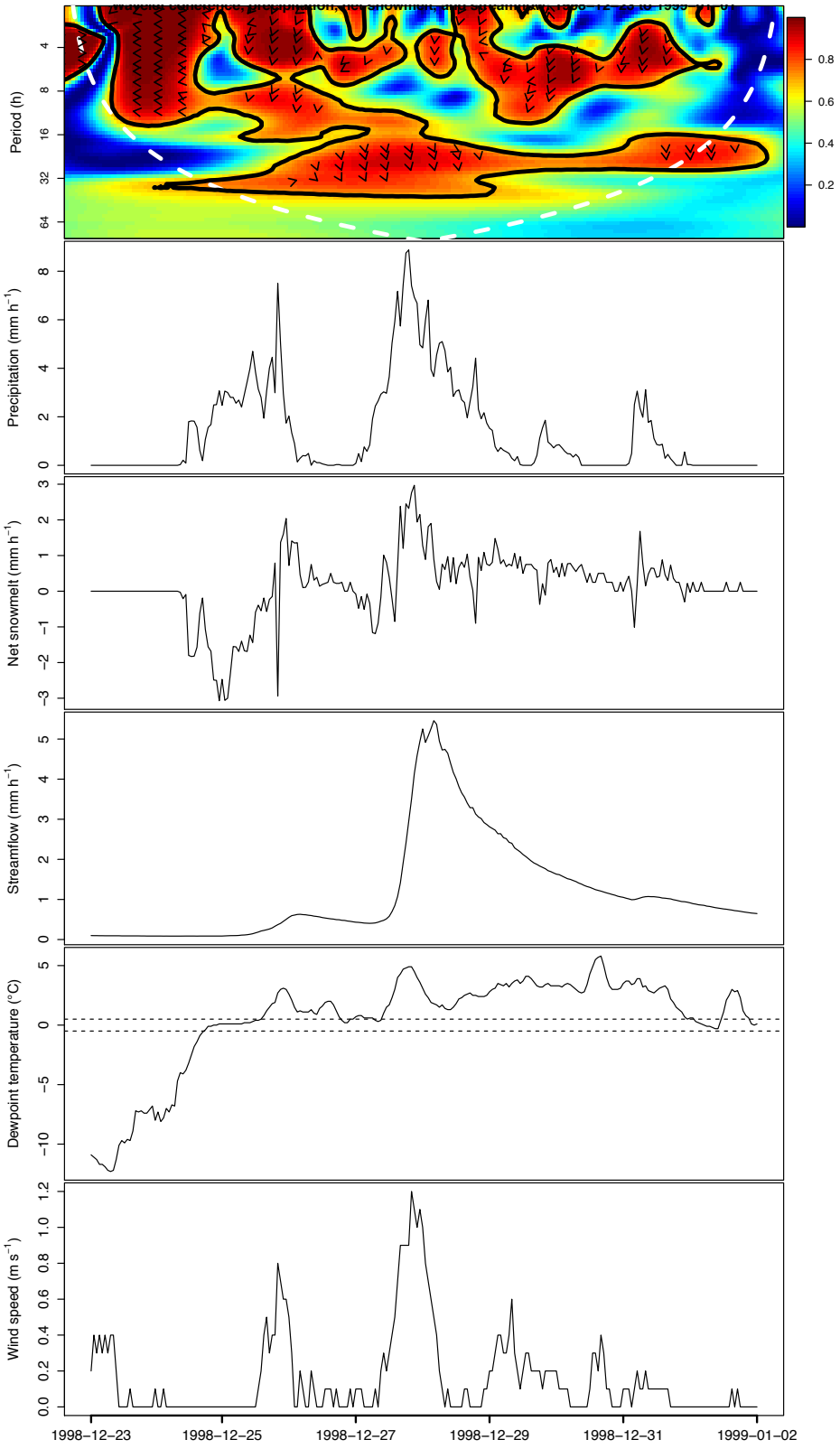

Figure E-11. From top to bottom: Wavelet coherence (with power bar on right), precipitation, net snowmelt, Lookout Creek streamflow, dewpoint temperature, and wind speed for the 1998-12-23 event.

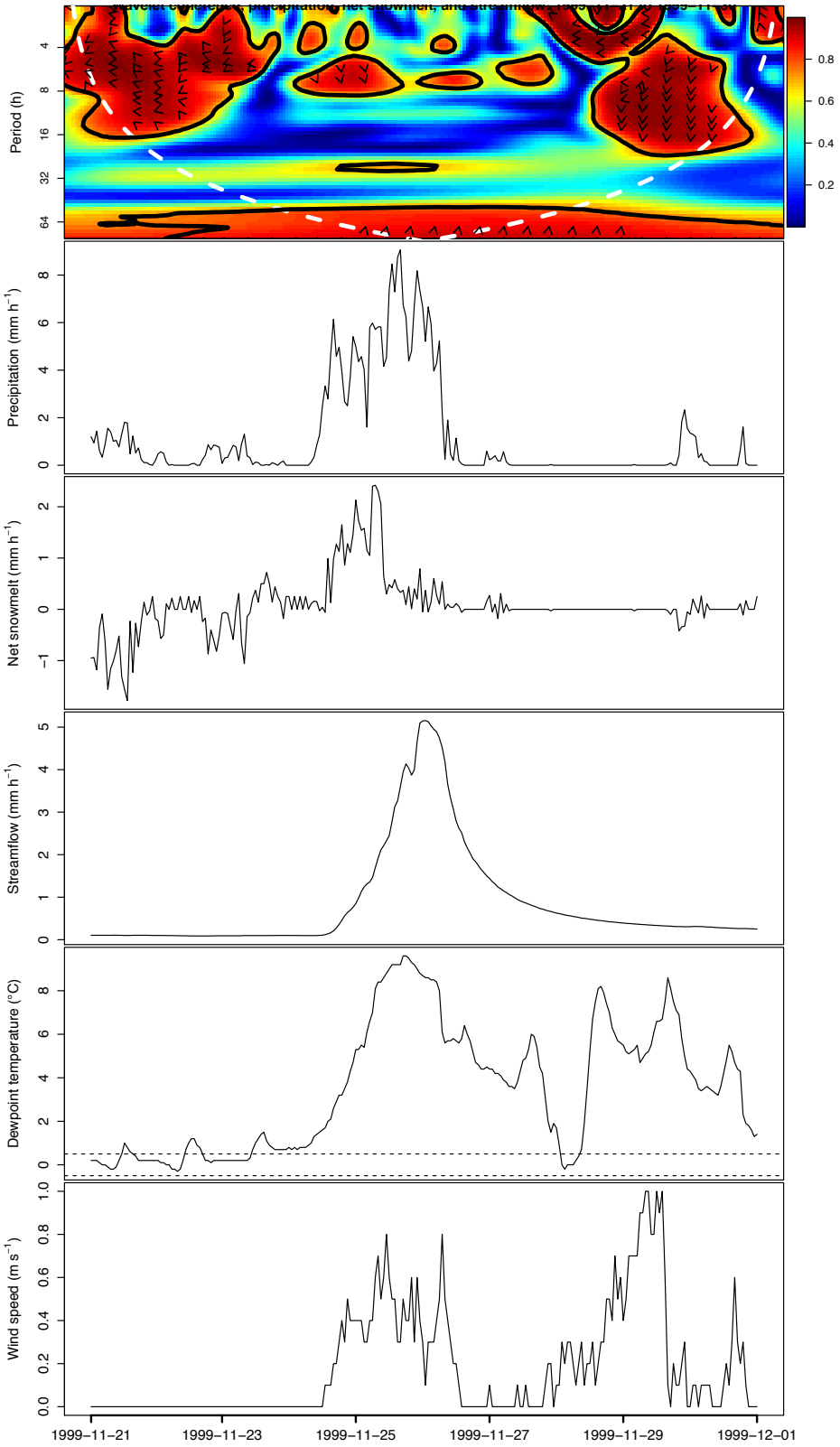

Figure E-12. From top to bottom: Wavelet coherence (with power bar on right), precipitation, net snowmelt, Lookout Creek streamflow, dewpoint temperature, and wind speed for the 1999-11-21 event.

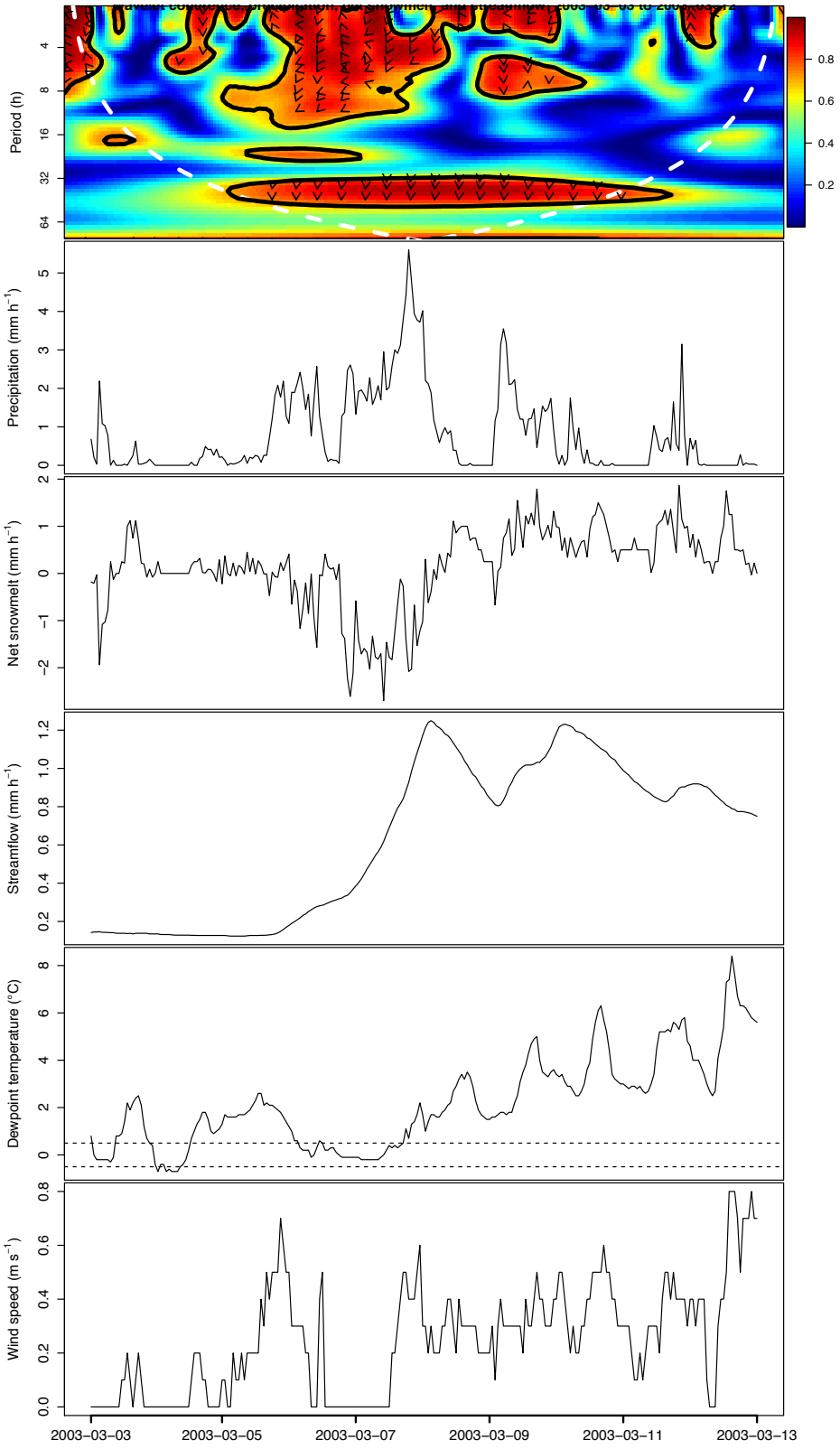

Figure E-13. From top to bottom: Wavelet coherence (with power bar on right), precipitation, net snowmelt, Lookout Creek streamflow, dewpoint temperature, and wind speed for the 2003-03-03 event.

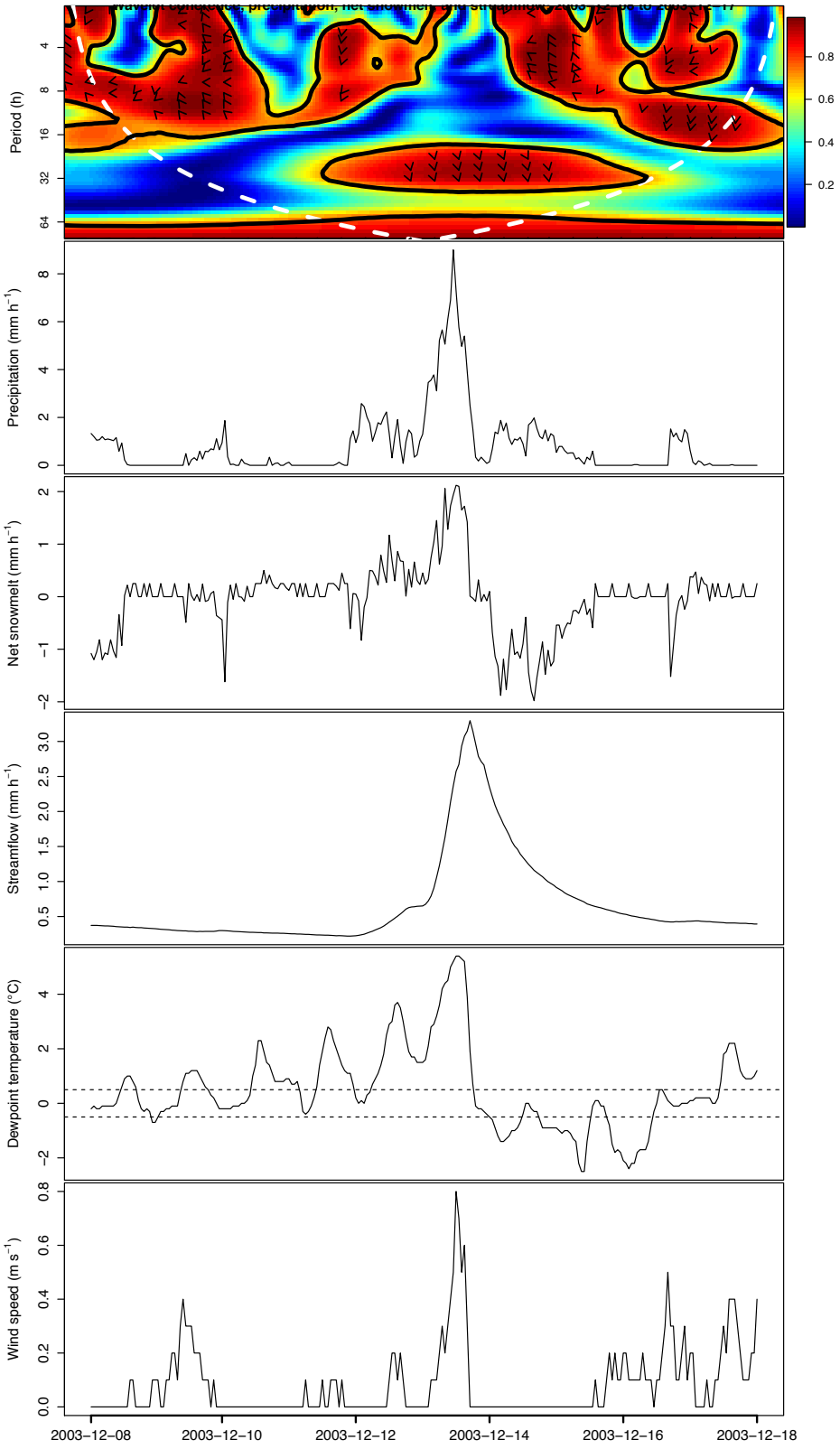

Figure E-14. From top to bottom: Wavelet coherence (with power bar on right), precipitation, net snowmelt, Lookout Creek streamflow, dewpoint temperature, and wind speed for the 2003-12-08 event.

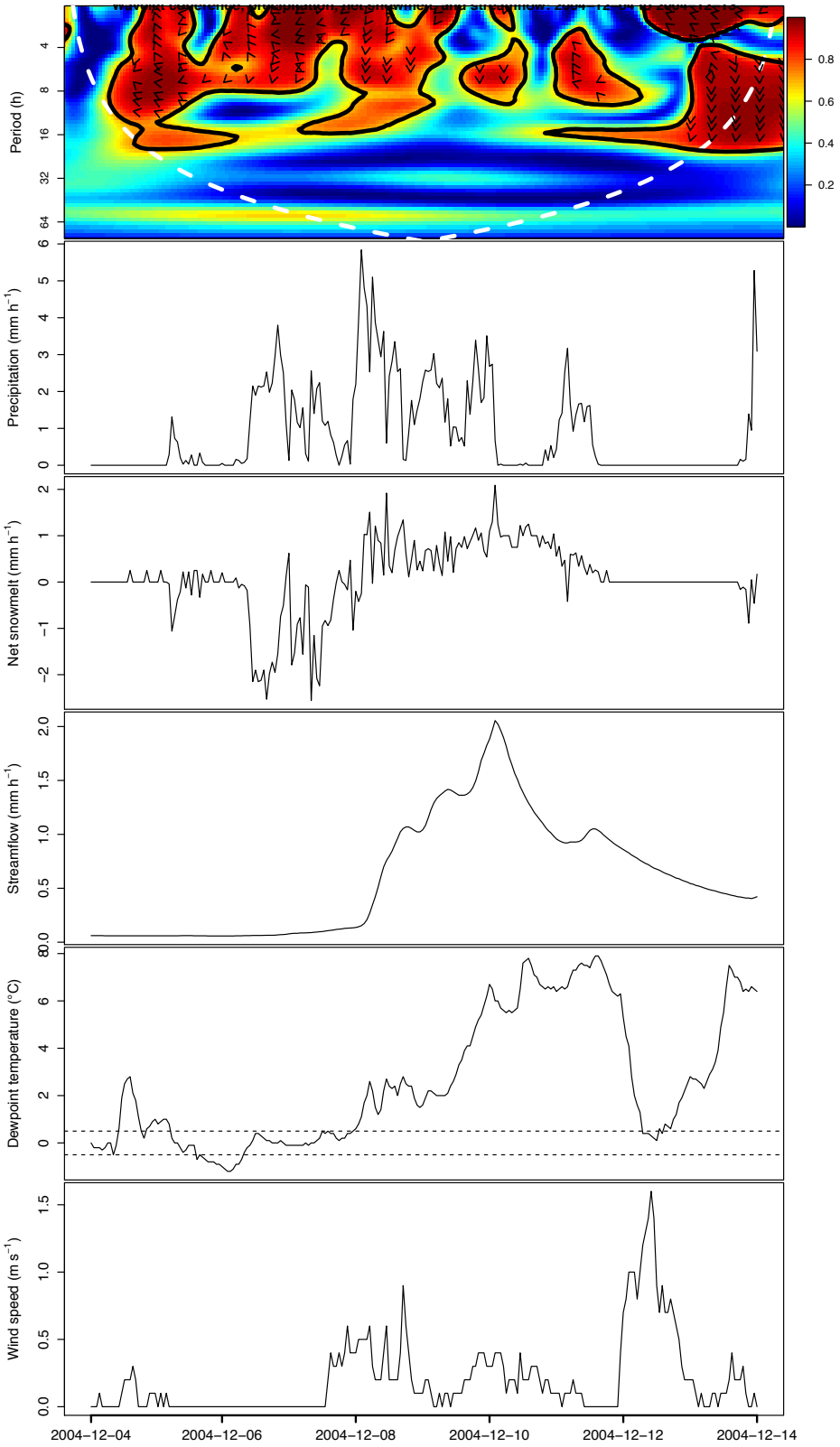

Figure E-15. From top to bottom: Wavelet coherence (with power bar on right), precipitation, net snowmelt, Lookout Creek streamflow, dewpoint temperature, and wind speed for the 2004-12-04 event.

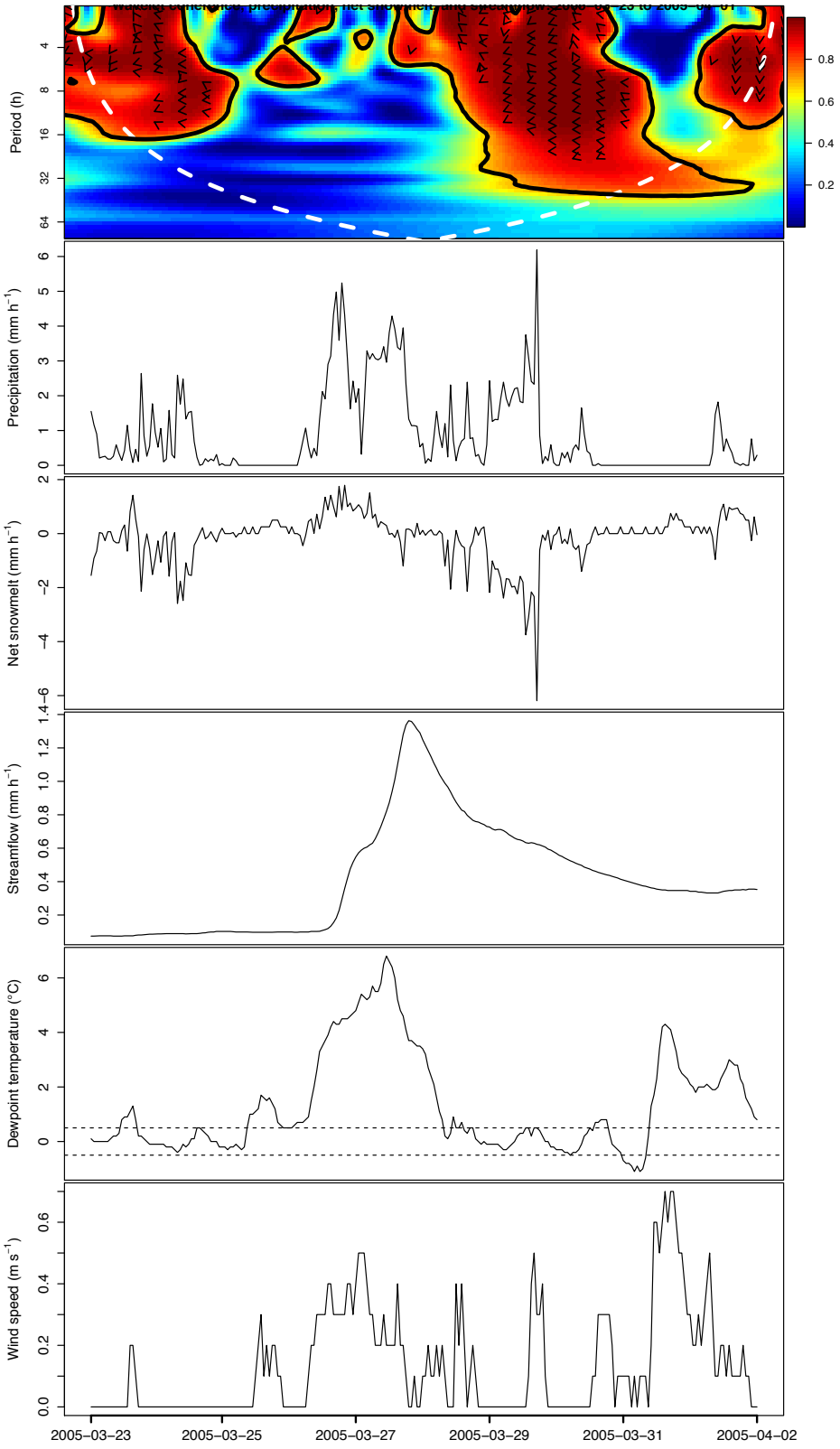

Figure E-16. From top to bottom: Wavelet coherence (with power bar on right), precipitation, net snowmelt, Lookout Creek streamflow, dewpoint temperature, and wind speed for the 2005-03-23 event.

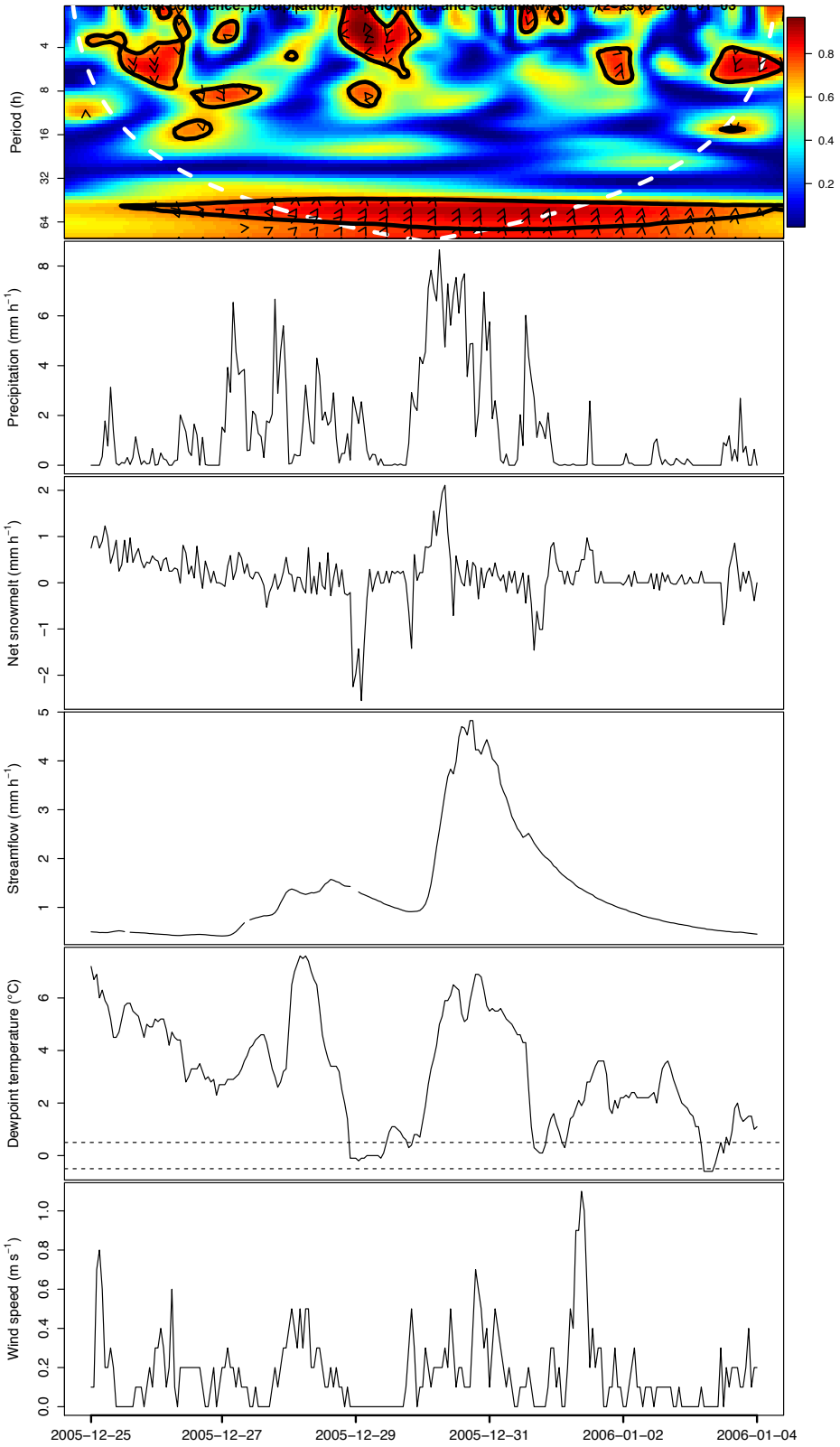

Figure E-17. From top to bottom: Wavelet coherence (with power bar on right), precipitation, net snowmelt, Lookout Creek streamflow, dewpoint temperature, and wind speed for the 2005-12-25 event.

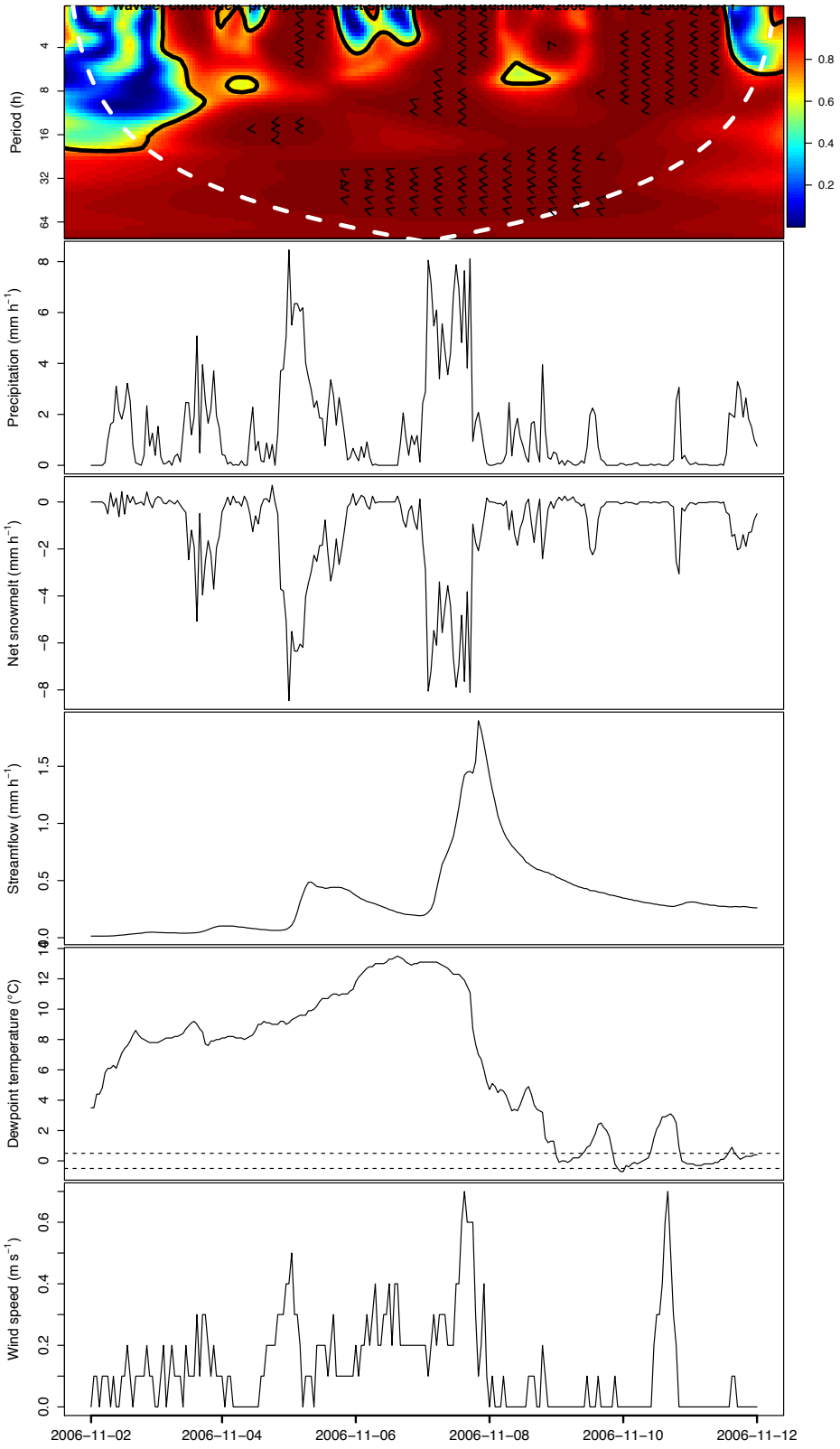

Figure E-18. From top to bottom: Wavelet coherence (with power bar on right), precipitation, net snowmelt, Lookout Creek streamflow, dewpoint temperature, and wind speed for the 2006-11-02 event.

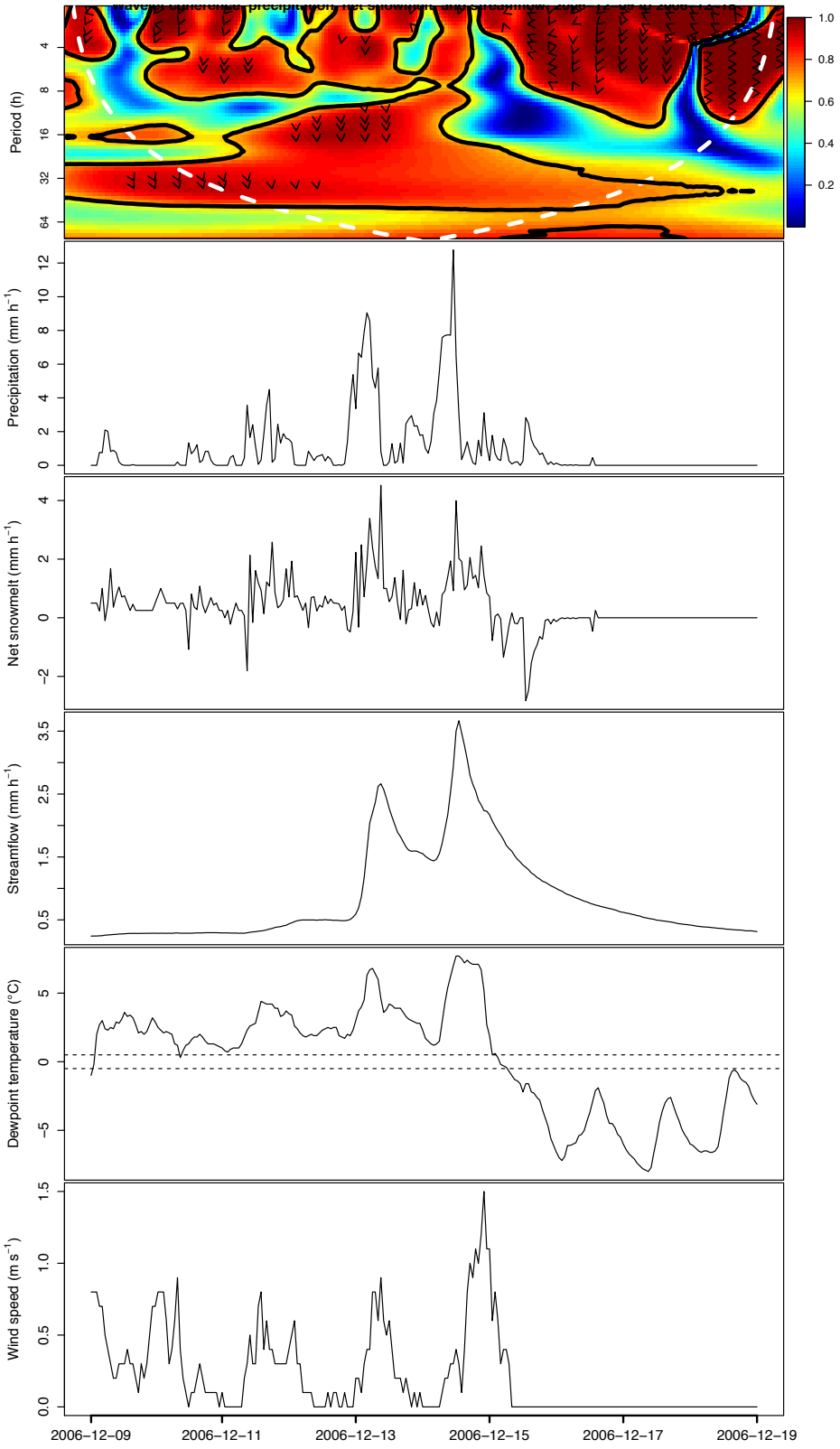

Figure E-19. From top to bottom: Wavelet coherence (with power bar on right), precipitation, net snowmelt, Lookout Creek streamflow, dewpoint temperature, and wind speed for the 2006-12-09 event.

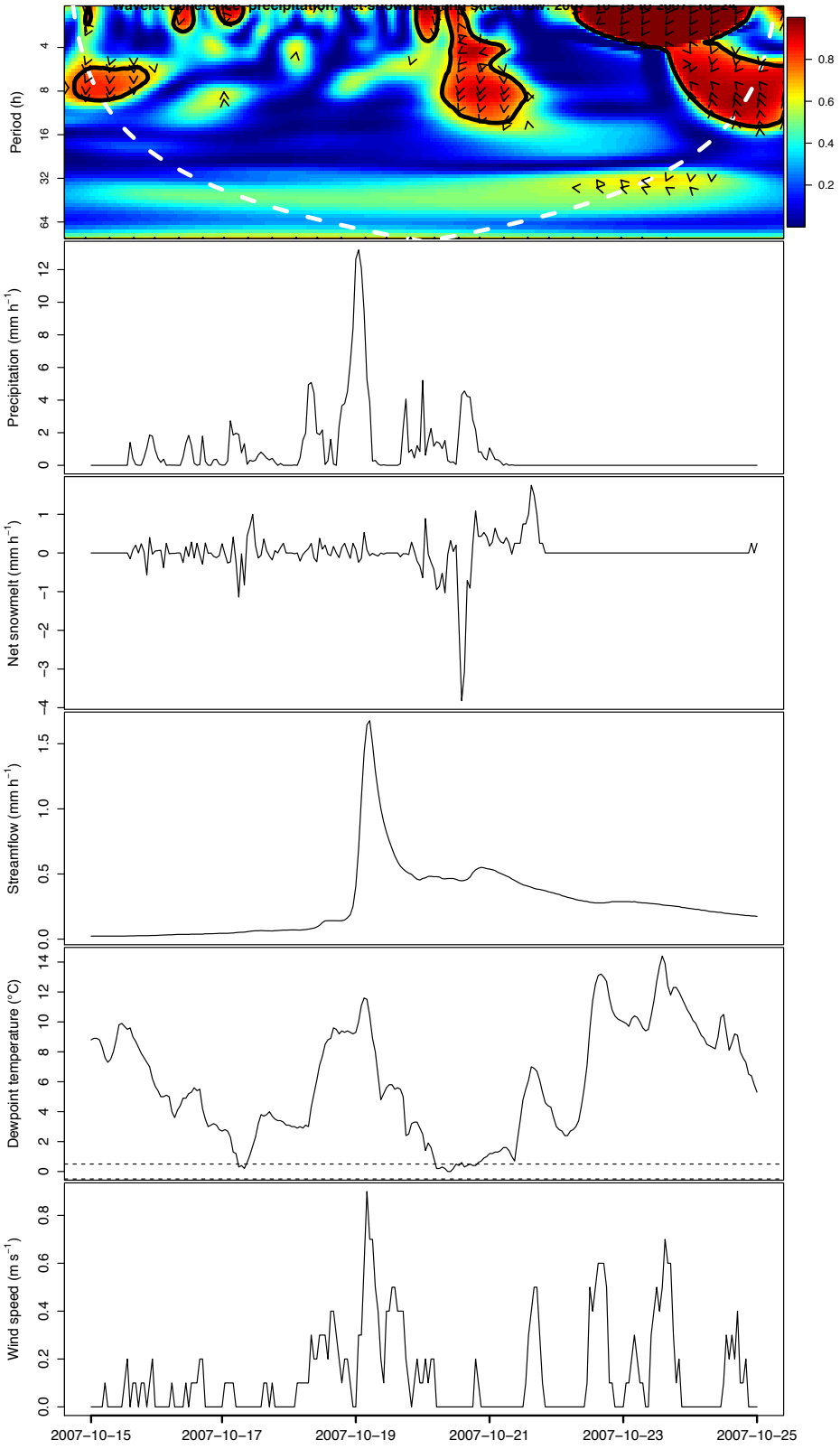

Figure E-20. From top to bottom: Wavelet coherence (with power bar on right), precipitation, net snowmelt, Lookout Creek streamflow, dewpoint temperature, and wind speed for the 2007-10-15 event.

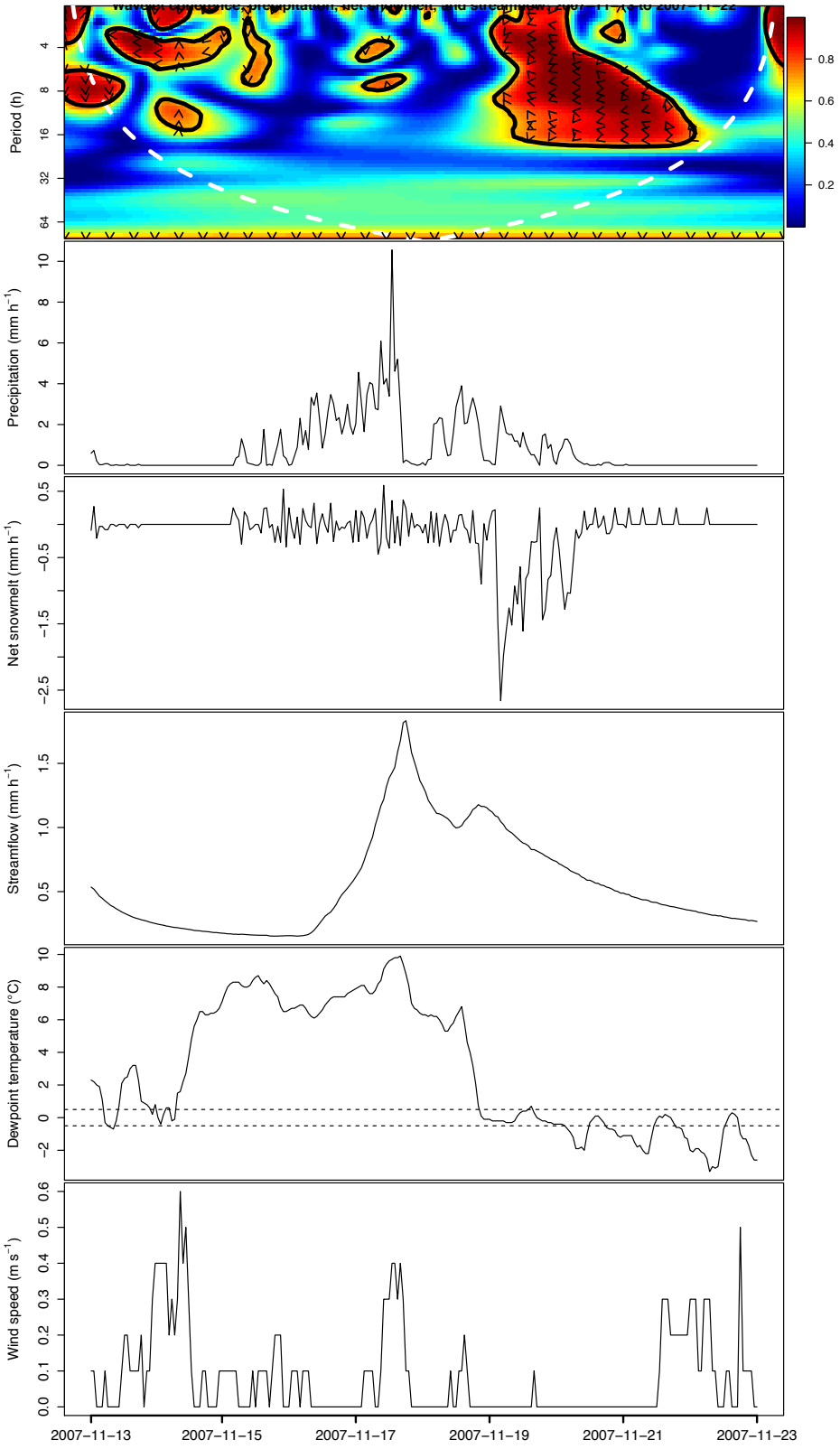

Figure E-21. Wavelet coherence (with power bar on right), precipitation, net snowmelt, Lookout Creek streamflow, dewpoint temperature, and wind speed (from top to bottom) for the 2007-11-17 event.

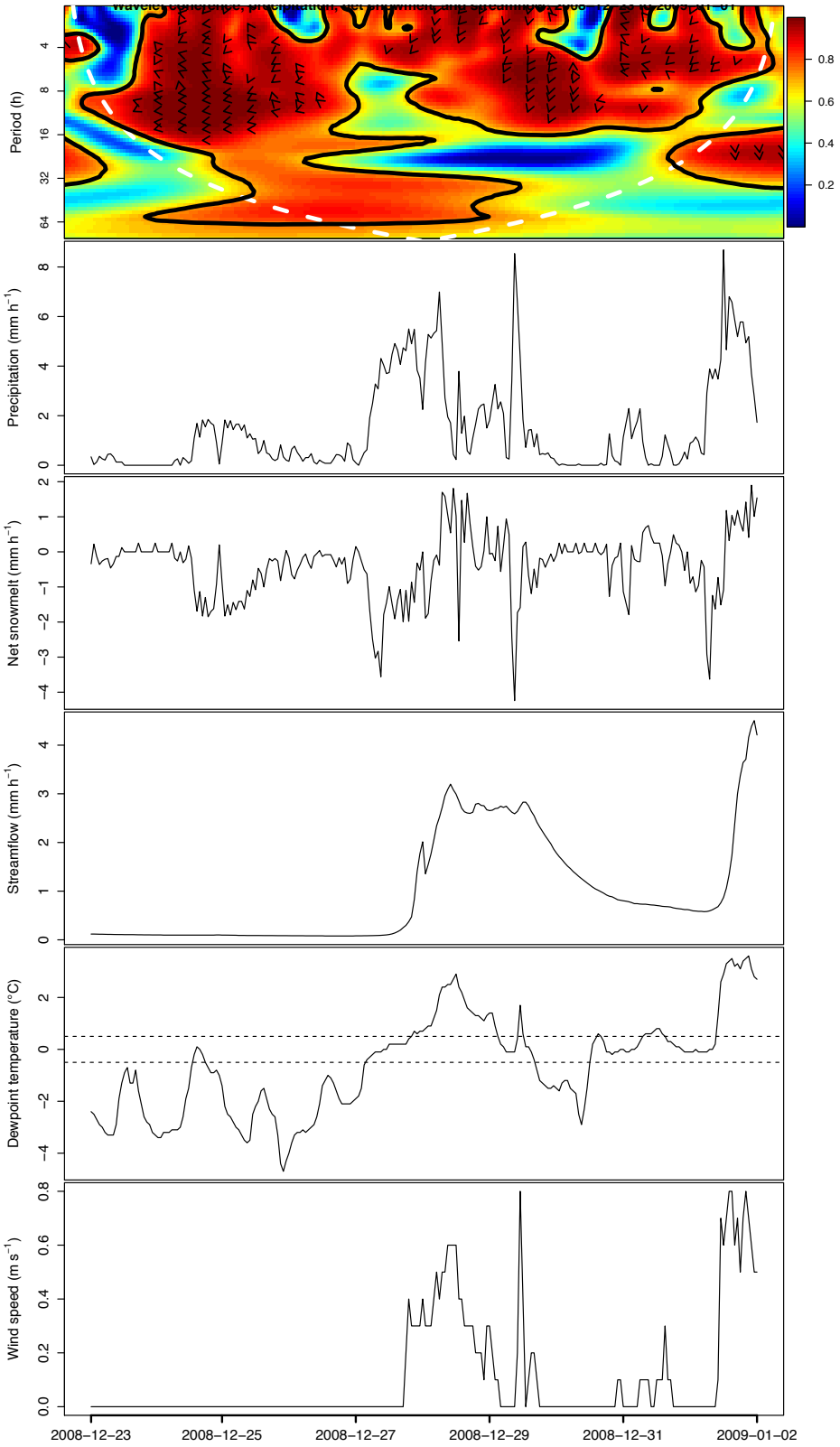

Figure E-22. Wavelet coherence (with power bar on right), precipitation, net snowmelt, Lookout Creek streamflow, dewpoint temperature, and wind speed (from top to bottom) for the 2008-12-23 event.

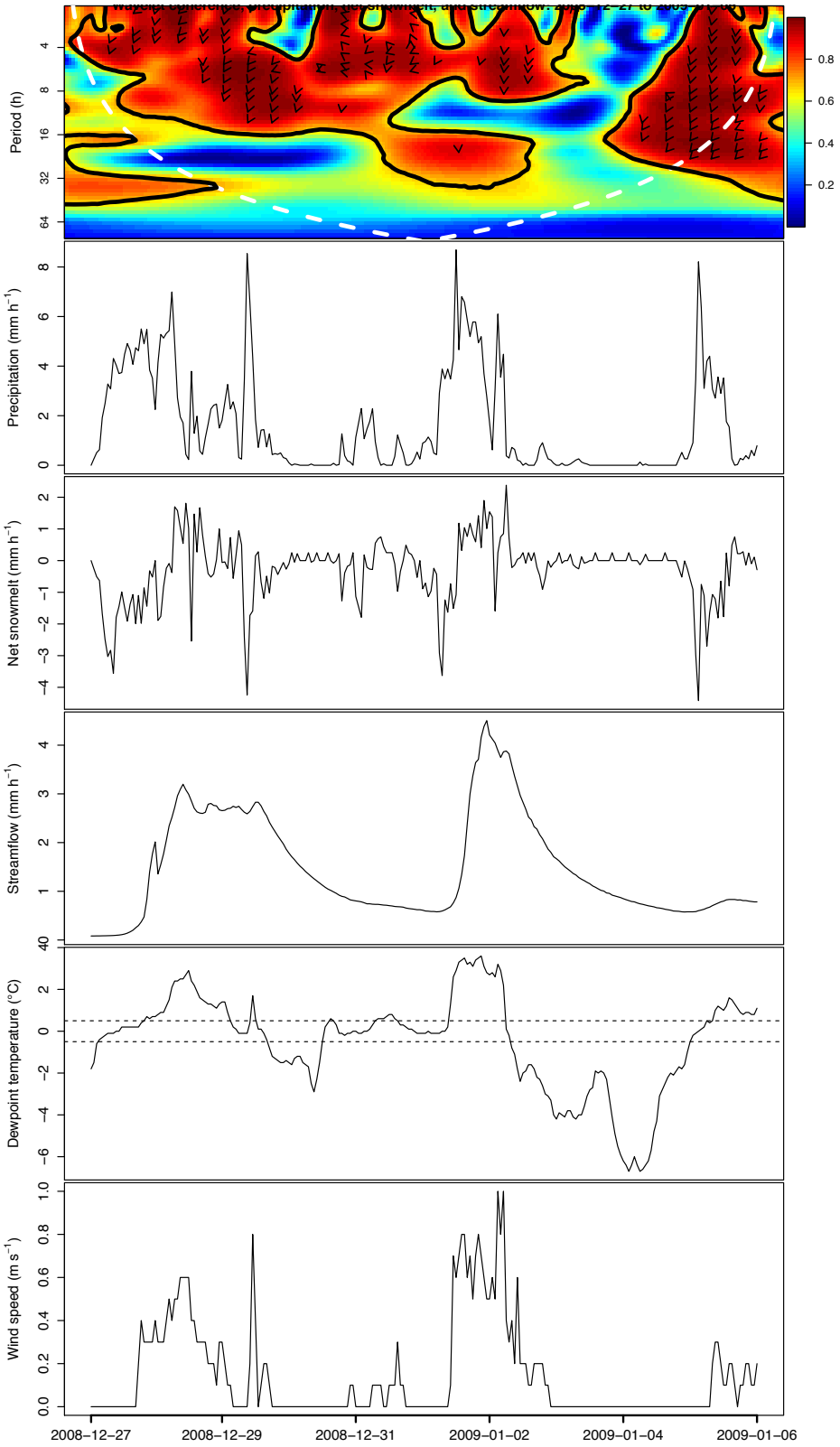

Figure E-23. Wavelet coherence (with power bar on right), precipitation, net snowmelt, Lookout Creek streamflow, dewpoint temperature, and wind speed (from top to bottom) for the 2008-12-27 event.

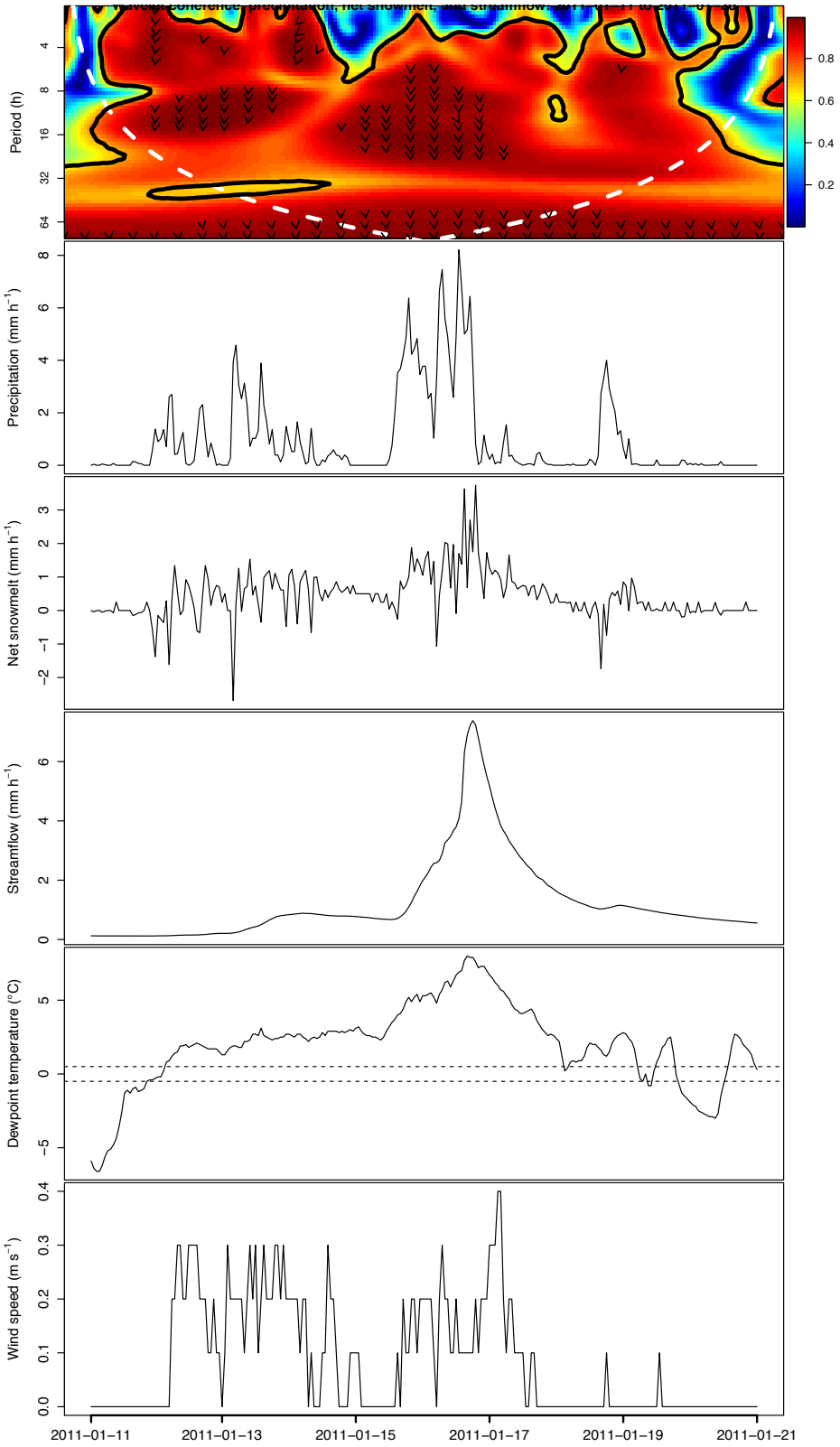

Figure E-24. Wavelet coherence (with power bar on right), precipitation, net snowmelt, Lookout Creek streamflow, dewpoint temperature, and wind speed (from top to bottom) for the 2011-01-11 event.

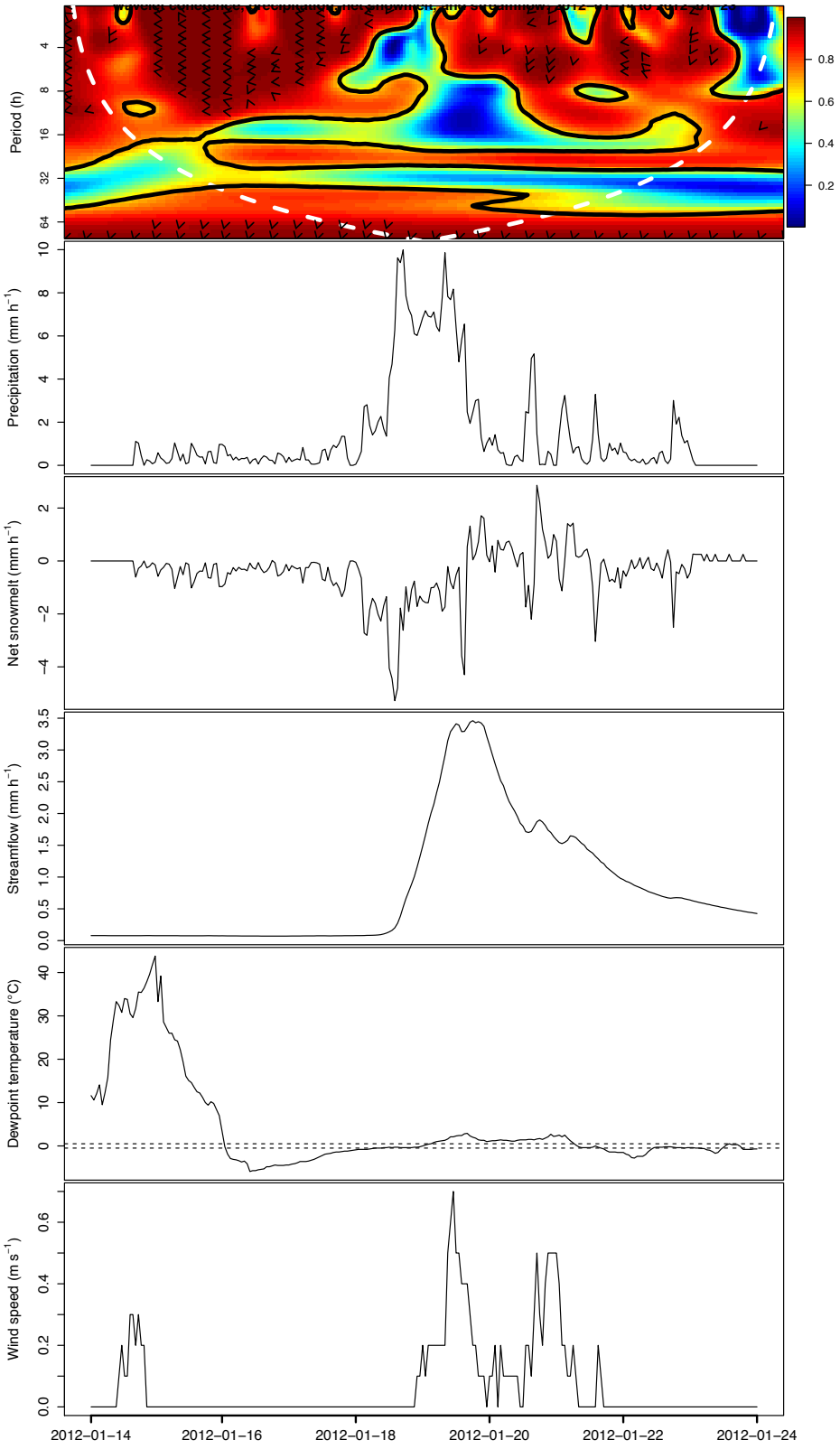

Figure E-25. Wavelet coherence (with power bar on right), precipitation, net snowmelt, Lookout Creek streamflow, dewpoint temperature*, and wind speed (from top to bottom) for the 2012-01-18 event. *Early dewpoint measurements most likely erroneous for this event.

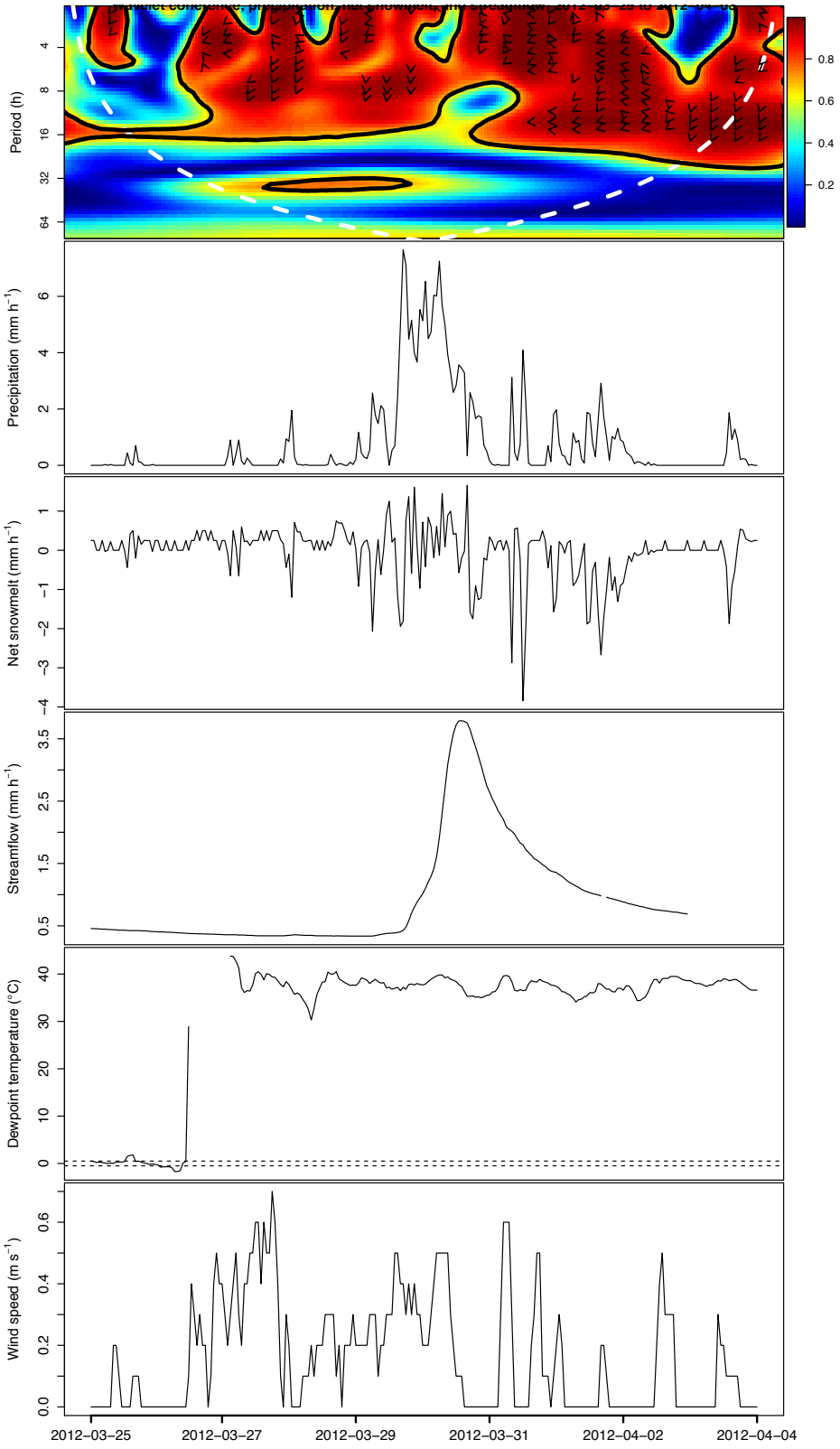

Figure E-26. Wavelet coherence (with power bar on right), precipitation, net snowmelt, Lookout Creek streamflow, dewpoint temperature*, and wind speed (from top to bottom) for the 2012-03-25 event. *Dewpoint measurements most likely erroneous for this event.

Appendix F.

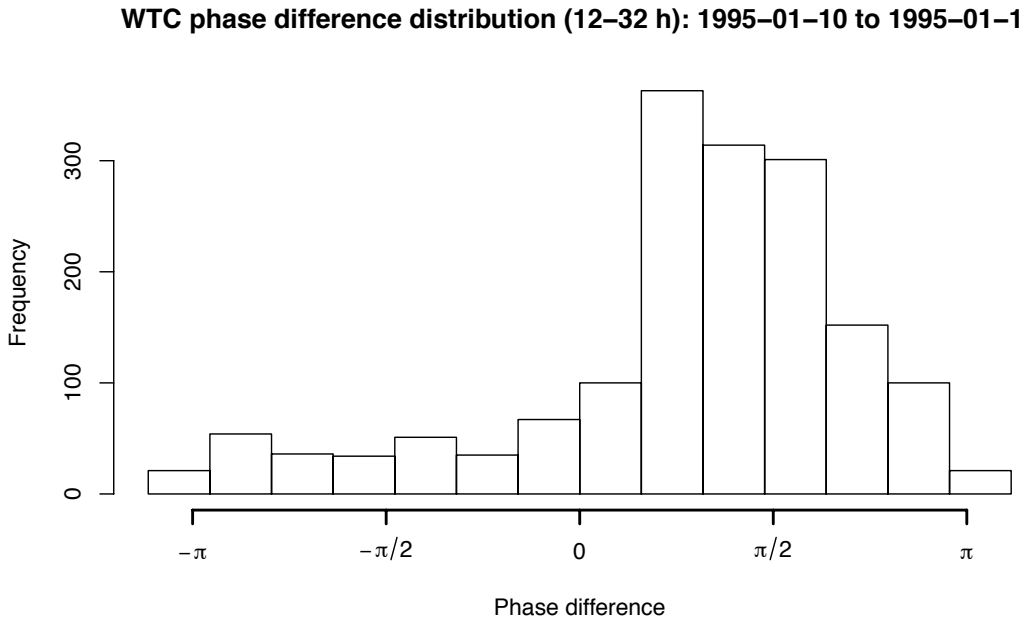

Figure F-1. Phase difference histogram for the 1995-01-08 event. Bins display the number of phase difference observations in a given range between –π and π for each storm's middle four days at time scales between 12 and 32 h. See Figure 3.30 for an explanation of phase differences.

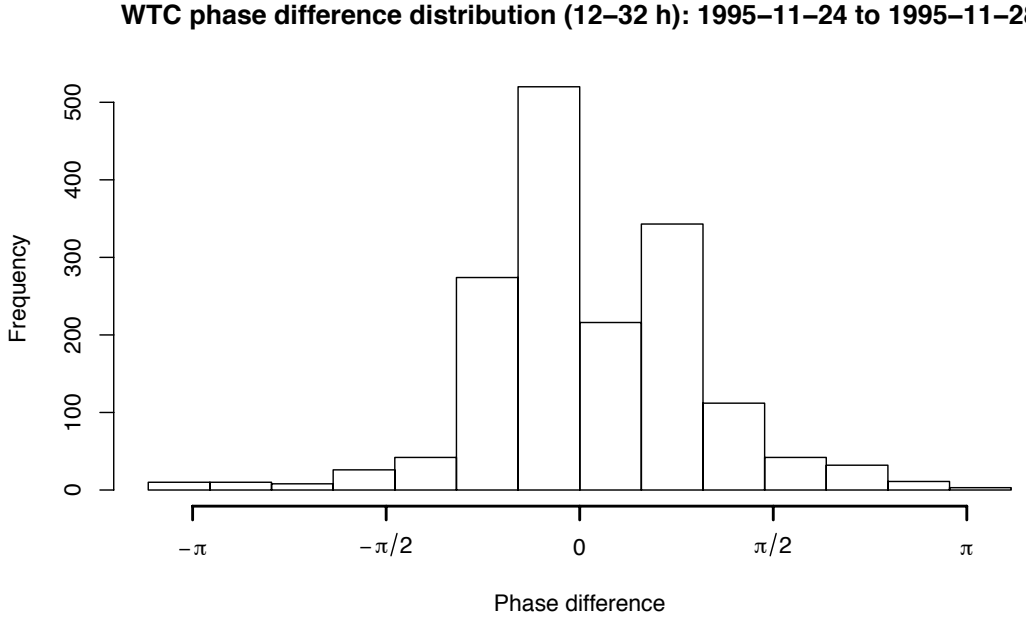

Figure F-2. Phase difference histogram for the 1995-11-22 event. Bins display the number of phase difference observations in a given range between –π and π for each storm's middle four days at time scales between 12 and 32 h. See Figure 3.30 for an explanation of phase differences.

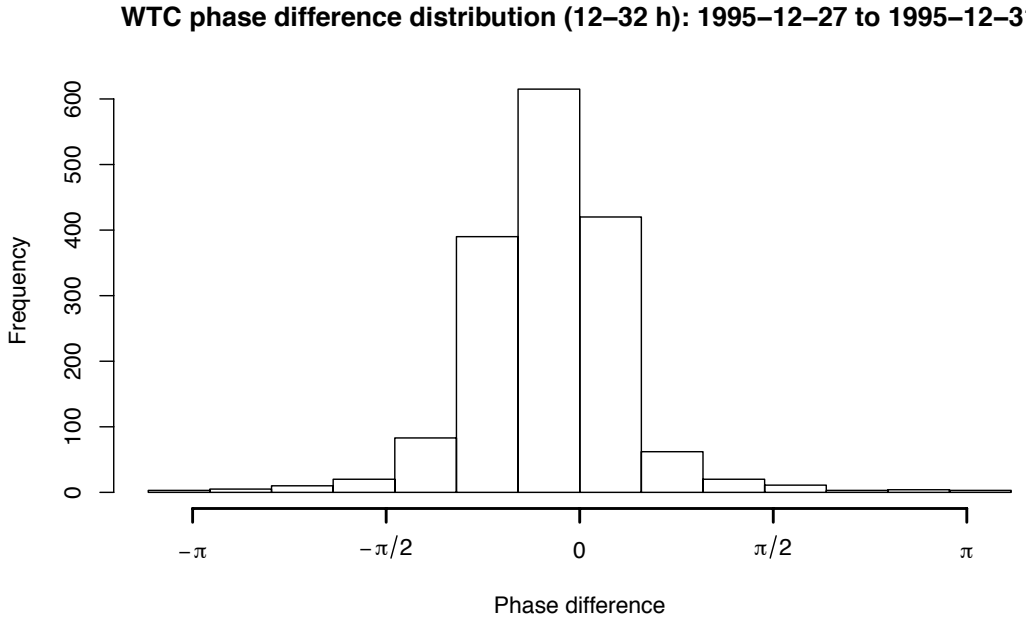

Figure F-3. Phase difference histogram for the 1995-12-25 event. Bins display the number of phase difference observations in a given range between –π and π for each storm's middle four days at time scales between 12 and 32 h. See Figure 3.30 for an explanation of phase differences.

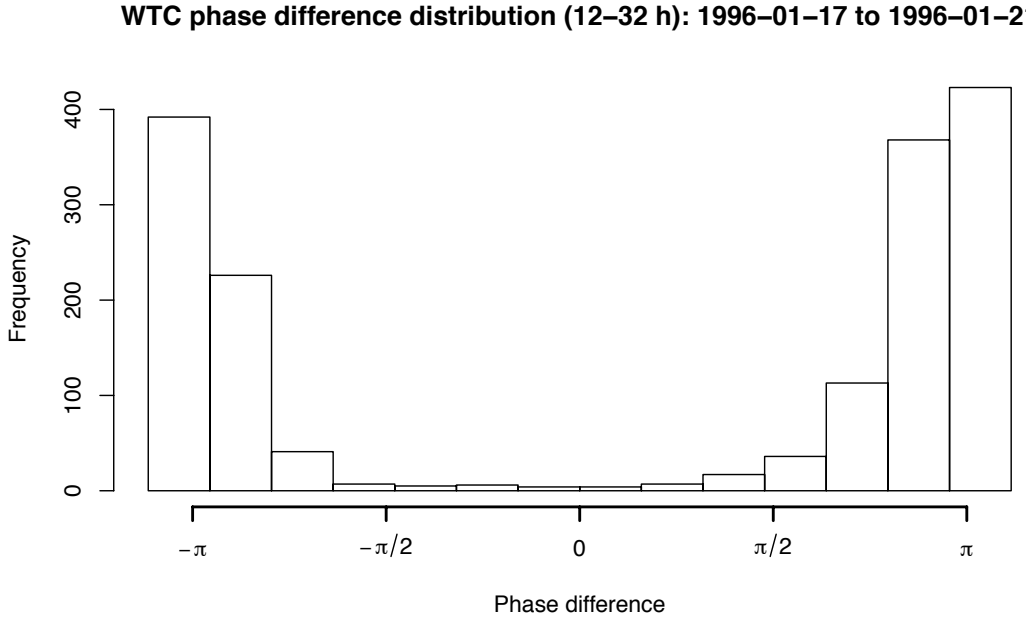

Figure F-4. Phase difference histogram for the 1996-01-15 event. Bins display the number of phase difference observations in a given range between –π and π for each storm's middle four days at time scales between 12 and 32 h. See Figure 3.30 for an explanation of phase differences.

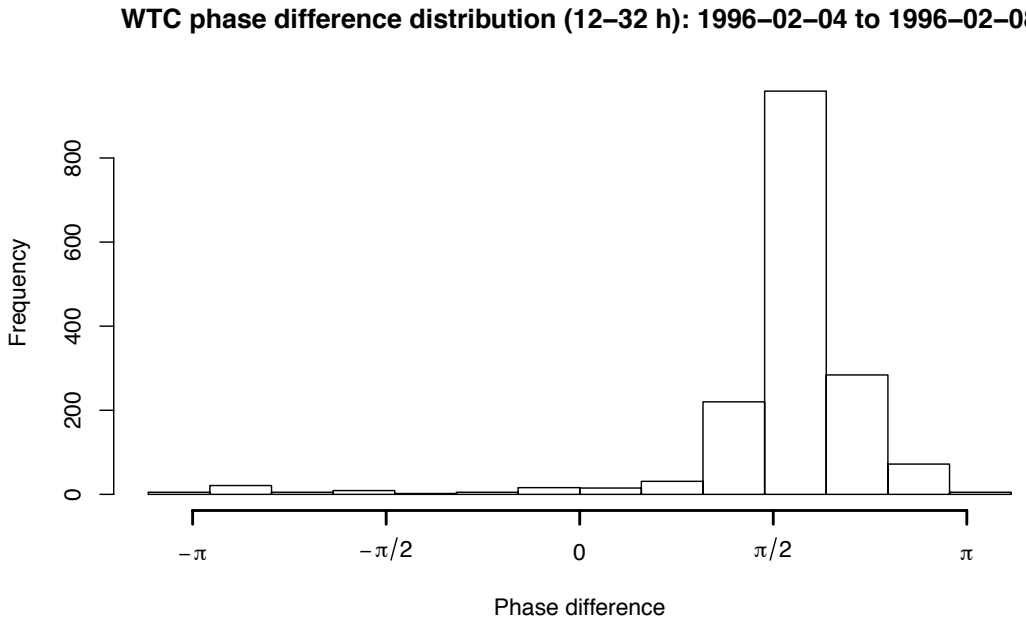

Figure F-5. Phase difference histogram for the 1996-02-02 event. Bins display the number of phase difference observations in a given range between –π and π for each storm's middle four days at time scales between 12 and 32 h. See Figure 3.30 for an explanation of phase differences.

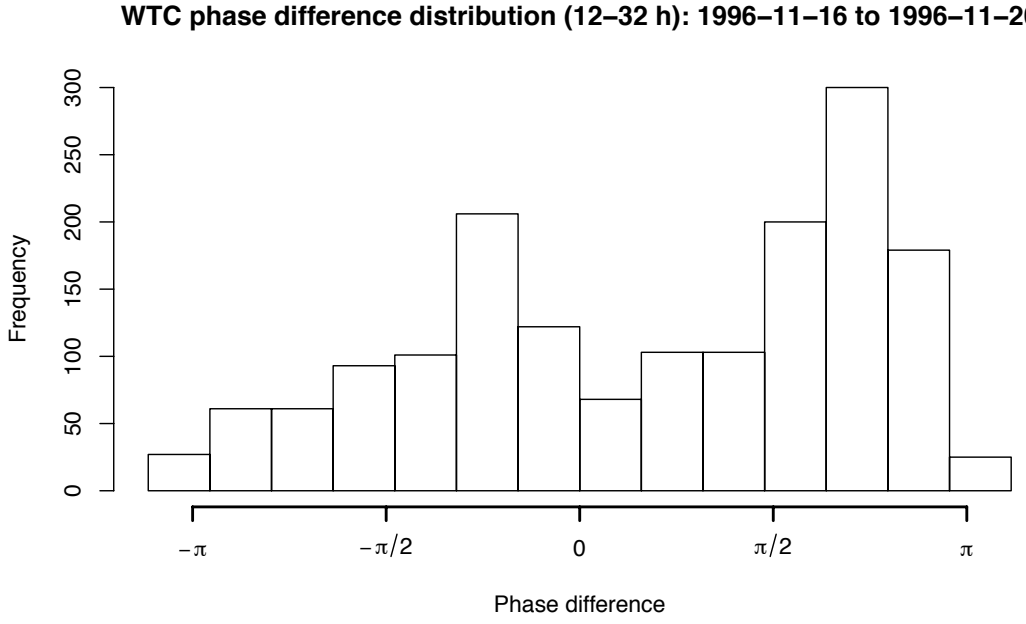

Figure F-6. Phase difference histogram for the 1996-11-14 event. Bins display the number of phase difference observations in a given range between –π and π for each storm's middle four days at time scales between 12 and 32 h. See Figure 3.30 for an explanation of phase differences.

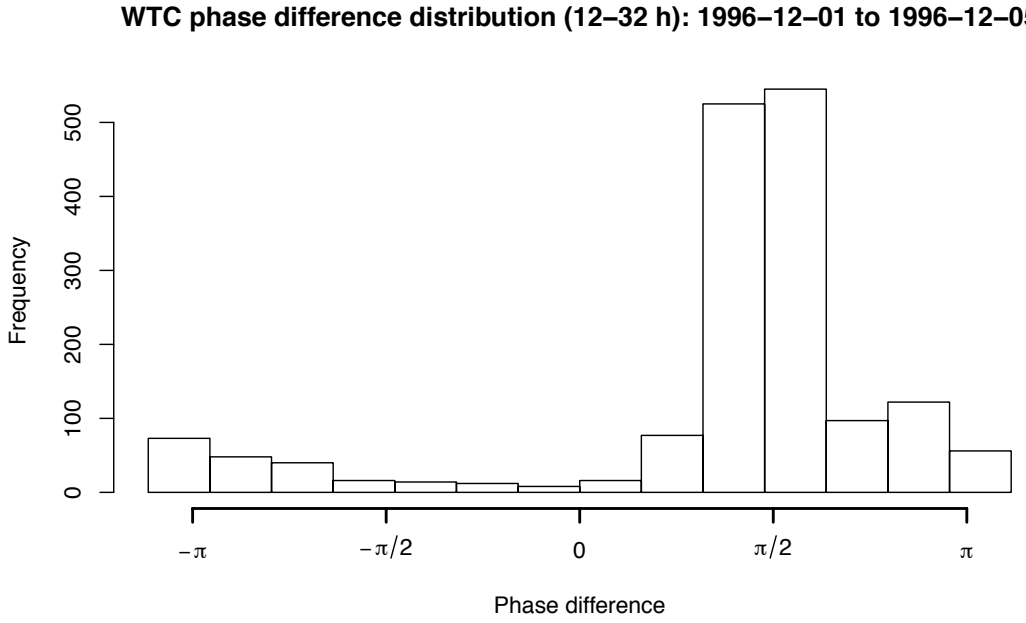

Figure F-7. Phase difference histogram for the 1996-11-29 event. Bins display the number of phase difference observations in a given range between –π and π for each storm's middle four days at time scales between 12 and 32 h. See Figure 3.30 for an explanation of phase differences.

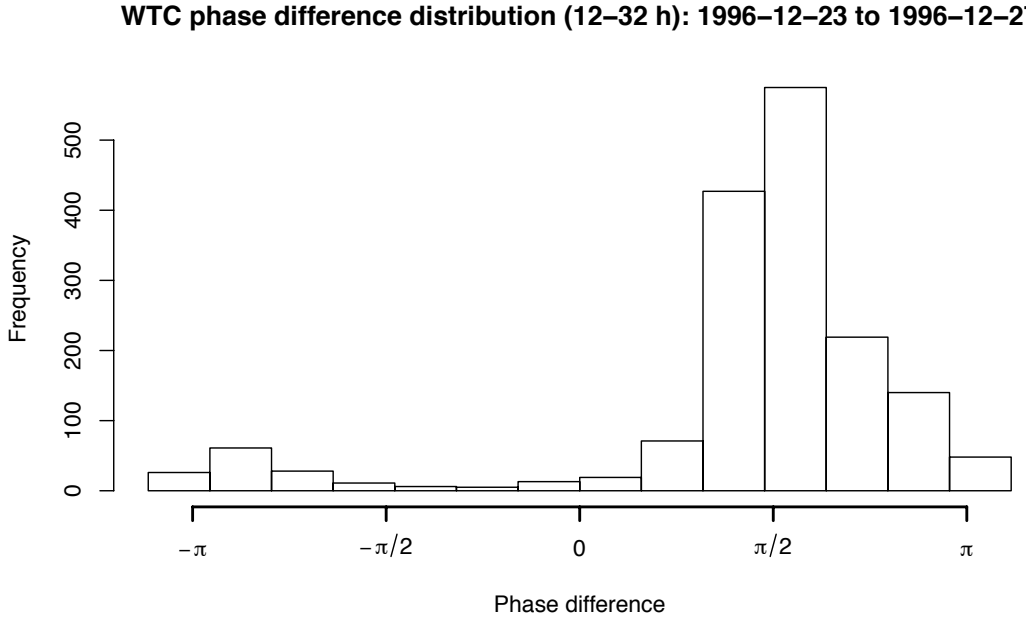

Figure F-8. Phase difference histogram for the 1996-12-21 event. Bins display the number of phase difference observations in a given range between –π and π for each storm's middle four days at time scales between 12 and 32 h. See Figure 3.30 for an explanation of phase differences.

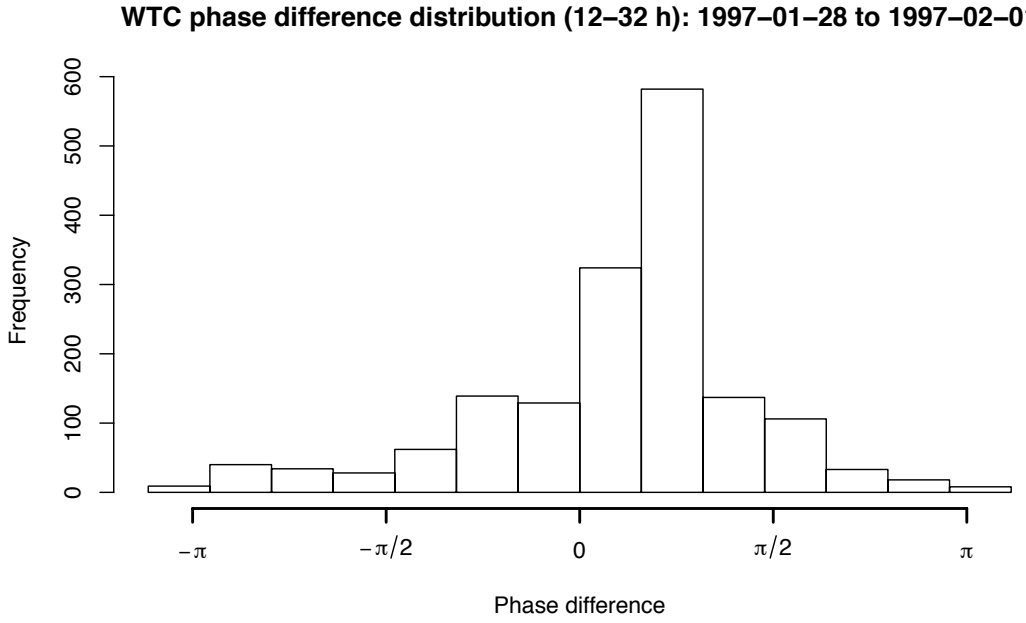

Figure F-9. Phase difference histogram for the 1997-01-26 event. Bins display the number of phase difference observations in a given range between –π and π for each storm's middle four days at time scales between 12 and 32 h. See Figure 3.30 for an explanation of phase differences.

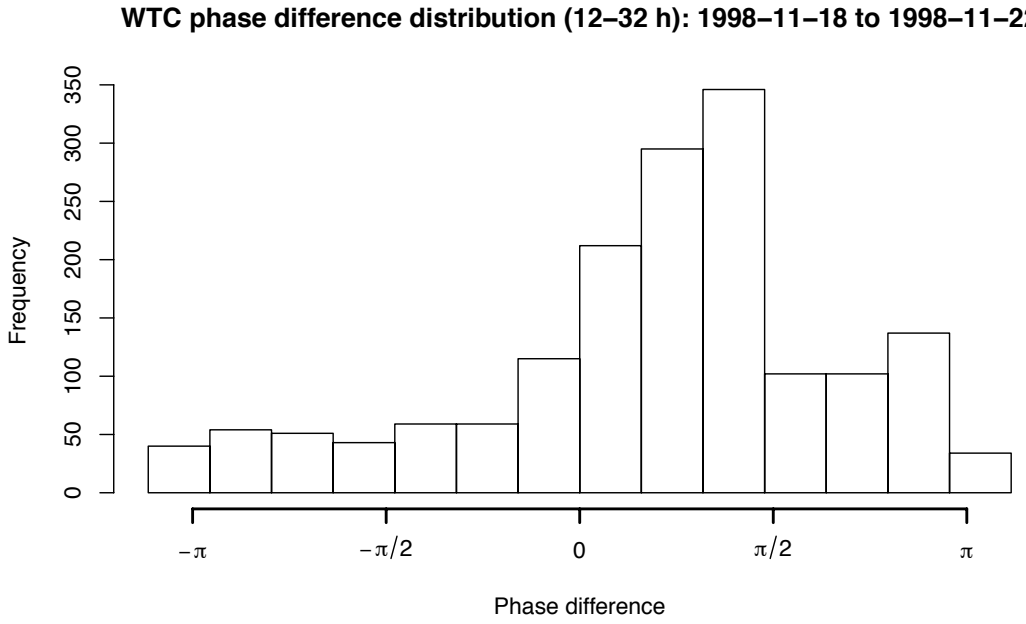

Figure F-10. Phase difference histogram for the 1998-11-16 event. Bins display the number of phase difference observations in a given range between –π and π for each storm's middle four days at time scales between 12 and 32 h. See Figure 3.30 for an explanation of phase differences.

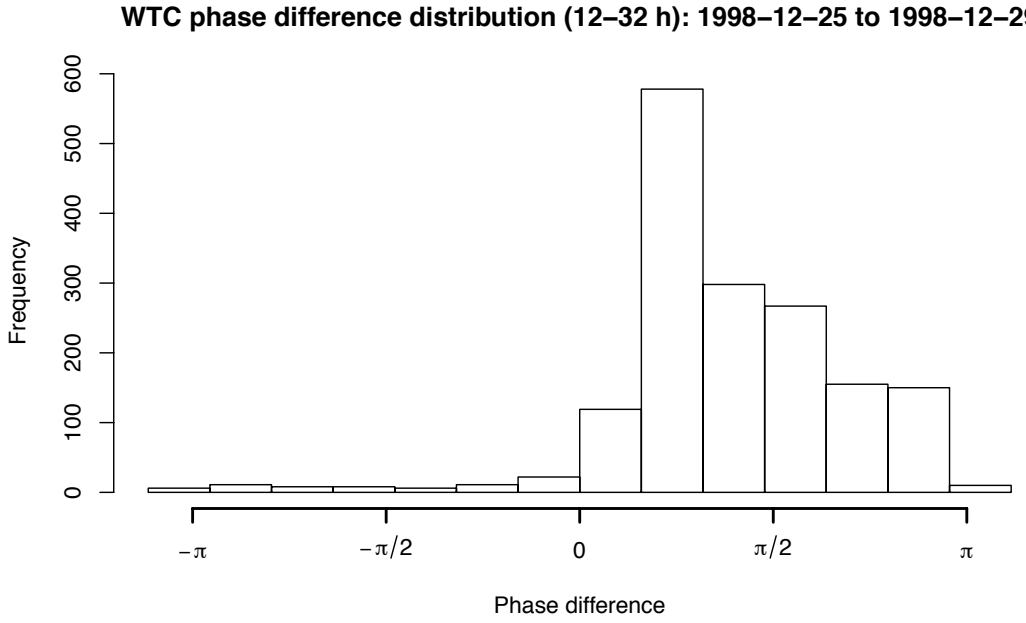

Figure F-11. Phase difference histogram for the 1998-12-23 event. Bins display the number of phase difference observations in a given range between –π and π for each storm's middle four days at time scales between 12 and 32 h. See Figure 3.30 for an explanation of phase differences.

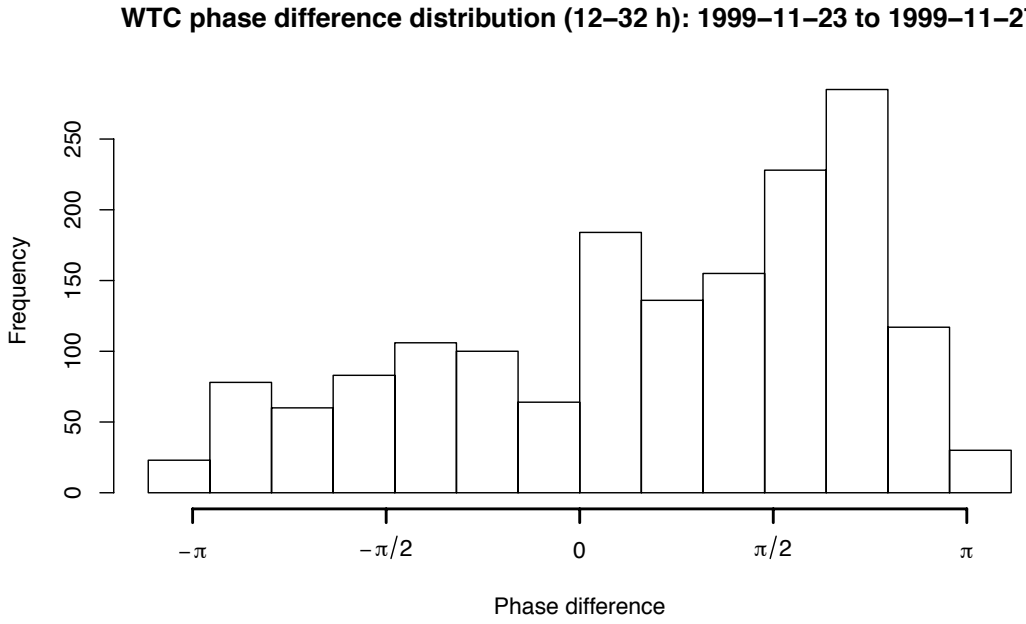

Figure F-12. Phase difference histogram for the 1999-11-21 event. Bins display the number of phase difference observations in a given range between –π and π for each storm's middle four days at time scales between 12 and 32 h. See Figure 3.30 for an explanation of phase differences.

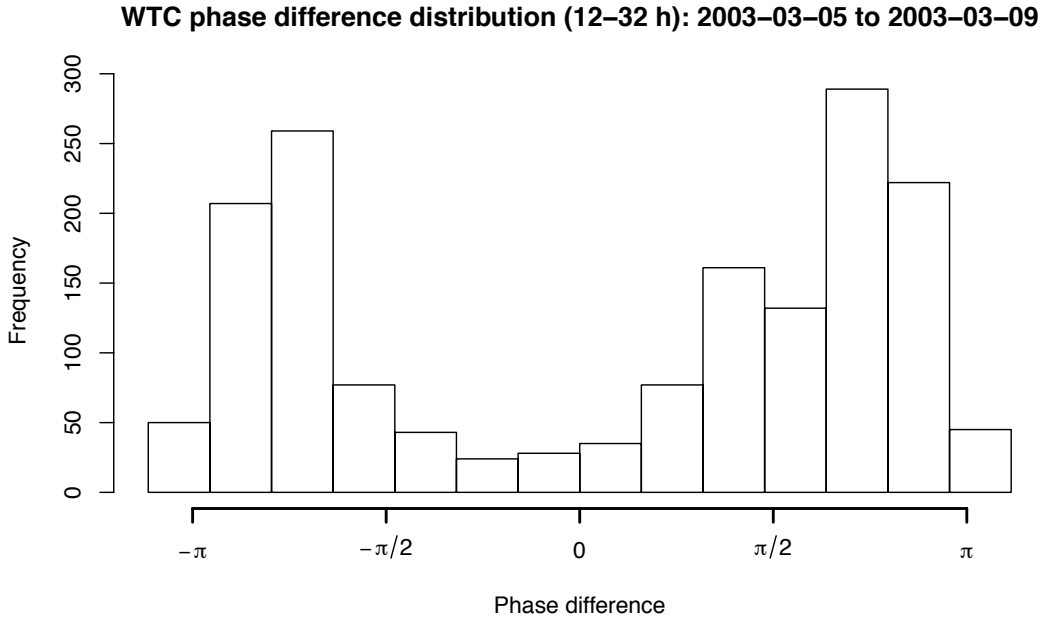

Figure F-13. Phase difference histogram for the 2003-03-03 event. Bins display the number of phase difference observations in a given range between –π and π for each storm's middle four days at time scales between 12 and 32 h. See Figure 3.30 for an explanation of phase differences.

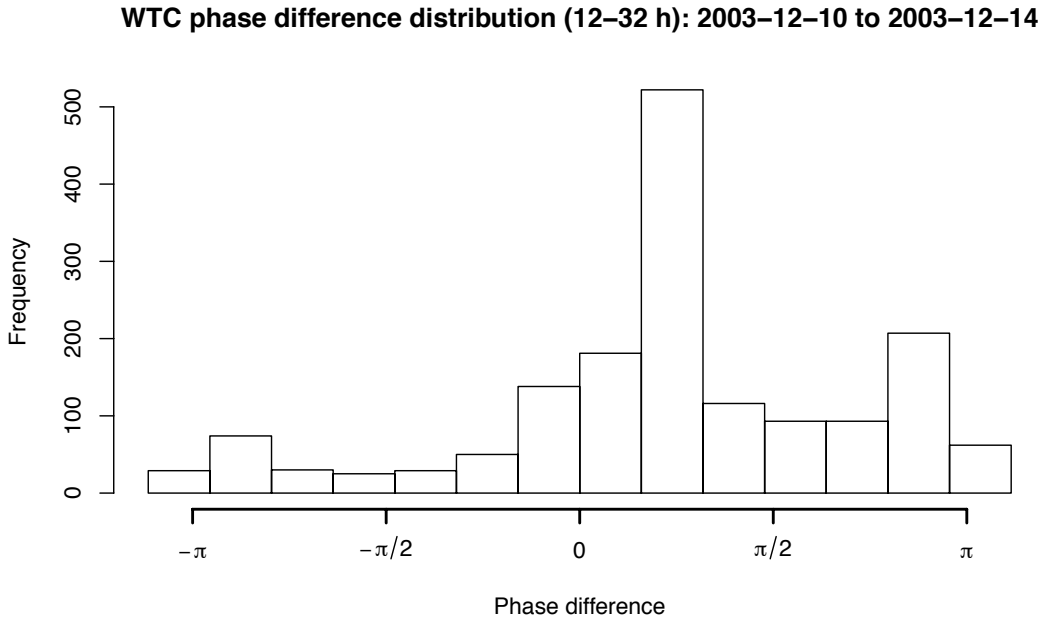

Figure F-14. Phase difference histogram for the 2003-12-08 event. Bins display the number of phase difference observations in a given range between –π and π for each storm's middle four days at time scales between 12 and 32 h. See Figure 3.30 for an explanation of phase differences.

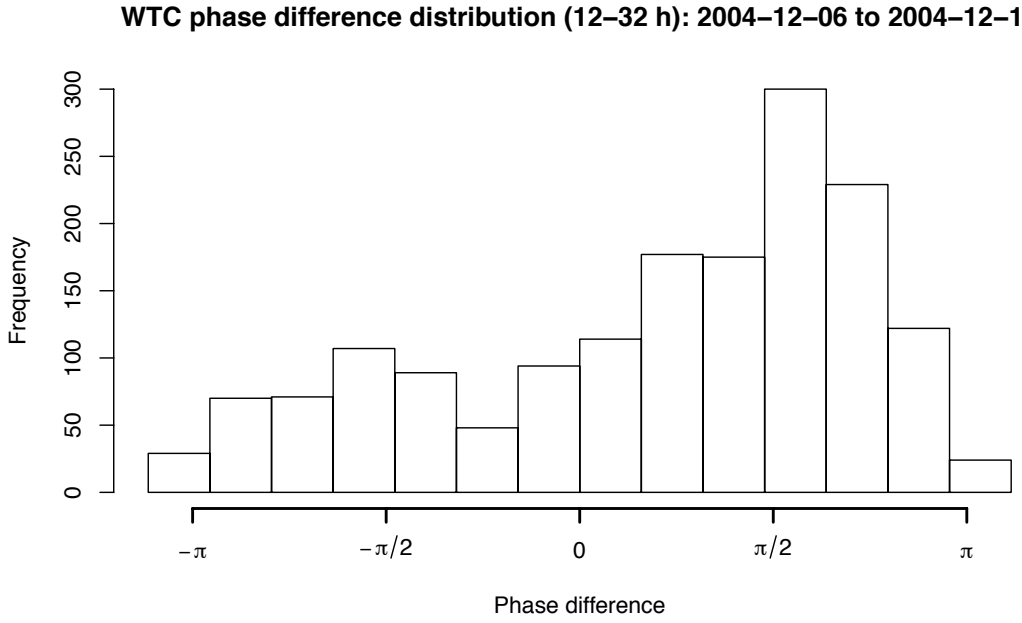

Figure F-15. Phase difference histogram for the 2004-12-04 event. Bins display the number of phase difference observations in a given range between –π and π for each storm's middle four days at time scales between 12 and 32 h. See Figure 3.30 for an explanation of phase differences.

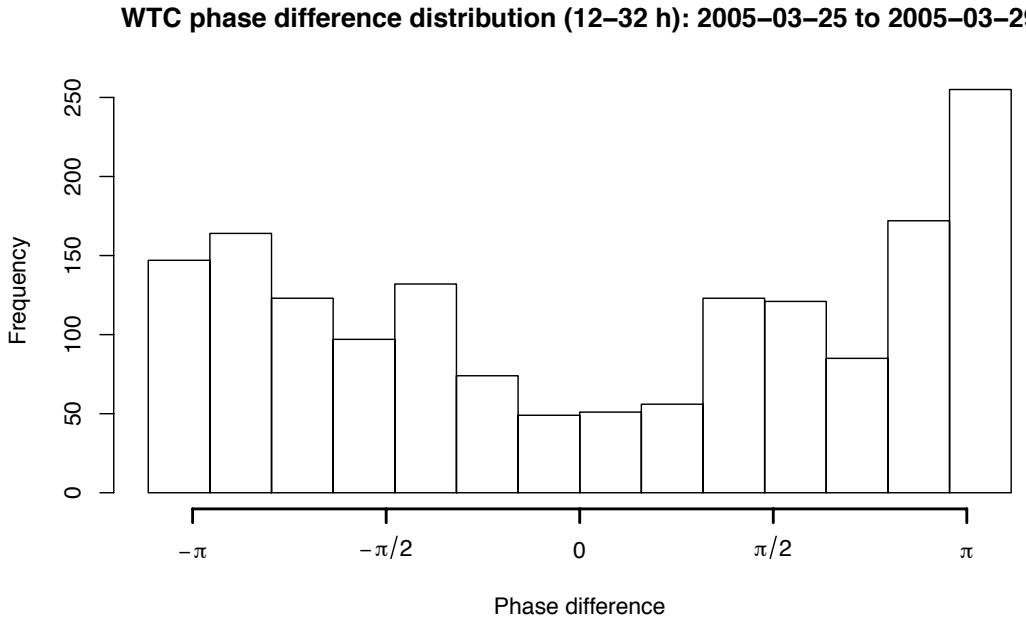

Figure F-16. Phase difference histogram for the 2005-03-23 event. Bins display the number of phase difference observations in a given range between –π and π for each storm's middle four days at time scales between 12 and 32 h. See Figure 3.30 for an explanation of phase differences.

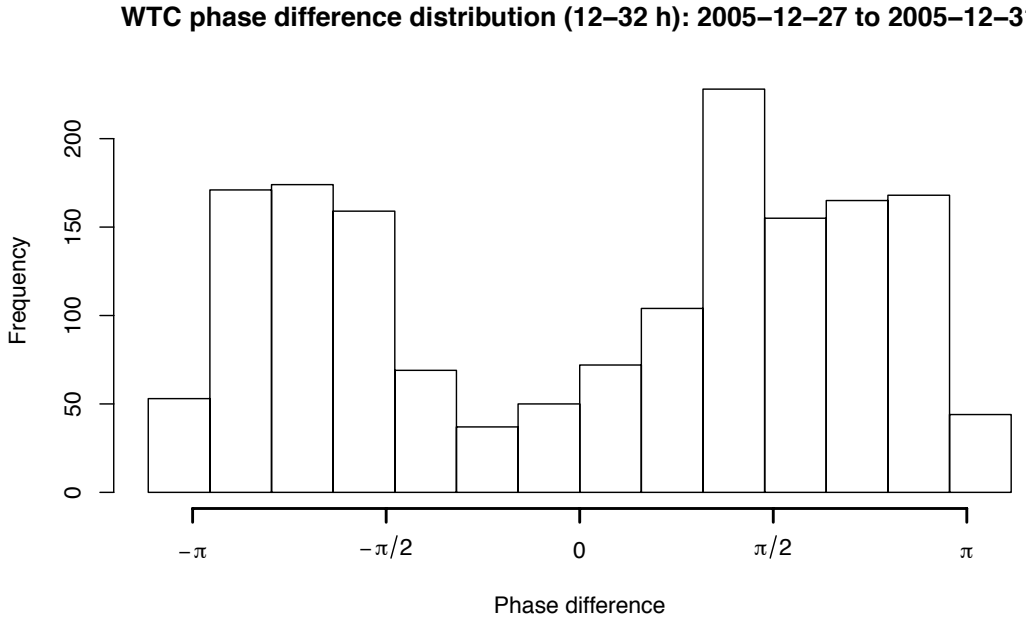

Figure F-17. Phase difference histogram for the 2005-12-25 event. Bins display the number of phase difference observations in a given range between –π and π for each storm's middle four days at time scales between 12 and 32 h. See Figure 3.30 for an explanation of phase differences.

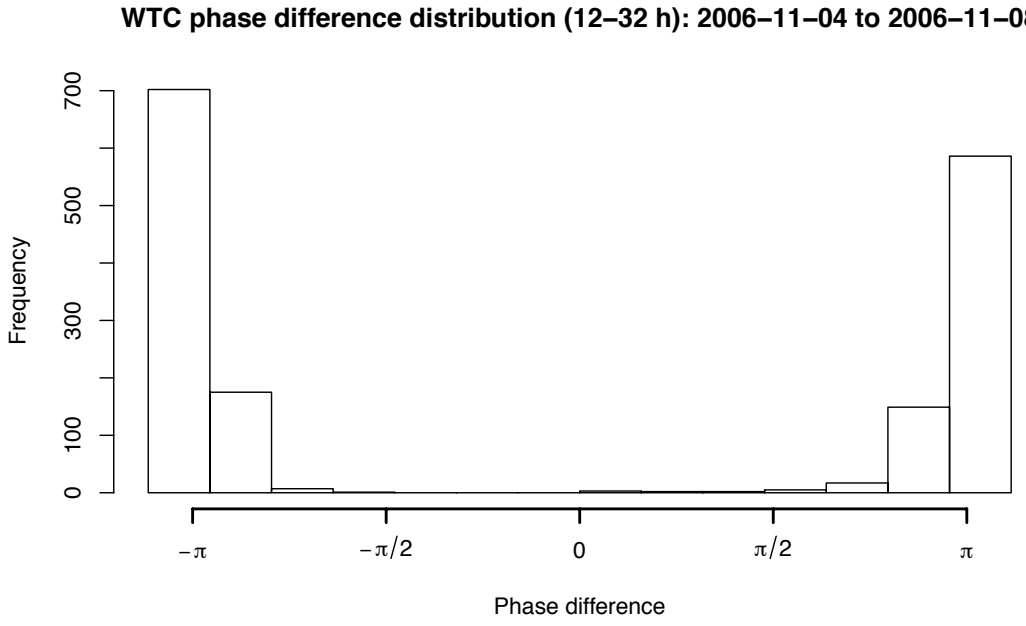

Figure F-18. Phase difference histogram for the 2006-11-02 event. Bins display the number of phase difference observations in a given range between –π and π for each storm's middle four days at time scales between 12 and 32 h. See Figure 3.30 for an explanation of phase differences.

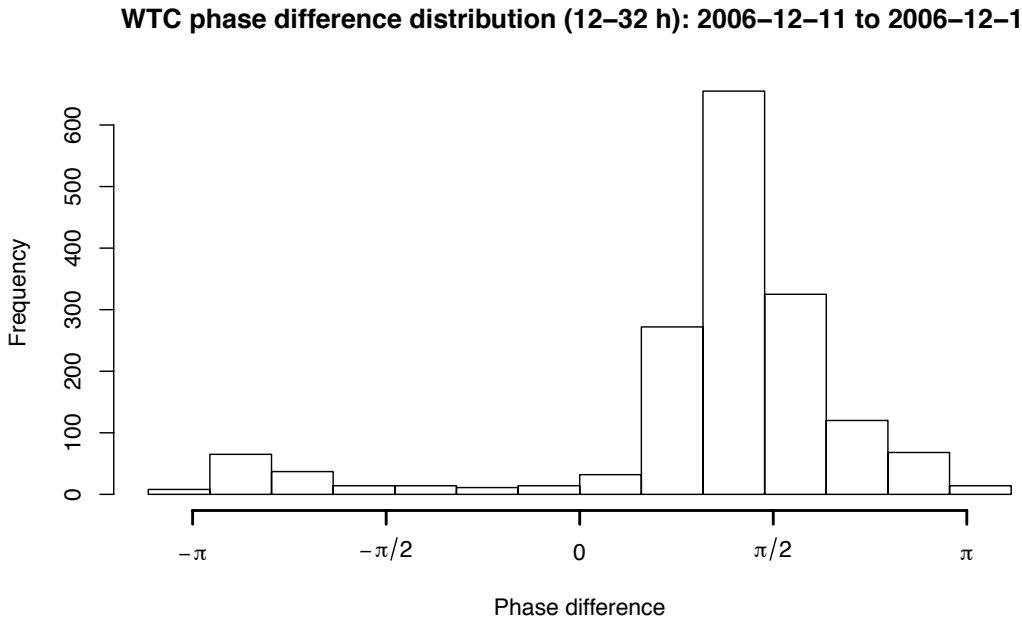

Figure F-19. Phase difference histogram for the 2006-12-09 event. Bins display the number of phase difference observations in a given range between –π and π for each storm's middle four days at time scales between 12 and 32 h. See Figure 3.30 for an explanation of phase differences.

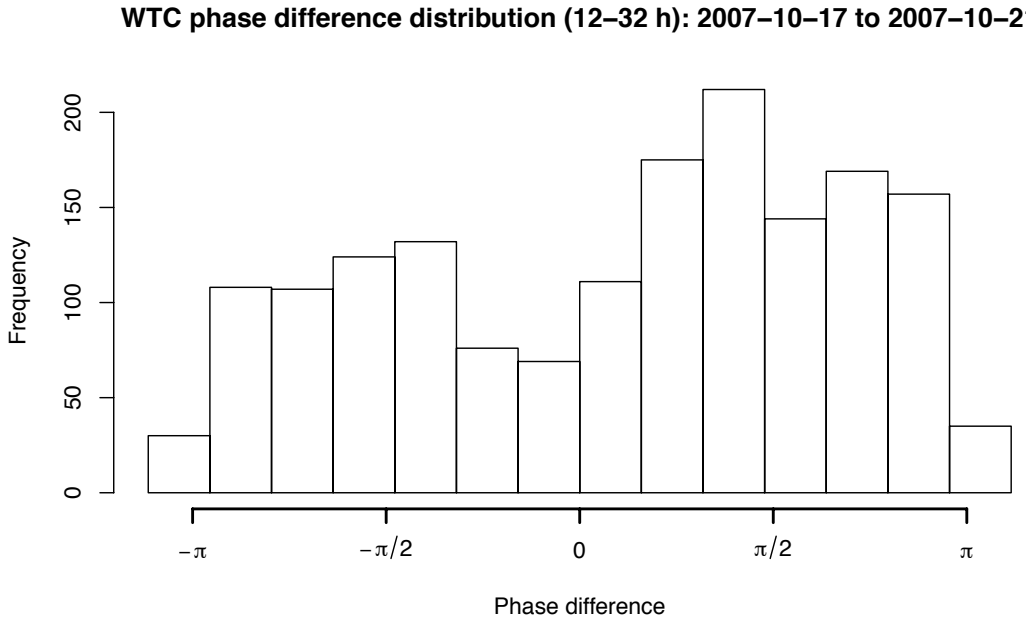

Figure F-20. Phase difference histogram for the 2007-10-15 event. Bins display the number of phase difference observations in a given range between –π and π for each storm's middle four days at time scales between 12 and 32 h. See Figure 3.30 for an explanation of phase differences.

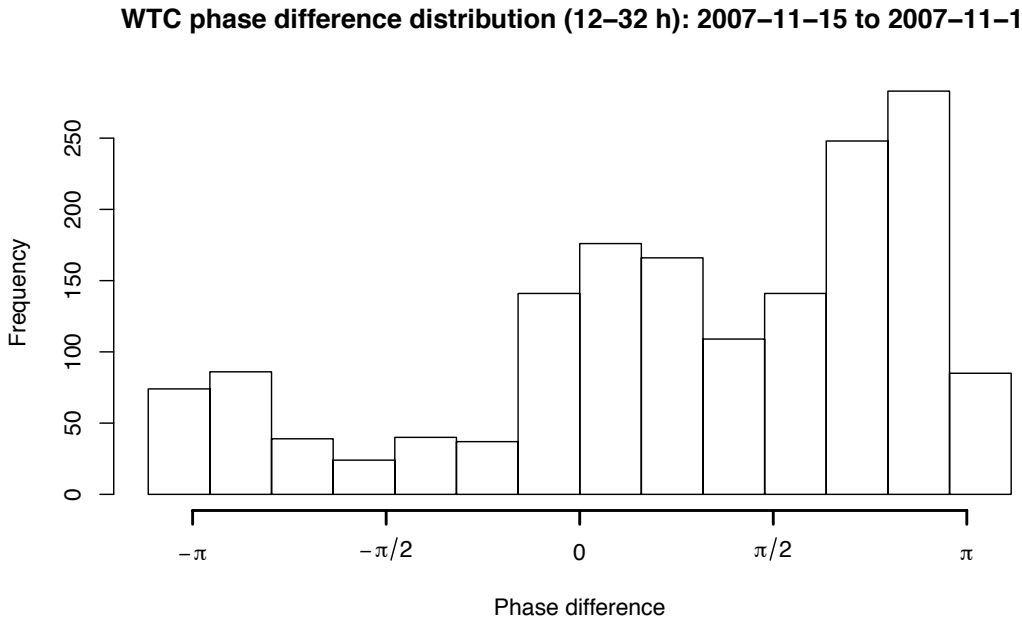

Figure F-21. Phase difference histogram for the 2007-11-13 event. Bins display the number of phase difference observations in a given range between –π and π for each storm's middle four days at time scales between 12 and 32 h. See Figure 3.30 for an explanation of phase differences.

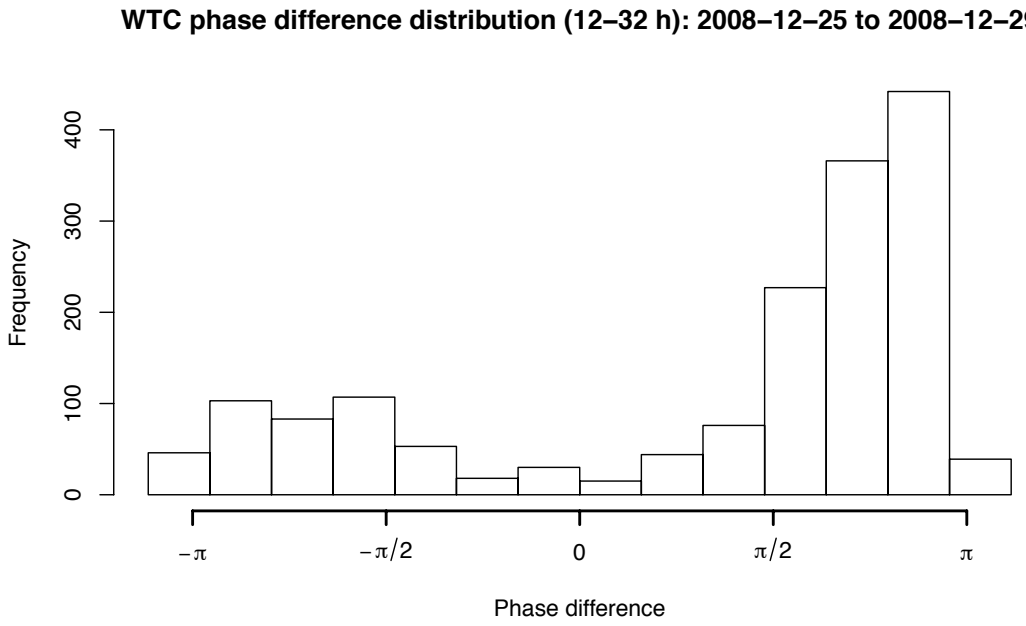

Figure F-22. Phase difference histogram for the 2008-12-23 event. Bins display the number of phase difference observations in a given range between –π and π for each storm's middle four days at time scales between 12 and 32 h. See Figure 3.30 for an explanation of phase differences.

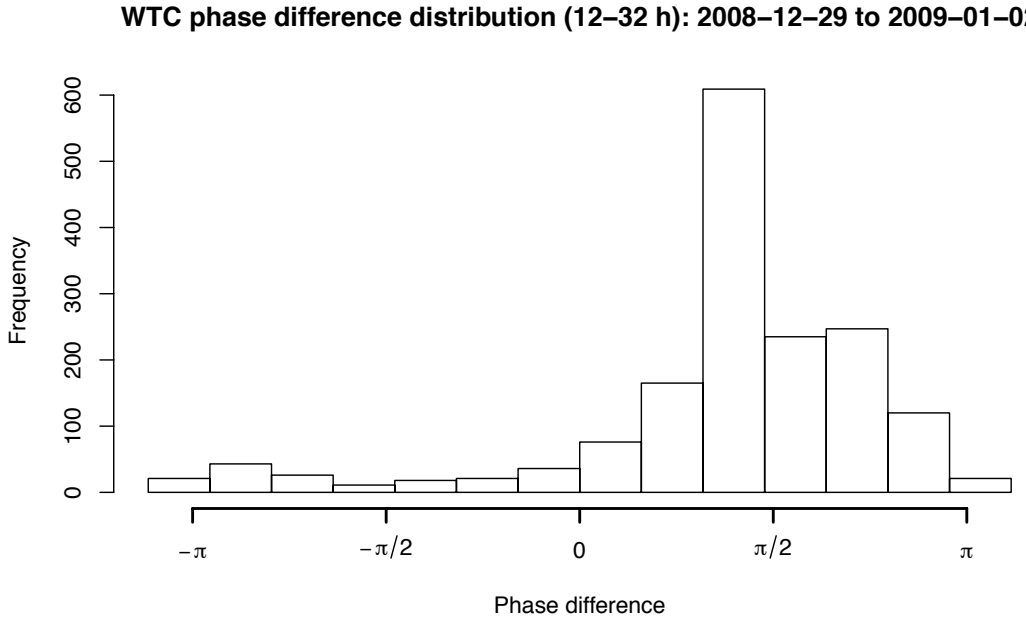

Figure F-23. Phase difference histogram for the 2008-12-27 event. Bins display the number of phase difference observations in a given range between –π and π for each storm's middle four days at time scales between 12 and 32 h. See Figure 3.30 for an explanation of phase differences.

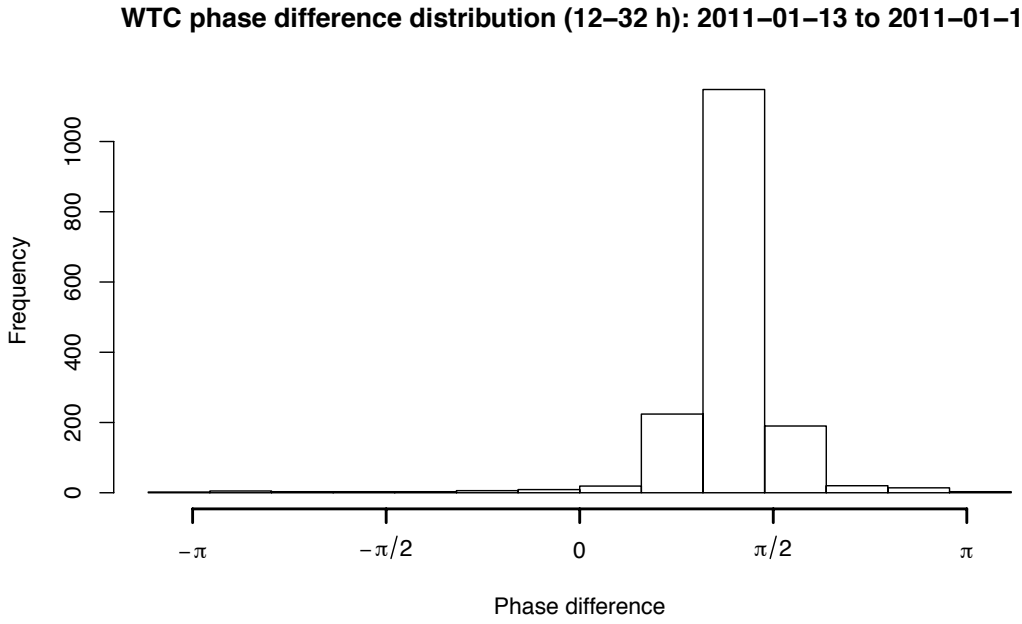

Figure F-24. Phase difference histogram for the 2011-01-11 event. Bins display the number of phase difference observations in a given range between –π and π for each storm's middle four days at time scales between 12 and 32 h. See Figure 3.30 for an explanation of phase differences.

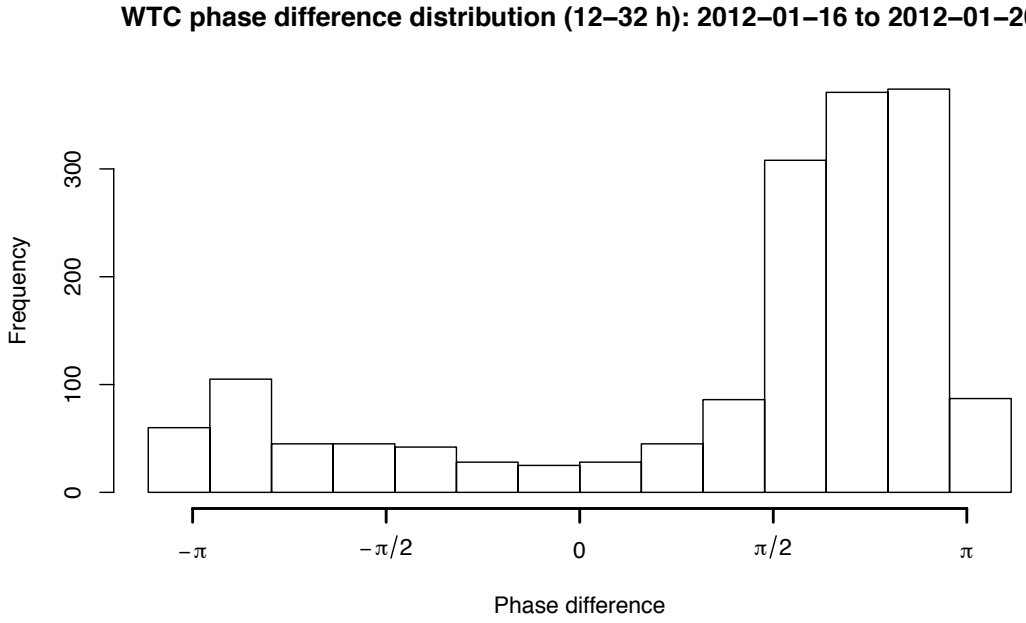

Figure F-25. Phase difference histogram for the 2012-01-14 event. Bins display the number of phase difference observations in a given range between –π and π for each storm's middle four days at time scales between 12 and 32 h. See Figure 3.30 for an explanation of phase differences.

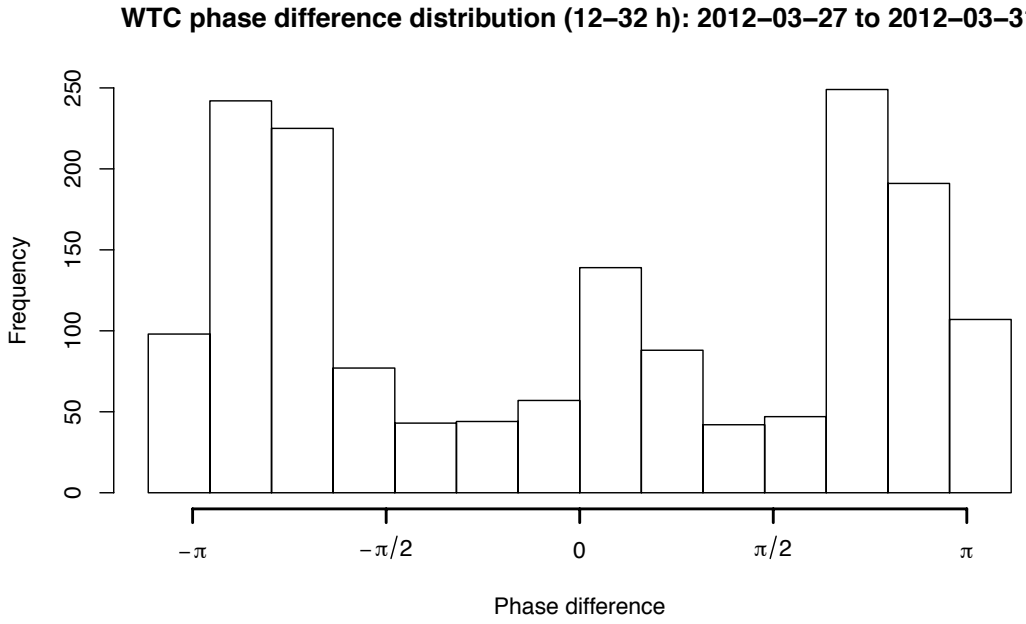

Figure F-26. Phase difference histogram for the 2012-03-25 event. Bins display the number of phase difference observations in a given range between –π and π for each storm's middle four days at time scales between 12 and 32 h. See Figure 3.30 for an explanation of phase differences.